Rheological Measurements in Moderate Reynolds Number Liquid-Solid Flows

Thesis by

Yichuan (Ryan) Song

In Partial Fulfillment of the Requirements for the
Degree of
Doctor of Philosophy

Caltech

CALIFORNIA INSTITUTE OF TECHNOLOGY
Pasadena, California

2022
Defended May 25, 2022

ACKNOWLEDGEMENTS

During my graduate study at Caltech, I received a lot of help and advice.

First, I really thank my Ph.D. advisor, Professor Melany Hunt, for being an incredible mentor during my study at Caltech. I am truly grateful for her support and encouragement during my first half-year after joining the lab. Her office door was always open for me to discuss any confusion and answer my questions. It was through the discussion process with Professor Hunt that many of the ideas presented in this study were inspired. I want to thank her for trusting me to pursue my experimental ideas to eventually overcome challenges.

I want to thank the professors on my thesis committee: Professor Beverly McKeon, Professor John Brady, and Professor John Dabiri. I especially want to thank them again for also being committee members on my Ph.D. candidacy examination. Their suggestions were invaluable for my current work on particulate flows. I also want to mention the Ae 104 classes taught by Professor McKeon. Throughout the classes, I learned various experimental techniques, which are particularly helpful for my experimental work.

I thank Dr. Jim Cory, Dr. Erin Koos, and Dr. Esperanza Linares-Guerrero. Though I never had a chance to meet them in person, it is the apparatus of the Caltech Couette flow device they designed and constructed that makes my present investigation possible. The rheometer used for this study has been redesigned and improved on many aspects, but the fundamental rotational system is still their work. Even though for most parts of my Ph.D. study I was the only student working at the Hunt research lab at the Gates-Thomas sub-basement, I want to thank Han Hsin Lin for discussions regarding the technical issues for multiphase flows.

I want to thank the many MCE staff members who helped me during my Ph.D. study. I appreciate the help from our research group assistants, formerly Holly Golcher and now Mikaela Laite, as well as the MCE department administrator, Lynn Seymour, who helped me with the logistics for the laboratory. I am indebted to John Van Deusen, who helped me make the Caltech Couette flow device functional again. I thank Petros Arakelian who kindly allows me to use the engine crane.

I would like to thank all the GALCIT people who directly or indirectly helped me at Caltech. I also want to thank my friend Cong Wang, who was always willing to

help me whenever I faced any challenges. I thank the GALCIT options manager, Christine Ramirez who was always there to answer my questions.

Finally, I thank my father, Hongjie Song and my mother, Dandan Sun. They are always my source of emotional support. One of my parents' greatest regret is that they were not able to attend college due to their family backgrounds forty years ago. It is through their encouragement that I became first college student in my family. They are the ultimate reason why I chose to take the challenge of Ph.D. study after college. I wouldn't be here to present my thesis without their continuous support.

ABSTRACT

Liquid-solid flows with inertial and viscous effects are critical for many engineering and geophysical applications, such as the processing of biomass slurry and the control of debris flows. However, modeling the rheological behaviors of these complex flows remains a challenge. Prior investigations on the liquid-solid flows typically cover suspensions in which the particle Reynolds numbers (Re) based on the particle diameter and shear rate are less than 1. Limited prior study at Caltech focuses on particle Reynolds numbers above 10. This thesis focuses on rheological experiments for the moderate Reynolds number regime where both inertial and viscous effects are important, with particle Reynolds numbers from 0.5 to 800. The rheological experiments include torque measurements of *mm* scale-sized polystyrene and SAN particles with a range of solid fractions from 10% to 50%, considering both neutrally-buoyant and settling suspensions with density ratios of 1 and 1.05. This thesis discusses rheological measurements of three different fields: pure fluids, neutrally-buoyant suspensions, and non-neutrally-buoyant suspensions.

The pure fluids measurements determine the flow starts to transition to turbulent flow for gap Reynolds numbers above 6.5×10^3 in the Caltech Couette flow device. For suspensions with matched particle and fluid densities and solid fractions less than 40%, we find that the effective viscosity only depends on the particle solid fraction until we observe the shear-thickening behaviors for Re of approximately 10. For the intermediate Re from 10 to 100 and lower solid fractions, the effective viscosity not only depends on the particle solid fraction, but also shows increased dependence on Re. For Re greater than 100, the liquid-solid flows transition to the turbulent regime, similar to what we see for the pure fluids. At the maximum solid fraction of 50%, the magnitude of the effective viscosity has increased by a factor of 20 as compared to the results of the 10% solid fraction, but the effective viscosity is nearly independent of Re. A particle Reynolds number (Re') based on the maximum shear flow velocity and the particle diameter is introduced to examine the effective viscosity of the suspensions. Since the present studies use particles with different sizes, Re' is found to be a better way to correlate the effective viscosity than the traditional Re. For the analysis of liquid-solid flows with a density ratio of 1.05, the effective viscosity of the particulate flow increases with the Stokes number for loading fractions of 10% and 20%, while the dependence is reversed for higher solid fractions.

TABLE OF CONTENTS

LIST OF ILLUSTRATIONS

LIST OF TABLES

NOMENCLATURE

$\dot{\gamma}$.	Shear rate.
μ.	Fluid viscosity.
μ'.	Suspension viscosity.
ω.	Rotational speed.
$\overline{\phi}$.	Loading fraction.
ϕ.	Solid fraction.
ϕ_m.	Maximum solid fraction.
ψ.	Sphericity.
ρ_f.	Suspending liquid density.
ρ.	Fluid density.
ρ_p.	Particle density.
τ.	Shear stress.
Ar.	Archimedes number, $Ar = gd^3\rho_f(\rho_p - \rho_f)/\mu^2$.
b.	Annulus gap.
D.	Pipe diameter.
d.	Particle diameter.
e.	Coefficient of restitution.
g.	Gravitational acceleration.
H.	Height of test cylinder.
h.	Particle height in the annulus.
h_o.	Particle bed height at $\dot{\gamma} = 0$.
h_{middle}.	Height of the middle testing cylinder.
h_{top}.	Height of the top inner cylinder.
h_T.	Height of annulus.
k.	Boltzmann constant.

M_o**.** Torque at the 0 shear rate.

$M_{laminar}$**.** Torque considering laminar theory, $M_{laminar} = 4\pi\mu H\omega r_i^2 r_o^2/(r_o^2 - r_i^2)$.

r_i**.** Inner radius of the annulus.

r_o**.** Outer radius of the annulus.

Re**.** Particle Reynolds number, $Re = \rho\dot{\gamma}d^2/\mu$.

Re'**.** Defined particle Reynolds number, $Re' = \rho_f dU_{wall}/\mu$.

Re_b**.** Gap Reynolds number, $Re_b = \rho\omega r_o b/\mu$.

St**.** Stokes number, $St = \rho_p Re/9\rho_f$.

St'**.** Defined Stokes number, $St' = \rho_p dU_{wall}/9\mu$.

T**.** Absolute temperature.

μ'/μ**.** Effective viscosity.

$M_{lam}{}'$**.** $M'_{lam} = 2\pi\mu'\dot{\gamma}H{r_i}^2$.

$Re_b{}'$**.** Gap Reynolds number obtained using μ', $Re_b{}' = \rho\omega r_o b/\mu'$.

Chapter 1

INTRODUCTION

Liquid-solid flows with both inertial and viscous effects are prevalent in industrial and geophysical environments. The conversion of biomass into fuels needs to mix biomass materials with water to form a liquid-solid suspension, including both settling particles and neutrally-buoyant particles, with a wide particle size range from μm to mm. Understanding the rheological behaviors of the biomass mixture can help improve the conversion efficiency in biomass reactor (Stickel and Powell, 2005). Another example is the debris flow that is usually caused by intense precipitation on steep mountains. The liquid-solid mixture has soil and water as the fluid phases, and rocks as the settling solid phases (Brennen, 2005). The dangerous liquid-solid flows often move fast and are challenging to predict. Understanding the properties of the debris flows is important to design effective control strategies for these dangerous mixtures. Therefore, it provides ample motivations to develop rheological models which describe the moderate-Reynolds-number liquid-solid flows.

The objective of this experimental project is to provide the scientific community with accurate measurements for both neutrally-buoyant and non-neutrally-buoyant suspensions over the previously untested Reynolds number regions, which will advance the developments of rheological models of the particulate flows considering moderate particle Reynolds numbers. In this thesis, liquid-solid flows are described in detail, demonstrating the interactions between the particles and fluids, along with the inertial effects from both solid and liquid phases, and the role of particle collisions and particle velocity fluctuations on the laminar-turbulent transition and on the stresses in the moderate-Reynolds-number liquid-solid mixture. Following the explanation, this chapter also presents the reviews covering theories and experiments of the previous particulate-flow studies.

1.1 Rheology of neutrally buoyant suspensions

Liquid-solid flows with neutrally-buoyant particles encompass many studies considering particle Reynolds number. In the neutrally buoyant environment, the particles are uniformly distributed throughout the liquid body, and the flow is considered as homogenous.

This section reviews some fundamental properties of liquid-solid two-phase flow. An overview of some previously reported experiments is also presented.

The relative viscosity of a suspension can be analyzed using dimensionless terms, which can be simplified to 6 variables at steady state (Stickel and Powell, 2005):

$$\frac{\mu'}{\mu} = f\left(\phi, \frac{b}{d}, Re, St, Ar, Pe\right), \tag{1.1}$$

where ϕ is the solid fraction and b is the annulus gap. Re is the particle Reynolds number defined as:

$$Re = \frac{\rho \dot{\gamma} d^2}{\mu}, \tag{1.2}$$

where ρ is the fluid density, $\dot{\gamma}$ is the shear rate, d is the particle diameter, and μ is the fluid viscosity. St is the Stokes number defined as:

$$St = \frac{1}{9}\frac{\rho_p}{\rho_f} Re, \tag{1.3}$$

where ρ_p is the particle density. Ar is the Archimedes number, which can be viewed as the Reynolds number based on the Stokes settling velocity. Ar is defined as:

$$Ar = \frac{g d^3 \rho_f (\rho_p - \rho_f)}{\mu^2}, \tag{1.4}$$

where g is the gravitational acceleration. Pe is the Péclet number, which is the ratio of advective transport rate to diffusive transport rate. It is defined as:

$$Pe = \frac{6\pi\mu d^3 \dot{\gamma}}{kT}, \tag{1.5}$$

where T is the temperature and k is the Boltzmann constant. The diffusive transport described in the Péclet number is a molecular diffusion process, which is distinct from the diffusion caused by mixing.

1.2 Rheology of low-Reynolds-number suspensions

There are many studies for low-Reynolds-number liquid-solid flows (Stickel and Powell, 2005). However, most of these studies cover particulate flows in which Reynolds numbers are small (Re from 10^{-6} to 10^{-2}). Typically, these investigations used particles with a diameter size of μm; therefore, the Reynolds number is much less than 1, and the inertial effect is negligible (Batchelor, 1970; Brady and Bossis, 1988; Stickel and Powell, 2005). For low-volume-fraction mixtures, the suspensions follow Newtonian behaviors. Hence, the shear stress τ depends linearly on the suspension viscosity μ' and the shear rate $\dot{\gamma}$, and is often modelled as,

$$\tau = \mu' \dot{\gamma}. \tag{1.6}$$

For dilute suspensions, the effective viscosity of the particulate flow only depends on ϕ. In a concentrated regime for ϕ greater than 40%, the effective viscosity may also have a dependence on $\dot{\gamma}$ (Stickel and Powell, 2005).

Effective viscosity theories

At present, different semi-empirical formulas allow us to calculate the effective viscosity for particulate flows considering low-Reynolds numbers. Among these theories, the Eilers and Krieger-Dougherty relations are two examples to be considered (Eilers, 1941; Krieger, 1963).

The study by Eilers (1941) proposed the well-known Eilers relationship that estimates the relative viscosity of the particulate flows of particles with spherical shape based on ϕ,

$$\frac{\mu'}{\mu}(\phi) = \left(1 + \frac{a\phi}{1 - \frac{\phi}{\phi_m}}\right)^2, \tag{1.7}$$

where a is the constant, and ϕ_m is the maximum solid fraction. Krieger (1963) studied suspensions with uniformly distributed particles, and correlated the relative viscosity with ϕ_m as,

$$\frac{\mu'}{\mu}(\phi) = \left(1 - \frac{\phi}{\phi_m}\right)^{-a\phi_m}, \tag{1.8}$$

where a and ϕ_m are used as fitting parameters. The Krieger-Dougherty correlation has been widely used to correlate the effective viscosity and ϕ for concentrated suspensions (Mueller et al., 2010; Pabst, 2004; Jeffrey and Acrivos, 1976).

All the equations considered above assume that the effective viscosity of the particulate flows only depends on the solid fractions of particles.

Previous investigation

There are many experimental studies on low-Reynolds number liquid-solid flows, and most of the experiments are for Brownian particles. This section considers two non-Brownian, low-Reynolds-number studies.

Acrivos et al. (1994) studied rigid particles with a diameter of 137.5 μm immersed in a glycerol-water mixture. Their results show shear-thinning behavior as Re increases. They explained the shear-thinning behaviors by the particle migration caused by the slight mismatch between the particle and fluid densities. By taking the settling behavior into account, their effective viscosity becomes comparable with Krieger correlations of low-Reynolds numbers ranging from 8×10^{-4} to 3×10^{-2}.

Boyer et al. (2011) studied the transition from a dense suspension to a dry granular flow (Table 1.1). They measured both normal and shear stresses using an annular shear cell with a fixed top plate. They used two types of relatively large particles (polystyrene and PMMA). However, due to the high viscosity of the fluids and the small shear rates, the particle Reynolds numbers of their experiments are much less than 1. They considered neutrally-buoyant particles and the particle migration was neglected in the analysis. Their results show good agreement with the values predicted by an effective viscosity model based on the Eilers relation.

1.3 Rheology of high-Reynolds number suspensions

For particulate flows, the inertial effects from both the solid and liquid phases become important as Re increases. However, the study of the rheology of multiphase flow with relatively large (*mm* or *cm* scale) particles and high shear rates has been limited.

Previous experimental investigation

As shown in Table 1.1, there are several studies focusing on neutrally-buoyant particles with inertial effects, with a relatively high range of Reynolds numbers.

Bagnold (1954) first investigated the normal and shear stresses in the neutrally buoyant suspensions. Bagnold (1954) used an outer-rotating rheometer with rotating bottom and top end plates (Table 1.1). Based on the experimental analysis, Bagnold summarized that there was a transition from a "macroviscous" regime, in which the shear stress, τ, depends linearly on $\dot{\gamma}$, to a "grain-inertia" regime where the shear stress, τ, has a quadratic dependence on $\dot{\gamma}$. However, these rheological measurements were implemented in the rheometer with smooth annulus walls, and rotating endplates. Due to the relatively high gap Reynolds number and small annulus height to gap ratio, the particulate flows in the rheometer cannot be assumed as simple shear flows, but are affected by secondary flows generated by the rotation of the endplates. An analysis by Hunt et al. (2002) found that the transition in the shear stresses from the "macroviscous" regime to the "grain-inertia" regime could be explained by accounting for the counter-rotating vortical structures, which have contributed significantly to the stress measurement. Therefore, Table 1.1 only includes Bagnold's results of a single solid fraction at low Reynolds numbers, which does not seem to be impacted by the secondary flow.

Particles	**d(mm)**	**Liquid**	**Re**	**Rheomoter**
Acrivos (1994)				Couette plate
PMMA [a]	0.1380	GW [b]	8×10^{-4}-3×10^{-2}	center part rotating
Boyer *et al.* (2011)				
polystyrene	0.5800	PGGM [c]	1×10^{-5}-4×10^{-4}	annular shear cell
PMMA	1.0000	TWZ [d]	4×10^{-5}-1×10^{-3}	top plate fixed
Bagnold (1954)				concentric cylinder
50% lead stearate	1.3200	glycerol	15 - 90	bottom, top,
and paraffin wax				outer rotating
Savage *et al.* (1983)				
	0.9700		7 - 54	concentric cylinder
polystyrene	1.2400	salt water	7 - 105	inner rotating
	1.7800		25 - 200	
Koos *et al.* (2012)				
polystyrene	3.3400	GW	18 - 782	concentric cylinder
nylon	6.3600	GW	50 - 720	outer rotating
SAN [e]	3.2200	GW	23 - 540	top, bottom fixed
Linares *et al.* (2017)				concentric cylinder
polystyrene	3.3400	GW	21 - 1030	outer rotating
polystyrene	3.3400	GE [f]	2 - 40	top, bottom fixed

---

[a] polymethyl methacrylate
[b] glycerol water
[c] polyethylene glycol-ran-propylene glycol monobutylether
[d] Triton X-100/water/ zinc
[e] styrene acrylonitrile
[f] glycerol ethanol

Table 1.1: Previous experiments properties considering neutrally-buoyant particles.

Following Bagnold's study, Savage and McKeown (1983) implemented torque measurements using neutrally-buoyant polystyrene particles using an inner-rotating rheometer. They observed that the shear stresses have a quadratic dependence on the shear rate. As shown in previous studies, rotating the inner rheometer cylinder could destabilize the secondary flows in the rheometer once the Reynolds number passes the low critical Reynolds number threshold. At relatively high Reynolds numbers, as the shear rate further increases, a rotational inner cylinder would facilitate the transition to turbulent flows (Mullin and Benjamin, 1980; Conway et al., 2004). Since their studies included experimental measurements higher than the critical Reynolds number, the results were affected by the turbulent effects significantly, which were not accounted for in the data analysis.

There is limited prior work at Caltech focusing on high Reynolds numbers above 10 for high-shear rate suspensions. At Caltech, Koos et al. (2012) made experimental measurements of the torques of particulate flows for Re from 18 to 782 with various solid fractions (ϕ) using a Couette-flow rheometer, which shears the liquid-solid mixture by the rotating outer cylinder to delay the transition to turbulence. The results showed that the particulate flows are Newtonian with constant viscosities. The Newtonian behavior was not expected, which appears to have related to the slip on the smooth wall of the rheometer.

Further experiments have been done by Linares et al. (2017) using the same rheometer but with roughened surface walls. The experiments involved used two different suspending fluids to explore the two Reynolds number regions with Re from 2 to 40 and Re from 21 to 1030. The liquid-solid flows showed non-Newtonian behaviors. For normalized torque measurements with Reynolds number up to 40, the results showed good agreement with current state-of-the-art simulations of $\phi = 0.1$, but were higher than the simulations for $\phi = 0.2$ and $\phi = 0.3$ (Linares et al., 2017). However, without further measurements in liquid and particle fluctuating velocities, it is impossible to determine the reasons behind the experimental difference.

1.4 Rheology of intermediate-Reynolds-number suspensions

The rheological properties of particulate flows are affected by the movements of particles in the suspending liquid, in which the collisions between particles, and the viscous and inertial interactions of the suspension all contribute to the mechanics of the multiphase flows. There are two limiting types of the fluid-solid flows: granular flows (with negligible viscous effects) in which the stresses depend on collisions and friction between particles; and suspension mixtures (with negligible inertial effects) in which the stresses are dominated by the viscous effect of the fluid. However, between the two extreme cases, there are sparse experimental data in a considerable regime involving moderate Reynolds numbers where both viscous and inertial effects are important. Hence, the mechanism of these multiphase flows with inertia to date is not fully understood. To develop rheological models for liquid-solid flows and to ensure accuracy, it is crucial to have sufficient experimental data to validate the constitutive relations.

Figure 1.1 presents a map considering particle Reynolds number, Re, as well as the solid fraction, ϕ, to summarize the regions covered in previous experimental investigations, as well as the range studied in current work. As shown in the map, the

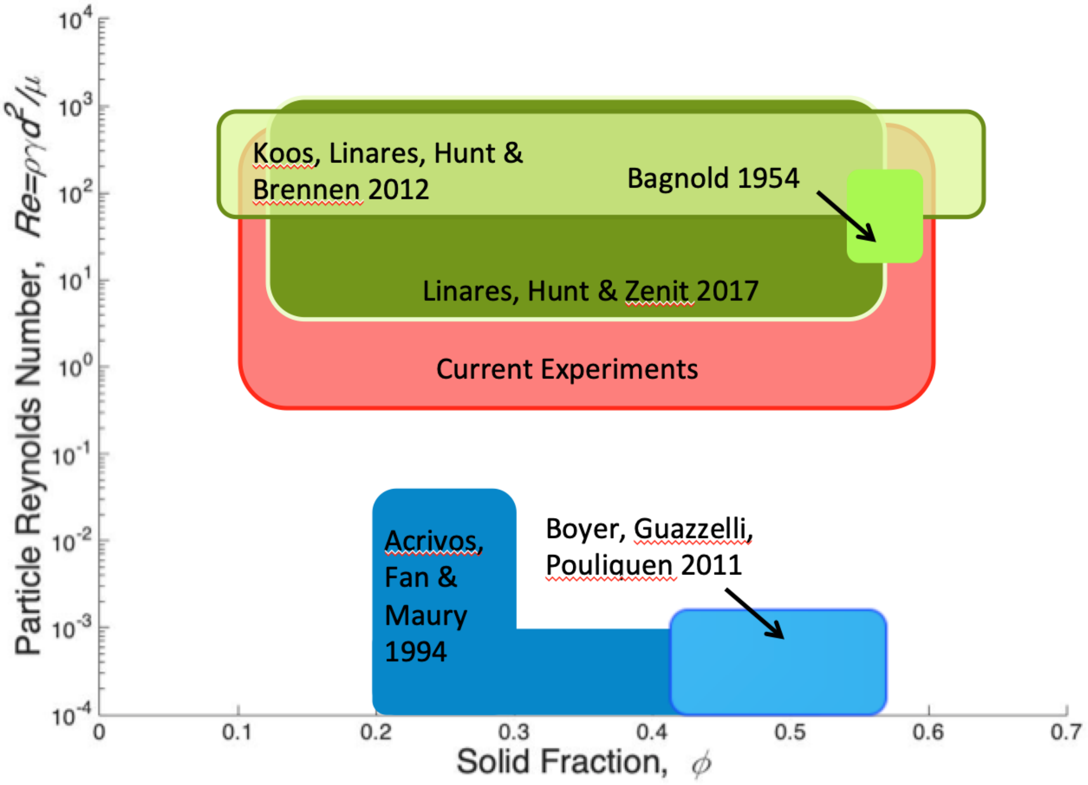

Figure 1.1: Map considering particle Reynolds number, Re, as well as solid fraction, ϕ for prior and current experiments of neutrally-buoyant particles. Properties of previous experiments are summarized in Table 1.1

current experiments cover a notably large regime including intermediate Reynolds numbers, $0.1 < Re < 10$. This figure includes two low Reynolds number studies from Acrivos et al. (1994) and Boyer et al. (2011). At higher Re regimes, this figure also includes the work done by Koos (2009) and Linares (2015) at Caltech.

Numerical Studies

In addition to the extensive numerical studies of low-Reynolds-number liquid-solid flows, there are numerical studies that investigated the inertial effects on the neutrally-buoyant suspensions in intermediate Reynolds number liquid-solid flows. These simulations calculate the total stresses in terms of ϕ and Re (Kulkarni and Morris, 2008; Rahmani et al., 2018; Picano et al., 2013; Yeo and Maxey, 2013).

Kulkarni and Morris (2008) considered liquid-solid mixtures in a wall-bounded simple-shear flow for Re from 0.04 to 16 (this paper defined Re based on radius rather than diameter), and calculated the stress contribution from the solid phase to

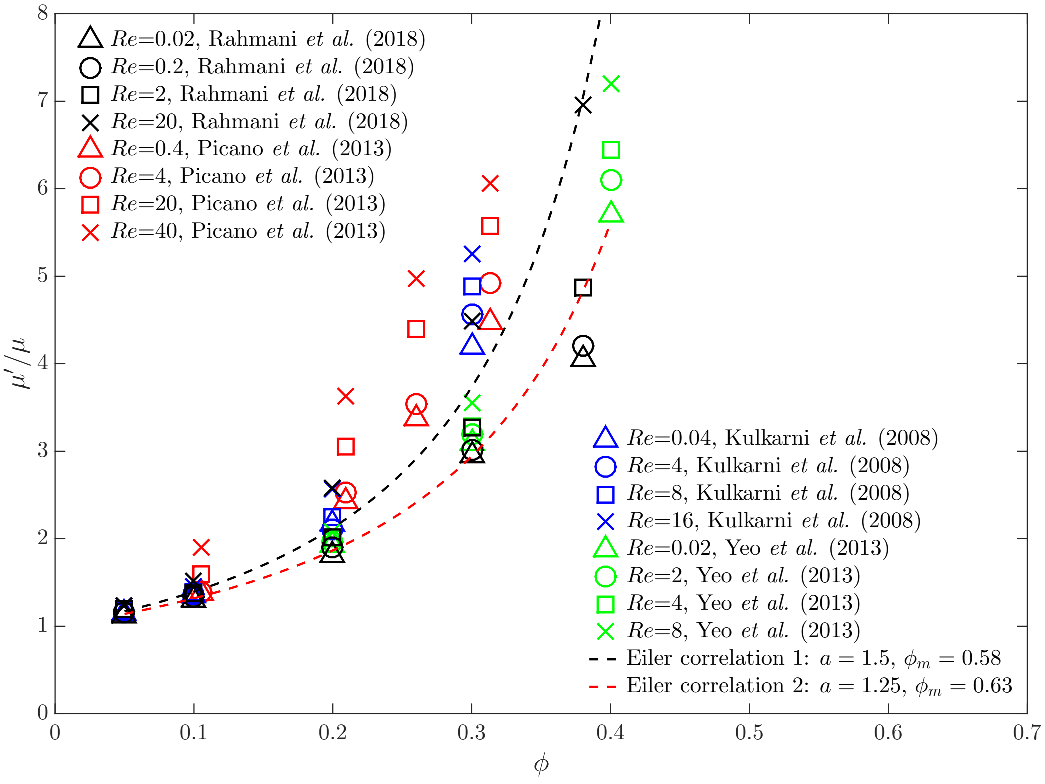

Figure 1.2: Effective viscosity (μ'/μ) of particulate flows in terms of solid fraction (ϕ) from numerical studies. The red and the black dashed lines are the Eilers relations.

the bulk stress with the lattice Boltzmann method. The simulation results of the effective viscosity are presented in Figure 1.2 in terms of solid fractions, with labeled particle Reynolds numbers (Rahmani et al., 2018; Yeo and Maxey, 2013; Picano et al., 2013; Kulkarni and Morris, 2008). For the lowest Re of 0.04, their results of effective viscosity show good agreement with the effective viscosity predicted by the Eilers relation. At the state of 10% and 20% solid fractions, the calculated effective viscosity increases as Re increases. But at the state of 30% solid fraction, the simulation results show an approximately 5% decrease in effective viscosity for Re less than 0.4, and an approximately 30% increase for Re greater than 10 when compared to the effective viscosity at Re = 0.4. Kulkarni and Morris (2008) explained that the slight shear thinning behavior and the following shear thickening behavior were caused by the change of the particle structures in the liquid-solid flows.

Another simulation study from Haddadi and Morris (2014) also used the lattice-Boltzmann method (LBM) to study the neutrally-buoyant particles considering simple shear flows, covering a particle Reynolds number regime from 0.02 to 20, and solid fraction from 0.1 to 0.35. In the examination of the stress mechanisms of the suspension, they calculated the surface traction term, the acceleration term, and the Reynolds stress term. They found that the stresslet and the Reynolds stress contribute significantly to the calculated stresses of the liquid-solid mixture, and the effects of the acceleration stress are found to be negligible.

Yeo and Maxey (2013) calculated the effective viscosity in a linear shear flow for $0.02 < Re < 8$. They implemented a "lubrication-corrected force-coupling method (FCM)" to estimate the shear stresses for solid fractions from 20% to 40%. As shown in Figure 1.2, their results of effective viscosity increase as the Re increases. However, the results is smaller in comparison with the calculations from Kulkarni and Morris (2008). In their calculations, Yeo and Maxey (2013) excluded Reynolds stresses generated from the velocity fluctuations, and they estimated that the Reynolds stresses are negligible as compared to the stresses from the particles.

Another study by Picano et al. (2013) calculated μ'/μ for wall-bounded liquid-solid flows over $0.4 < Re < 40$ and $11\% < \phi < 31\%$. They computed the shear stresses with an "immersed boundary method". Specifically, Picano et al. (2013) divided the shear stress on the wall by the average shear rate. Their results are slightly higher than those in the study of Kulkarni and Morris (2008).

Rahmani et al. (2018) considers neutrally-buoyant suspensions of particles in the Couette flow, with a Re regime from 0.002 to 20, and solid fractions from 0.5 to 0.38. They used the "distributed Lagrange multiplier and fictitious domain" methods to simulate the motions of the particles in the liquid. For $\phi = 10\%$ and $\phi = 20\%$, the results from Rahmani et al. (2018) show good agreements with the simulations from Kulkarni and Morris (2008) for Re from 0.04 to 16. At the state of $Re = 20$ and $\phi = 30\%$, their results of effective viscosity increase substantially compared to numerical results considering low Re, but appear to be lower than the values found by Kulkarni and Morris (2008) with similar Re values. In the examination of the inertial effects of the fluids and the particles, they estimated that particle inertia plays a dominant role as compared to fluid inertia. In addition, they found that the velocity fluctuations associated with the Reynolds stresses do not contribute substantially to the calculated stress of the suspension over the particle Reynolds number regimes tested.

At the state of smallest solid fractions ($\phi < 0.2$) and Re less than 20, all the simulation results plotted in Figure 1.2 in terms of μ'/μ with respect to ϕ compares well with the Eilers relation 2 ($\mu' = [1 + a\phi/(1 - \phi/\phi_m)]^2$) using $a = 1.25$ and $\phi_m = 0.63$. However, at the solid fraction of 0.2, the values from Picano et al. (2013) starts to deviate from the Eilers correaltion 2, while the rest simulations still compare well with the Eilers correlation 2. For $\phi = 30\%$, the results of Picano et al. (2013) show increased dependence on Re, and their results considering smallest Re are best modelled using Eilers relationship 1 ($\mu' = [1 + a\phi/(1 - \phi/\phi_m)]^2$ using $a = 1.5$ and $\phi_m = 0.58$).

There are some differences between experimental and simulation investigations. In the numerical environment, the suspending liquid density and the particle density are set to be equal. However, for conditions in experiments, it is challenging to achieve a perfectly neutrally-buoyant state, given the difficulty to match particle and fluid densities due to the temperature dependence of the suspending liquid densities. The challenge to fix the concentration of each component in mixed fluid introduces additional discrepancies in the fluid and solid phase density match. As a result, the settling and floating of the particles can have a substantial impact on the measurements of effective viscosity (Acrivos et al., 1994; Fall et al., 2009). In addition, due to the rheometer design, secondary flows and laminar-turbulent transition may occur in the Couette flow device, making it challenging to have a simple shear flow (many simulations considered simple shear flows) for experimental study. All these factors contribute to complicating the comparisons between the experimental and numerical results.

1.5 Particle interactions in liquid-solid flows

The solid phase in the liquid-solid flow inevitably introduces particle velocity fluctuation and particle collisions into the multiphase flow. As the Re is further increased, the increasing inertial interactions in the particulate flow may lead to the laminar-turbulent transition (Batchelor, 1970). These fluctuations and collisions from the particles can excite instabilities in the multiphase mixture that may either suppress or facilitate the turbulent transition (Gore and Crowe, 1991; Matas et al., 2003). At relatively high Reynolds numbers, the particle velocity fluctuations, the particle collisions, as well as the turbulence, all have contributed to the torque measurement. To complement the torque measurement and flow visualization in rheological studies, it is crucial to study the roles of fluctuating particle velocities and particle collisions on the stresses and on the transition to turbulent flow.

Unlike many other rheometers in the scientific community, the Caltech concentric rheometer was purposely designed to shear the large (*mm* scale) particles. The rheometer's ability to accommodate relatively big particles, combined with its potential to implement flow visualization, along with velocity and pressure measurements, gives the opportunity for velocity and pressure data acquisitions to further correlate to the torque in intermediate-Reynolds-number liquid-solid flows.

Particle resuspension

In addition to the neutrally-buoyant particle experiments, particles with a higher density as compared to the surrounding liquid are important to further study the impact of the additional solid-phase inertia on the torque measurement. Theoretically, there are several methods to introduce additional inertial effects to the rheological experiments, including increasing shear rate, increasing particle size, decreasing fluid viscosity, and increasing particle density. However, in practice, the particle size is limited by the gap size of the concentric rheometer. The infinitely large shear rate in the rheometer is untenable, due to the electric motor required to achieve the desired shear rate would make such an experimental setup prohibitively expensive. Instead, it must turn to increase the particle density or decrease the fluid viscosity.

Once the particle density is different from the suspending fluid density, the particles could either float or settle based on the ratio of ρ_p/ρ_f and the shearing condition. As a result, the suspensions are no longer uniformly distributed in the liquid body, and the mixture becomes inhomogeneous. As the shear rate increases, the settling particles in the suspending fluid could be resuspended, which may also lead to radial variation in solid fractions. The phenomena of particle settling and the following resuspension can significantly change the properties of liquid-solid flows.

Table 1.2 presents three resuspension experiments using a particle to fluid density ratio higher than 1. The particle properties, the fluid properties, and the Re range examined are highlighted in the table.

Among these liquid-solid flow experiments using rheometers, there are some studies considered particle collisions, especially at high shear rates. Hanes and Inman (1985) mixed glass bead with water in a device with an annular gap driven by the rotation of the bottom plate. At the state of solid fractions greater than 55%, they found a static layer of particles near the bottom. Above the static layer, the suspension can be easily sheared and deformed rapidly. Prasad and Kytömaa (1995) used an experimental device to study the transition in the particulate flow from

Particles	**d(mm)**	**Re**	ρ_p/ρ	**Rheomoter**
Prasad *et al.* (1995)				
glass beads	2.000	1.37-13.70	2.09	annular gap
acrylic	3.175	0.09 - 2.89	1.12	bottom rotating
Hanes *et al.* (1985)				
	1.100	43.00 - 317.00	2.48	annular gap
glass beads	1.850	118.00 - 434.00	2.78	inner, outer
				bottom rotating
Linares Thesis (2015)				
polystyrene	3.340	17.19 - 744.80	1.05	concentric cylinder
polyester	2.930	2.99 - 1099.93	1.2/1.4	top, bottom fixed

Table 1.2: Previous experiments properties considering settling particles.

a static regime to a viscous regime with acrylic particles and glass beads at high solids fraction (from 49.3% to 56.1%). Their experimental apparatus consisted of an annular gap with a rotating bottom end plate and a fixed top end plate; the top plate was therefore used for the measurement of stress. At the constant normal stress condition, they revealed that the maximum packing solid fraction (ϕ_m), at which the particulate flow cannot be sheared, has no dependence on the fluid dynamic viscosity.

At Caltech, Linares (2015) has done preliminary experiments to study the settling particles using the same rheometer mentioned in Section 1.3. As shown in Table 1.1, Linares used both polystyrene (3.34 mm) and polyester particles (2.93 mm) with relative densities of 1.05, 1.2, and 1.4. At the beginning of the experiment, the dense particles were uniformly placed at the bottom of the annulus of the rheometer and formed a particle bed. Once the particles were mixed with the fluid, the settled particles reached a loose packing state. With an increasing shear rate, applied by the rotation of the outer cylinder, the particles resuspended and the particle bed expanded to reach a steady state, in which the torque is measured using the same experimental apparatus designed for neutrally-buoyant experiments. To quantify such changes, Linares also implemented flow visualization in the Caltech Couette-flow device to measure the variations in particle solid fraction. To do so, a transparent inner cylinder with the same radius value as r_i was constructed and used to replace the top and the middle testing cylinders of the Caltech Couette flow device. A camera was then placed inside the transparent cylinder, and the bed height was recorded.

Particle collisions

Particle collisions occurring in the liquid-solid flows are assumed to contribute to the measured torque staring with a Stokes number higher than 10. Many studies have shown that particle-wall and particle-particle collisions are important to determine the effective viscosity of liquid-solid flows (Joseph et al., 2001; Ruiz-Angulo and Hunt, 2010; Yang and Hunt, 2006).

Some earlier work on particle collisions, though may not be implemented in a rheometer, has also shed light on how particle collisions contribute to the measured stresses. In prior investigations at Caltech, Zenit et al. (1997) measured particle pressures in both concurrent and countercurrent flows of liquid-solid flows. The experiment used a PCB dynamic pressure transducer to measure pressures generated by the collision between the particles, as well as collisions between the particle and the wall. The two types of collisions were then determined based on the length of the pressure pulses. Then Zenit and Hunt (1999) incorporated a high-speed camera into the apparatus and synchronized the pressure sensor. The measured collisional pressure was consisted of both the direct collisions with pressure transducers and the collisions internal to the flow that radiated an impulse to the transducer. In terms of the strength of the pressure pulse and the decay of the signal strength, the experimental results showed a qualitative agreement with models considering inviscid flow theory.

Joseph et al. (2001) implemented experiments considering collisions of a single particle and a rigid wall immersed in a viscous fluid. The experimental setup used a pendulum immersed in the fluid to control the particle's trajectory with an initial inclination angle. Once the particle was released, a camera was employed to capture the resulting collision. Following the study of Joseph, Ruiz-Angulo and Hunt (2010) employed a similar experimental apparatus to further investigate the rebounding behaviors of particles after the collisions with a deformable surface immersed in the viscous fluid. Another experiment implemented by Yang and Hunt (2006) studied the collisions between the particles in fluid, including both the head-on and oblique collisions of two particles.

In those studies, the Stokes number is used to study the particle collisions in the fluids, and the coefficient of restitution, e, is used to describe the energy loss during the collision. It was found that the coefficient of restitution depends strongly on the Stokes number. For Stokes number higher than 2000, the effects from the liquid phase become negligible, and the collision became almost elastic, leading to a value of e close to 1. However, with a decreasing Stokes number resulting from the effects of decreasing particle inertia and increasing fluid viscosity, the particle is less likely to rebound in the viscous liquid. These studies concluded that there existed a critical particle Stokes number around 10. Once the Stokes number is less 10, no rebounding behaviors of the particle from the surface were observed; the kinetic energy associated with the particle movement and the impact of the collision are damped out by the viscous liquid.

A numerical study from Zhou and Prosperetti (2020) used resolved simulations to examine the inertial effects of non-neutrally buoyant suspensions. This study examines the particle-fluid mixture with varying density ratios between 2.5 and 10, and solid fractions from 5% to 33%, considering Re (They defined the Re as $Re_p = 4a^2\dot{\gamma}/\nu$, which is equivalent to $Re = \rho\dot{\gamma}d^2/\mu$ presented in this thesis) of 20 and 40. They simulated a simple shear flow generated by two plates, moving with the same velocity magnitudes, but in the opposite directions. Their study calculated the relative contributions to the effective viscosity from the fluid phase, the stresslet, and the particle collisions. They found that for higher density ratio and higher volume fraction, the intense collisional activities promote the velocity fluctuations and contribute to the effective viscosity. At the Re of 40, for the density ratios of 5 and 10, their results show that the collisional components of the effective viscosity dominate.

1.6 Thesis outline

The current work aims to study the liquid-solid flows with both inertial and viscous effects, as well as the underlying mechanisms of suspension stresses, with a focus to extend the particle Reynolds numbers to previously-untested regimes.

The description of the Caltech Couette flow device and the experimental methods are presented in Chapter 2. The suspending fluids and the particle properties are also discussed in Section 2.2 and Section 2.3.

Experiments were conducted using multiple pure fluids to cover a wide regime of gap Reynolds numbers. The results of the direct torque measurements and the normalized torques of pure fluids are presented and discussed in Chapter 3. The hydrodynamic instabilities of the pure fluids are also analyzed in Section 3.1.

The direct torque measurements and the normalized torques for neutrally-buoyant particles are detailed in Chapter 4. A particle Reynolds number (Re') based on the the particle diameter and the maximum shear flow velocity is proposed to examine the effective viscosity of the particulate flows, and the rheological models considering measurements before transition are presented in Section 4.5. Comparisons between the current experimental measurements and the results of the previous experimental and simulation studies are presented in Section 4.7 and Section 4.8 separately.

Results of rheological measurements for non-neutrally buoyant suspension are detailed in Chapter 5. The same particles tested in Chapter 4 were immersed in water with a density ratio of 1.05 to further examine the effects of increased particle inertia on the torque measurements.

Finally, Chapter 6 summarizes the findings in the pure fluids, neutrally-buoyant, and non-neutrally buoyant experiments. Section 6.4 also discusses the potential topics for future work.

Chapter 2

EXPERIMENTAL DEVICES AND METHODS

The current experiments are designed to expand the rheological torque measurements to previously untested Reynolds and Stokes number regions for both neutrally-buoyant and settling particles. Subsequently, the Caltech Couette flow device has been improved for the experiments using 1.27 *mm* polystyrene particles.

This chapter consists of three major parts corresponding to the measurements of torque, the suspending fluids, and the particles separately. The rheometer and the methods used to measure torque for small particles are described in Section 2.1. Following that, the fluids are discussed in Section 2.2. This chapter also specifies the particle properties in Section 2.3.

2.1 Coaxial-cylinder rheometer

This study uses a stainless-steel coaxial-cylinder rheometer that was designed to look at multiphase flow with inertia. The rheometer was designed and constructed by the Hunt research group at Caltech and described in Koos (2009).

Figure 2.1 shows the cross-sectional view of the Caltech Couette flow device. The Caltech Couette flow device has two concentric cylinders: the outer cylinder and the inner cylinder. The bottom part of the outer cylinder is connected to an electric motor by a rubber belt. The rotational speed of the electric motor can be adjusted with 9 levels. More specifically, the inner cylinder has three subsystems: the top cylinder, the middle testing cylinder, and the bottom cylinder. The top and the bottom cylinders are fixed on the experimental frame. The middle testing cylinder is connected to a freely-rotating central shaft. To allow free rotation and to prevent the particles from entering the inner cylinder, the top and bottom cylinders are separated from the middle testing cylinder by small gaps. Two large sets of ball bearings are also mounted between the top and bottom cylinders and the rotational outer cylinder to further reduce the friction. The central shaft and the fixed guard cylinders are then sealed with O-rings to prevent the leaking of fluid. Once the components are properly sealed and lubricated, the rotating outer cylinder shear the liquid-solid mixture located in the annulus of the rheometer. The torque generated by the particulate flow is measured by the middle testing cylinder.

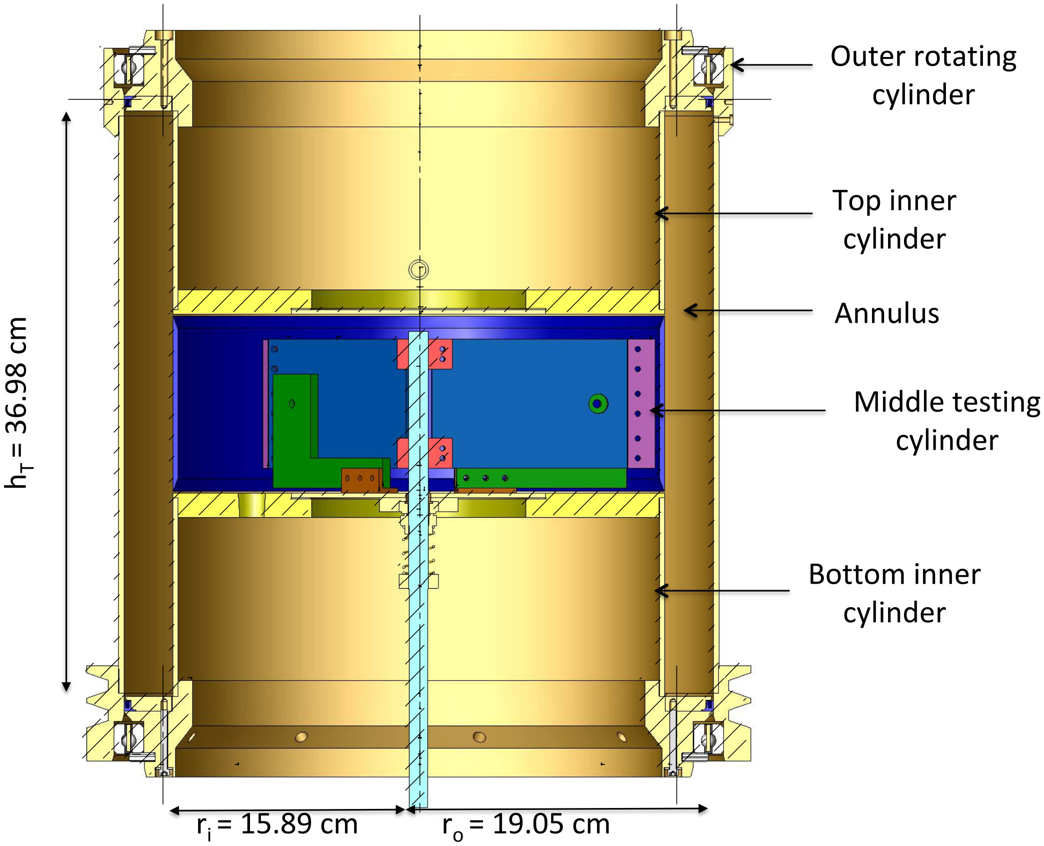

Figure 2.1: Schematic of the Caltech Couette flow device. The outer cylinder is connected to the electric motor by a belt. The schematic is from Koos Caltech thesis (Koos, 2009).

To reduce the particle slip near the annulus wall, the elliptical polystyrene particles (3.34 *mm* effective diameter) have been used to rough the annulus surface walls of the inner and the outer cylinders. The cylinder surfaces are firstly covered with a thin layer of waterproof vinyl sticker sheets, which are often used in swimming pools. Then the polystyrene particles are glued uniformly on the sticker sheets. The rheometer properties and the corresponding dimensions considering rough walls are summarized in Table 2.1. The height of the rheometer annulus, h_T, is 0.37 m. The height of the top and the bottom cylinders are both 0.13 m. The height of the middle testing cylinder, H, is 0.11 m. The outer radius of the annulus, r_o, is 0.19 m. The inner radius of the annulus, r_i, is 0.16 m. The size of the gap of the annulus, b, is 0.025 m. The maximum rotational speed of the outer cylinder, ω, is 16 rad s^{-1}. The maximum shear rate of the rheometer, $\dot{\gamma} = 2\omega r_o^2/(r_o^2 - r_i^2)$, is 128.93 s^{-1}.

Rheometer Properties	Dimensions
Height of the annulus: h_T	0.37 m
Height of the top&bottom cylinders	0.13 m
Height of the middle testing cylinder: H	0.11 m
Outer radius of the annulus: r_o	0.19 m
Inner radius of the annulus: r_i	0.16 m
Size of the gap of the annulus: (b)	0.025 m
Ratio of annulus height to annulus gap	15
Maximum rotational speed: ω	16 rad s^{-1}
Fully turbulent gap Reynolds number	1.10×10^4

Table 2.1: Dimensions of the Caltech Couette flow device with rough walls

Rheometer torque measurements

To improve the measurement accuracy and the experiment repeatability, a new data acquisition system using a torque sensor has been built and validated for the rheometer.

The axial shaft supporting the floating cylinder has been extended to connect to a reaction torque sensor (Omegadyne, Inc.), which is installed on the stationary frame of the experimental apparatus (Figure 2.2). Due to the shear of the liquid-solid mixture, the test cylinder rotates slightly but its rotation is constrained by the calibrated reaction torque sensor. The torque applied on the test cylinder is then measured by the torque sensor. The signal from the torque sensor is then processed by a lab-built data acquisition system, and displayed and recorded in a code that can monitor the torque measurement in a real-time manner. With the torque-monitoring interface on the computer, the system can determine whether the flow in the annulus enters a steady state, and continuously monitors the flow behavior during the experiment. With this design, the rheometer can directly measure the torque without having to subtract out the friction of the bearing.

For each data point of torque measurement, it is the average value of at least five individual experiments using pure fluids or liquid-solid mixtures. The error bars represent the standard deviation of the rheological measurements recorded for each experiment. For each individual measurement, the average torque sensor reading during the steady state, the fluid temperature, and the fluid density are monitored and recorded. The average torque sensor reading is then converted to torque $(N.m)$ based on the different sensor calibration curves. There are minor density differences (less

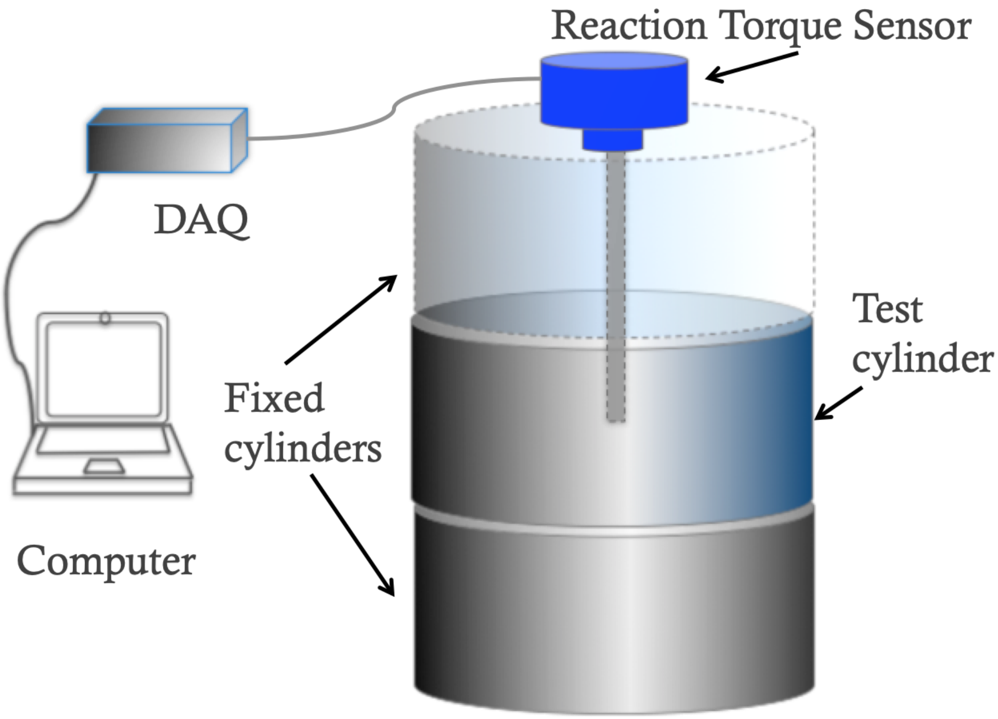

Figure 2.2: Torque measurement system. This image only shows the inner cylinders. In the side view of the inner cylinders, the central shaft supporting the test cylinder is extended to connect to a reaction torque sensor, which is installed on a stationary apparatus frame. The signal captured by the sensor is processed by a data acquisition system and recorded on a computer. The schematic of the cylinders is from Koos Caltech thesis (Koos, 2009).

than 1%) between the particles and the fluids. This minor mismatching between the particle and fluid densities caused by temperature change and particle properties could lead to the floating and settling of the particles, which affects the effective viscosity measurement (Acrivos et al., 1994). To address this issue, temperatures are monitored and measurement running time is controlled to avoid significant changes in fluid temperature and the corresponding changes in fluid density and viscosity. Moreover, before the torque measurement, the rheometer is run at the maximum speed for some time to mix the neutrally buoyant particles to reduce the impact of settling and flotation of particles.

In addition to the regular experimental procedures, additional operations are taken to ensure the consistency of the density and the viscosity of the glycerol-ethanol mixture throughout the experiment. The goal for these steps is to ensure the neutrally-buoyant state of the liquid-solid mixture and the measurement precision. Due to the high evaporation rate of ethanol and the high density sensitivity to temperature variation of the 51% glycerol-ethanol mixture, a minor glycerol-ethanol composition variation in the glycerol-ethanol mixture caused by temperature change may lead to obvious changes in fluid density and the corresponding fluid dynamic viscosity. As a result, the fluid density change affects the neutrally buoyant state of suspending particles. Therefore, after each individual experiment, the glycerol-ethanol fluid density is tested using a hydrometer. Then the glycerol-ethanol fluid is remixed with pure glycerol or pure ethanol to make sure that the fluid density is at 1050 kg/m^3, matching the particle density. Besides the density control of the fluid, the temperature of the mixture is measured for each data point. The fluid temperature for all the rheological measurements using glycerol-ethanol mixture is controlled between 20 °C and 21.1 °C.

There are differences between the temperature measurements for experiments using SAN particles and polystyrene particles. For the temperature measurements of rheological experiments using SAN particles, the suspending fluid is collected through the draining holes located at the bottom of the annulus, then the temperature of the liquid is recorded. Unlike the temperature measurements of particulate flows with SAN particles, the temperature of the suspending fluids in the annulus considering 1.27 *mm* polystyrene particles cannot be directly measured using the thermometer since the draining holes are sealed. The temperature of the same suspending fluid inside the middle testing cylinder was then measured near the gap between the top and the middle testing cylinders. Therefore, the uncertainty of the temperature measurements is taken into account in the error bars of the normalized results of polystyrene particles, especially for the 10% solid fraction measurements, which have 90% glycerol-ethanol volume fraction.

Experimental setup for small polystyrene particles

The rheometer has been upgraded to introduce small particles to the rheometer without letting the particles get stuck in the gaps between the cylinders.

Once the upgraded reaction torque sensor is installed, the central shaft supporting the middle testing cylinder is constrained by the torque sensor, but can still measure the torque accurately as discussed in Chapter 3. With the improvement of the torque sensor, it becomes possible to adjust the gap size between the cylinders as low as 1 *mm* at a relatively static state of the middle testing cylinder. For the setup of the 3.22 *mm* SAN particles, without the reaction torque sensor, the middle testing cylinder can rotate 360 degrees without any obstacles. Due to the machining tolerance of the bottom cylinder, the surface of the bottom cylinder is not perfectly flat, and it can affect the 360-degree rotation of the middle testing cylinder if the gap size is extremely small. Therefore, unlike the SAN particle experiment, with the reaction torque sensor uninstalled, the gap setup for the smaller polystyrene particles cannot allow a 360-degree free rotation for the middle testing cylinder, instead, it can let the middle testing cylinder rotate freely for approximately 80 degrees. However, once the reaction torque sensor is connected with the middle testing cylinder under the 1 *mm* gap size setup, the testing cylinder can rotate freely within the 80 degrees range (the observed maximum rotation angles of the middle testing cylinder during the experiments are ± 5 degrees.), without introducing extra friction to the system. In addition, the long bolts supporting the top cylinder are also replaced with improved bolts with finer threads to make precise adjusts of the gap sizes. Once the gap sizes are adjusted, to test the gap between the cylinders, an aluminum plate with 1.01 *mm* thickness cannot go through the gap, but an aluminum foil with a thickness of 0.91 *mm* can pass through the gap in all directions. It is challenging to set up the gap size the first time even for the 3.22 *mm* SAN particles. Therefore, it is suggested to observe and adjust the gap size without the outer cylinder installed before assembling the entire rheometer.

The purpose of the remaining small gaps between the cylinders is to prevent particles from entering the test cylinder without introducing friction. Besides the adjustment of the gap size, the draining holes located at the bottom of the rheometer annulus are sealed with water-proof materials and tapes to prevent the small polystyrene particles from entering the draining pipes. After the seal of the draining holes, the suspending liquids are drained using a waterproof vacuum machine inside the cylinders during the experiments.

After the gaps between the cylinders are set up, the pure fluid experiments using pure water and glycerol water mixtures are repeated to validate the torque measurements' accuracy. The results of the pure fluids using the small gaps match very well with previous pure fluids results, and the pure fluid measurements are discussed in detail in the contexts of Chapter 3. The remaining experimental procedures are similar to the measurements of pure fluids and SAN particles.

For future experimental improvements, one idea is to cover the cylinder gaps using fine-mesh filter nets, which are typically used for the separation of small particles and liquid. The filter bags (0.38 *mm* mesh size), though not directly mounted on the rheometer for this study, are frequently used to recycle the particles after each experiment. The filtering nets are flexible such that suspending fluids can go through, but the particles cannot pass through.

Outer cylinder speed measurement

This section introduces a method to measure the rotational speed of the outer cylinder by a laser sensor (Neiko, Inc.).

Figure 2.3 presents the speed measurement system for the outer cylinder. To enhance the measurement accuracy, a black stripe on the upper edge of the outer cylinder was painted to improve color contrast between the outer cylinder and the laser sensor targets. Eight reflective targets were then glued on the black stripe with equal distance to further improve the accuracy. The laser sensor was installed on the rheometer frame, with the same height as compared to the reflective targets. Once the outer cylinder starts rotating, the laser beam points to the reflective mark on the black stripe. The rotational speed recorded by the laser sensor is then transformed into angular velocity by taking the number of reflective targets into account.

The shear rate in the rheological experiments is determined based on the angular velocity acquired by the speed measurement system. Considering the cylindrical Caltech Couette-flow device with the rotating outer cylinder, the corresponding shear rate is defined as:

$$\dot{\gamma} = \frac{2\omega r_o^2}{r_o^2 - r_i^2}, \tag{2.1}$$

The maximum and the minimum rotational speeds of the outer cylinder, and the corresponding maximum and minimum shear rates ($\dot{\gamma}$), are slightly different for each individual experiment. There are several factors affecting the maximum and the minimum shear rates, including the tightness of the belt connecting the motor and the outer-rotating cylinder, the maintenance state of the bearing, the solid fractions, and the types of the particles and fluids. Typically, the rheometer needs to overcome larger friction to rotate for large particles immersed in high-viscosity fluids with high solid fractions in comparison to the case of small particles immersed in low-viscosity fluids with low solid fractions. Therefore, the small particles immersed in low-viscosity fluids tend to have lower minimum shear rates at the steady state. In addition, the belt cannot be too tight to introduce excessive loading stress to the rheometer frame, and cannot be too loose to allow the slip of the outer-rotating cylinder. The shear rates for each experiment are presented and discussed in detail in the chapters for the results of rheological measurements.

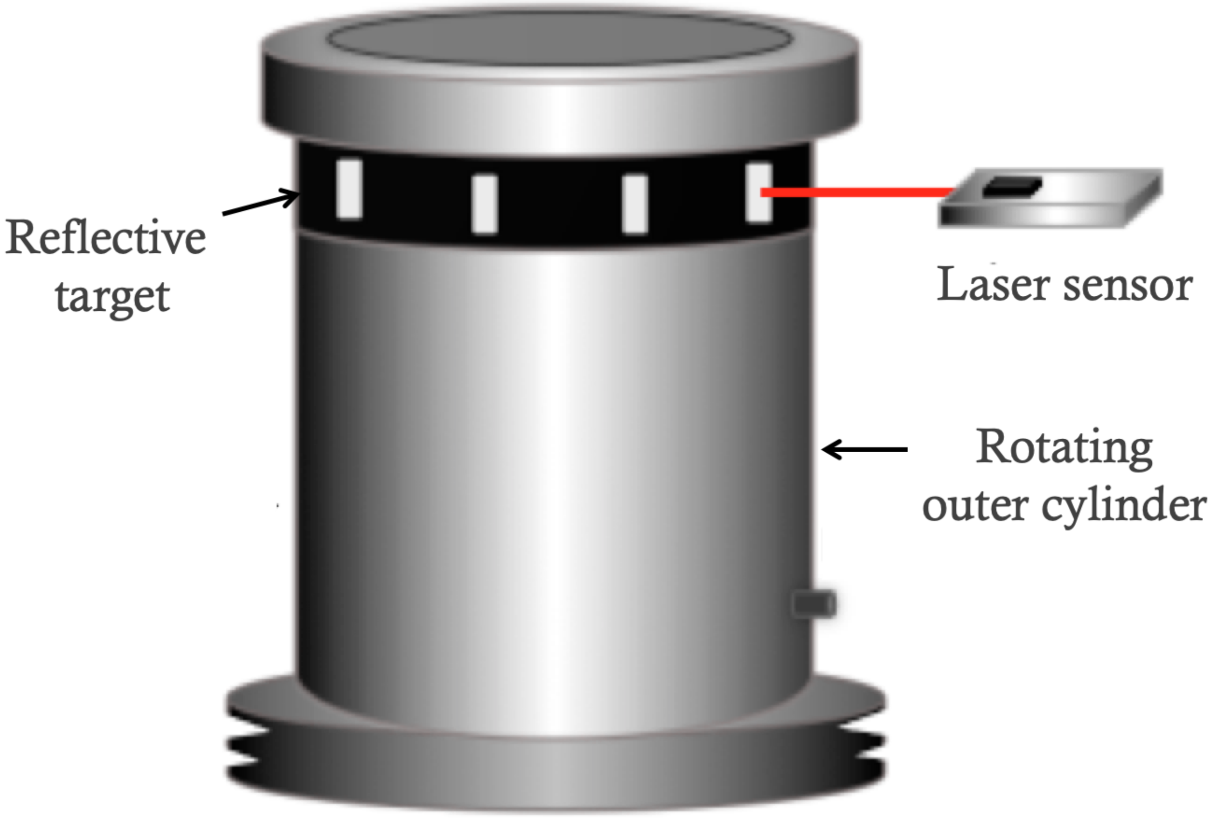

Figure 2.3: The speed measurement system for the outer cylinder. There are 8 reflective targets. The laser sensor measures the rotational speed of the outer cylinder. The sketch is from Linares Caltech thesis (Linares, 2015).

Sensor calibration

The reaction torque sensors used for torque measurement were calibrated on a different experimental apparatus with the known torque arm and applied force perpendicular to the arm. The same data acquisition system was used to capture the signal during the calibration process.

The calibration of the torque sensor was implemented by applying torques generated by known masses on the reaction torque sensor. The torque sensor was fixed on a bench vise, with a lab-fabricated cap connecting the sensor and a long aluminum bar. The cap was rotated to a position that holds the aluminum bar firmly and horizontally. Before each calibration measurement, the data acquisition system measured and recorded the initial reading generated by the torque applied by the weight of the aluminum bar. Then 11 mass sets ranging from 1 g to 400 g were placed on the end of the aluminum bar. The distance from the center of the known mass to the center of the torque sensor was measured for every data point. The output reading for each mass is the final sensor reading subtracts the initial reading. The torque corresponding to the sensor readout is the known mass weight multiplied by the measured distance.

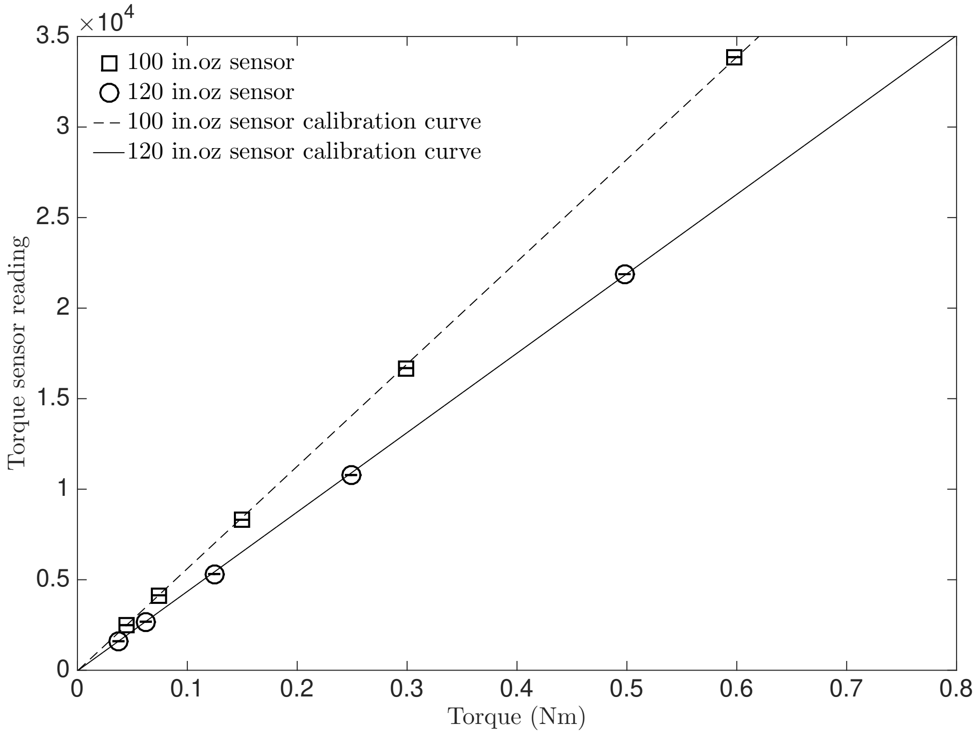

Figure 2.4: Reaction torque sensor reading vs. torque from 0 to 0.8 Nm.

Figure 2.4 presents the reaction sensor reading with respect to the applied torque on the calibration apparatus with a range from 0 to 0.8 Nm. The calibration data points and the corresponding fitting curves are presented in the plot for 100 in.oz and 120 in.oz torque sensors separately. The sensor reading is proportional to the applied torque with a linear calibration curve passing through the origin of the coordinates. The linear relationships are consistent with the manufacturer's instructional manuals. The error bar was generated and plotted based on the maximum and the minimum sensor reading for each data point. On the stationary calibration apparatus, the percentage of reading variation is less than 0.001%, indicating that the torque sensor can perform reliable measurements over the torque range of interest (0 to 0.8 Nm).

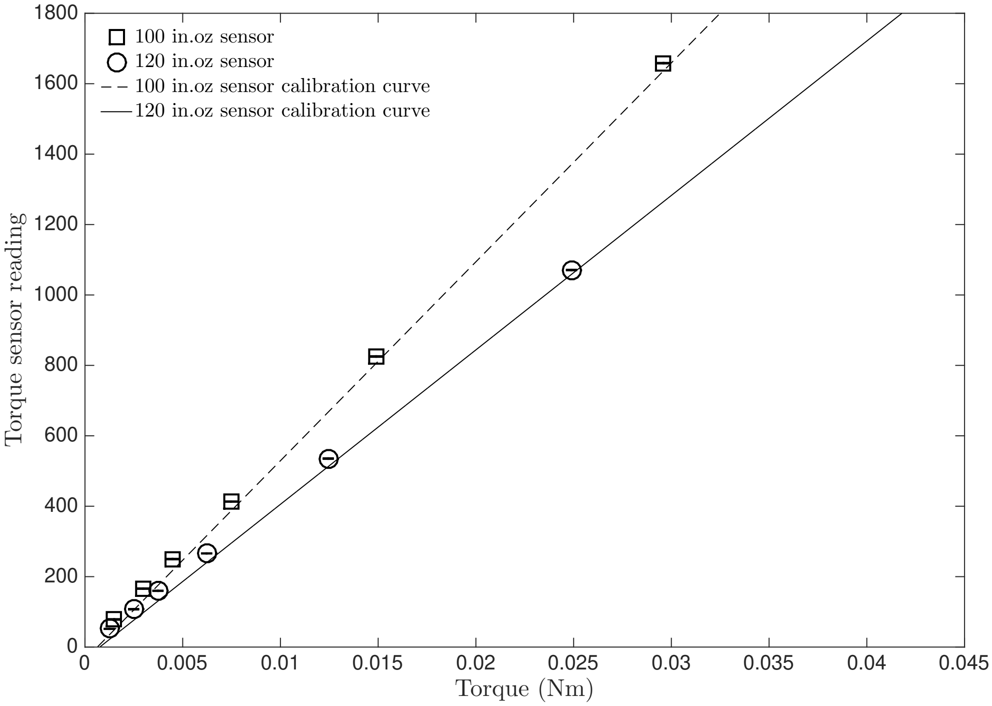

Figure 2.5: Reaction torque sensor reading vs. torque from 0 to 0.045 Nm.

To further test the resolution of the torque sensor, additional calibration experiments considering small torque loading were performed (Figure 2.5). For those data points close to the origin of the coordinates, they still align well with the linear calibration curves that best fit the results. To examine the sensitivity, the errors of these data points were plotted under small torque loading. The maximum and the minimum reading for each calibration point deviate with a limited magnitude from the mean output (less than 0.01%).

Therefore, the calibration result concludes that the sensors selected for the rheological experiments can cover the desired range of torque measurement with consistent linear calibration curves, without introducing additional uncertainty to the experimental measurements. Moreover, the sensors have enough resolution to capture the torque variation at the lowest rotational speed of the Caltech Couette flow device.

Even though the sensor has enough accuracy for torque measurement of $\dot{\gamma}> 10$ s^{-1}, the torque sensor has a limitation for estimation of M_o generated by the fitting curves at $\dot{\gamma} = 0\ s^{-1}$, which is examined in detail in chapters for experimental results. At the stationary calibration setup, the resolution of the 100 $in.oz$ torque sensor approaches 1×10^{-3} Nm. However, the torque sensor's official document claims that the highest accuracy of the 100 $in.oz$ torque sensor under working environment is ±0.2%, corresponding to 1.4×10^{-3} Nm.

2.2 Fluids

This section examines the properties of the pure fluids without particles and the suspending fluids for liquid-solid flows in the present study.

Table 2.2 summarizes the properties of the fluids used in this investigation. All the densities and the dynamic viscosities listed in Table 2.2 are under the environmental temperature of 20 °C (equivalently 68 °F), which is the same as the laboratory temperature.

For the pure fluid experiments, the study considers the water, 77% glycerol-water mixture, 50% glycerol-water mixture, 28% glycerol-water mixture to cover a gap Reynolds number regimes corresponding to the laminar, the transitional, and the turbulent flows, which are discussed in Chapter 3. For the neutrally-buoyant experiments, the study used the 18% glycerol-water mixture and the 51% glycerol-ethanol mixture as the low-viscosity and the high-viscosity fluids to extend the tested particle Reynolds number regime in Chapter 4. Water was used for non-neutrally buoyant experiments in Chapter 5.

Regarding the pure water and the water-glycerol mixtures, the densities were directly measured under the lab environment, and the dynamic viscosities were calculated using the models from Cheng (2008). The density and the dynamic viscosity for pure water are 998 kg/m^3 and 1.00×10^{-3} Ns/m^2. With an decreasing glycerol percentage, the densities for the 77%, 50%, 28%, and 18% glycerol-water mixtures are 1210 kg/m^3, 1142 kg/m^3, 1080 kg/m^3, and 1050 kg/m^3, respectively, and the corresponding dynamic viscosities are 6.72×10^{-2} Ns/m^2, 8.36×10^{-3} Ns/m^2, 2.75×10^{-3} Ns/m^2, and 1.84×10^{-3} Ns/m^2.

For the glycerol-ethanol mixture, different combinations of glycerol and ethanol were tested based on the study of Ernst et al. (1936) to match the particle density of 1050 kg/m^3. The density of the 51% glycerol-ethanol was measured to be 1050 kg/m^3 under 20 °C. Then the dynamic viscosity of the 51% glycerol-ethanol mixture was measured by an inner-rotating rheometer and a falling ball viscometer, and the value is 2.90×10^{-2} Ns/m^2 as shown in Table 2.2. Before the measurement, the container of the glycerol-ethanol sample was placed in an ice bath until the liquid temperature reached 20 °C.

Fluid	Density	Dynamic viscosity
Water	998 kg/m^3	1.00×10^{-3} Ns/m^2
77% Glycerol 23% Water	1210 kg/m^3	6.72×10^{-2} Ns/m^2
50% Glycerol 50% Water	1142 kg/m^3	8.36×10^{-3} Ns/m^2
28% Glycerol 72% Water	1080 kg/m^3	2.75×10^{-3} Ns/m^2
18% Glycerol 82% Water	1050 kg/m^3	1.84×10^{-3} Ns/m^2
51% Glycerol 49% Ethanol	1050 kg/m^3	2.90×10^{-2} Ns/m^2

Table 2.2: Fluids properties under 20 °C

Particle property	Polystyrene 1	Polystyrene 2	SAN
Diameter (d)	3.34 mm	1.27 mm	3.22 mm
Particle density (ρ_p)	1050 kg/m^3	1050 kg/m^3	1050 kg/m^3
Gap width/diameter (b/d)	7.46	19.61	7.73
Shape	elliptical cylinders	spheres	ellipsoids
Sphericity (ψ)	0.7571	0.9998	0.9798

Table 2.3: Experimental particles properties

The percentages of the liquid mixtures described in this thesis are by volumes of the fluid composition. However, the study of Ernst et al. (1936) used weight percentage to describe the liquid mixture.

2.3 Particle properties

The present experimental study is conducted using three types of particles: polystyrene elliptical cylinders (polystyrene 1), polystyrene spheres (polystyrene 2), and nearly-spherical Styrene Acrylonitrile (SAN). Due to the elliptical shape, the polystyrene 1 particles are only used to create the rough surface on the rheometer wall, but not used in the liquid-solid flow in the current experiments. The experiments use polystyrene 2 particles and SAN particles as solid phases immersed in various liquids for rheological measurements. Table 2.3 summarizes the properties and the corresponding dimensions of the three types of particles in the current experiment.

Elliptical polystyrene

Figure 2.6 presents the 3.34 *mm* polystyrene particles, which are used to rough the rheometer walls. These hard plastic particles have an average minor cross-sectional axis length of 2.08 *mm* and an average major cross-sectional axis length of 2.92

mm, with an average longitudinal length of 3.99 *mm* (Koos, 2009). The average equivalent spherical diameter for polystyrene 1 particle is 3.34 ± 0.02 *mm*.

The elliptical polystyrene particles are filtered using sieves before the experiments to ensure the consistency of particle size. Both the annulus surfaces of the outer and inner cylinders are then roughened with polystyrene 1 particles.

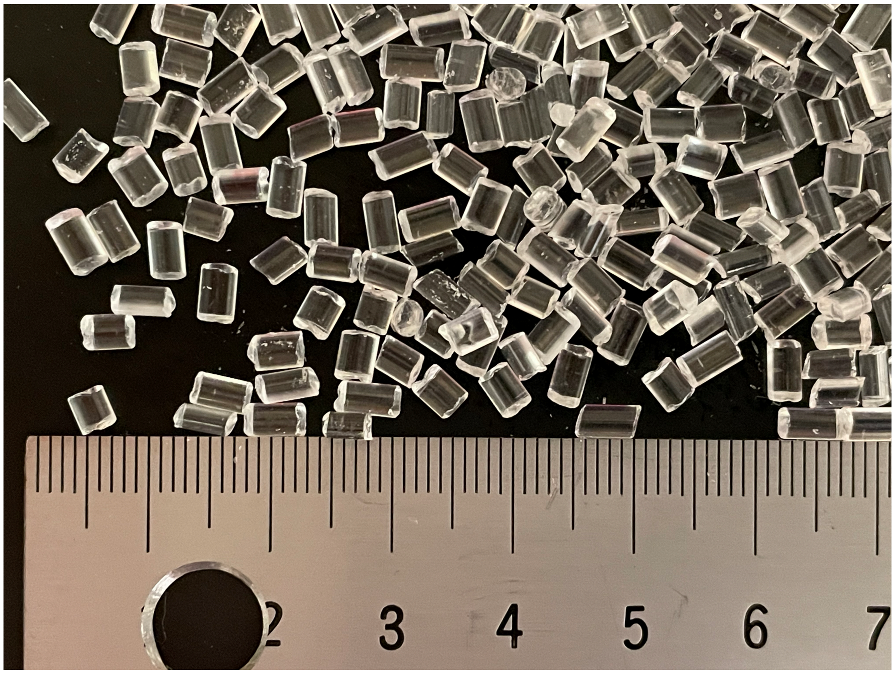

Figure 2.6: Polystyrene particles type 1. The particle diameter is 3.34 ± 0.02 *mm* and the particle density is 1050 kg/m^3. The unit of the ruler is *mm*.

Spherical polystyrene

Figure 2.7 presents the spherical polystyrene particles used in the rheological measurements. The spherical polystyrene is hard particles, which are usually used as blasting cleaning media. The polystyrene dust is removed. The polystyrene 2 particles have spherical shapes with a density of 1050 kg/m^3 and they are neutrally buoyant in a glycerol-water mixture of 18% glycerol and a glycerol-ethanol mixture of 51% glycerol under the lab environment of 20 °C.

The polystyrene 2 particles have an average diameter of 1.27 ± 0.01 *mm*. All the testing polystyrene particles are filtered with US standard sieves before the experimental measurements.

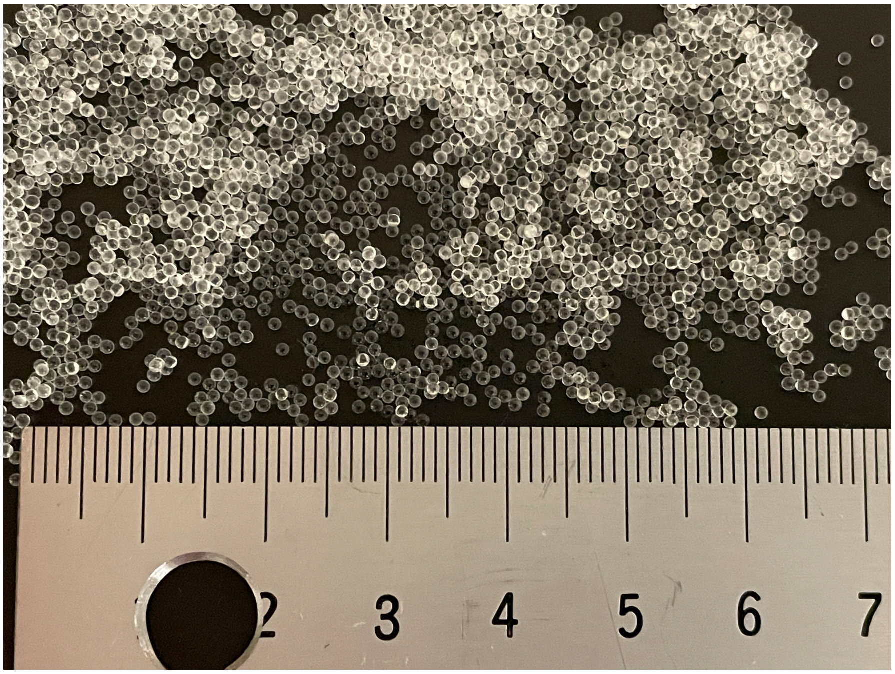

Figure 2.7: Polystyrene particles type 2. The particle diameter is 1.27 ± 0.01 mm and the particle density is 1050 kg/m^3. The unit of the ruler is mm.

SAN

The SAN particles in the liquid-solid mixture are presented in Figure 2.8. The shape of the SAN particle is nearly spherical, and the equivalent spherical diameter of 3.22 ± 0.02 mm. Typical SAN particles have particle densities ranging from 896-1200 kg/m^3 due to different manufacturing techniques. The SAN particles used in the current experiments have a density of 1050 kg/m^3 and they are neutrally buoyant in a glycerol-water mixture of 18% glycerol and a glycerol-ethanol mixture of 51% glycerol at the lab temperature of 20 °C.

Due to the relatively large particle size ($3.22mm$) and the associated manufacturing defect rate, a small amount of the SAN particles may contain bubbles leading to the variation of the SAN particle density. Therefore, all the SAN particles are floated in the liquid with a density of 1050 kg/m^3 to examine the relative density of the particles. The SAN particles that are not neutrally buoyant in the 1050 kg/m^3 liquid are filtered out before the experiment to ensure the consistency of SAN particle density during the torque measurements.

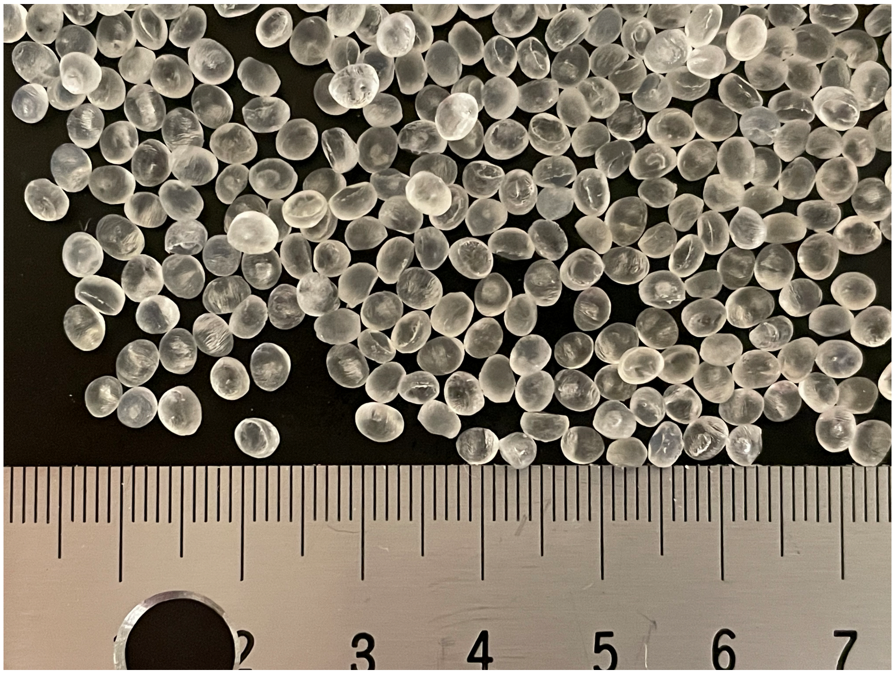

Figure 2.8: SAN particles. The particle diameter is 3.22 ± 0.02 mm and the particle density is 1050 kg/m^3. The unit of the ruler is mm.

Chapter 3

RHEOLOGICAL MEASUREMENTS WITH PURE FLUID

Pure fluid torque measurements are implemented in the Caltech Couette-flow device using the data acquisition system with torque sensors and the rough surface walls glued by the polystyrene particles. The torque measurement uses water, glycerol-water and glycerol-ethanol mixtures without any particles. The pure fluid experiments serve two purposes: validate the accuracy and the reliability of the torque measurement system; expand the rheological torque measurements to previously untested gap Reynolds number regions for pure fluids. This section reviews some fundamental properties in rheological experiments. Following that, it presents the current and previous pure fluid torque measurements, as well as the theoretical pure fluid results considering smooth walls.

The gap Reynolds number for the pure fluid experiments is defined as:

$$Re_b = \frac{\rho \omega r_o b}{\mu}. \tag{3.1}$$

Then the direct torque measurement is normalized by M_{lam}, which is the theoretical laminar torque for Couette flows with smooth walls. The laminar flow theory considers an infinitely-long cylindrical rheometer with the stationary inner cylinder and the rotational outer cylinder. The torque generated by the laminar flow in the rheometer annulus (smooth cylinder walls) is defined as (Schlichting, 1951):

$$M_{laminar} = 4\pi\mu H \frac{\omega r_i^2 r_o^2}{r_o^2 - r_i^2} = 2\pi\mu H r_i^2 \dot{\gamma}. \tag{3.2}$$

For each data point in the experiment, the corresponding temperature and the density of the fluid are measured and then considered when determining fluid properties.

3.1 Torque measurement of pure fluids

Measurements are taken with rough walls in the rheometer for five different kinds of fluids without particles: 28%, 50%, 77% glycerol-water mixtures, 51% glycerol-ethanol mixture and pure water. The Reynolds number corresponding to these four fluids covers from the laminar region to the turbulent region. This section also compares the present and previous pure fluid results using the Caltech Couette flow device.

Figure 3.1 presents the direct torque measurement with respect to $\dot{\gamma}$ for the 28% glycerol-water mixture and the water. The data point is the average value of several individual experimental measurements. The error bar represents the standard deviation of the torque values among the measurements. The theoretical torque results considering a laminar flow with smooth walls are also plotted in the figure. For both water and the 28% glycerol-water mixture examined, the direct torque measurements are substantially greater than the theoretical laminar torques (M_{lam}) considering smooth surface walls. The difference can be explained by the roughness of the walls and the turbulence, which is discussed in detail in Figure 3.3. Both sets of the measured torque show quadratic characteristics in terms of the slope.

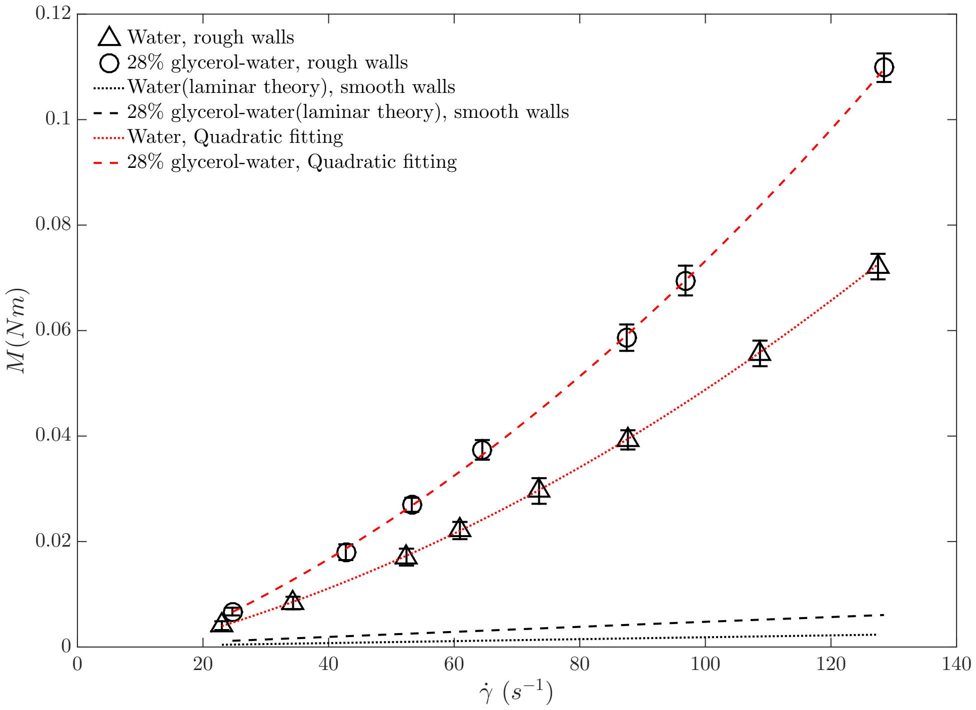

Figure 3.1: Direct torque measurement with respect to $\dot{\gamma}$ for water and 28% glycerol-water mixture without particles. The black dotted and dashed lines are the theoretical laminar torques considering smooth walls for water and 28% glycerol-water mixture, respectively. The quadratic fitting curves are $M = 2.7 \times 10^{-6}\dot{\gamma}^2 + 2.5 \times 10^{-4}\dot{\gamma} - 3.2 \times 10^{-3}$ and $M = 3.8 \times 10^{-6}\dot{\gamma}^2 + 4.1 \times 10^{-4}\dot{\gamma} - 5.8 \times 10^{-3}$ for water and 28% glycerol-water mixture, respectively.

Figure 3.2 shows the direct torque measurement with respect to $\dot{\gamma}$ for 50% and 77% glycerol-water mixtures, as well as the 51% glycerol-ethanol mixture and the laminar solutions. For the 77% glycerol-water mixture, the direct torque measurement

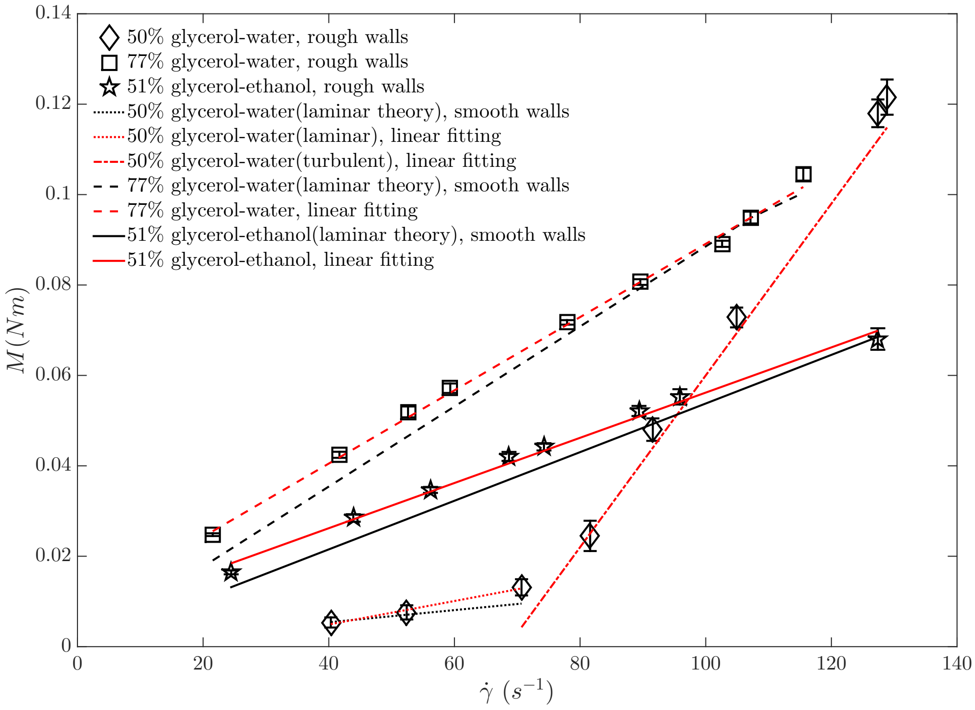

Figure 3.2: Direct torque measurement with respect to $\dot{\gamma}$ for 50% glycerol-water mixture, 77% glycerol-water mixture, and 51% glycerol-ethanol mixture without particles. The black dotted line and the red dotted line correspond to the 50% glycerol-water laminar solution and the 50% glycerol-water laminar linear fitting curve ($M = 2.6 \times 10^{-4}\dot{\gamma} - 5.5 \times 10^{-3}$). The red dash-dotted line is the 50% glycerol-water turbulent linear fitting curve ($M = 1.9 \times 10^{-3}\dot{\gamma} - 0.13$). The black solid and dashed lines are the 51% glycerol-ethanol and the 77% glycerol-water laminar solutions, respectively. The red solid and dashed lines are the linear fitting curves of the 51% GE and the 77% GW mixtures, which are4 $M = 5 \times 10^{-4}\dot{\gamma} + 6.2 \times 10^{-3}$ and $M = 8.1 \times 10^{-4}\dot{\gamma} + 8.1 \times 10^{-3}$.

matches closely in magnitude to the theoretical laminar results considering smooth walls. The measured torques of the 51% glycerol-ethanol mixture are slightly higher than the theoretical results, with a maximum deviation of 13.8% from the laminar solution for the shear rate around 70 s^{-1}. For the 50% glycerol-water mixture, the measurement is best fitted with two linear curves with different slopes over different shear rate regions. For shear rate slower than 80 s^{-1}, the three data points show good agreement with the theoretical results in the laminar regime. Once the shear rate further increases, the flow starts to transit to the turbulent regime, and the measured torque deviates significantly from the laminar results.

For the direct torque measurement results of the pure fluids considered in Figure 3.1 and Figure 3.2, the M_o values at $\dot{\gamma} = 0$ are -3.2×10^{-3} Nm, -5.8×10^{-3} Nm, 6.2×10^{-3} Nm, -5.5×10^{-3} Nm, and 8.1×10^{-3} Nm for water, 28%, 77%, 50% glycerol-water mixtures, and 51% glycerol-ethanol mixture, respectively. In comparison to the 1.4×10^{-3} Nm resolution of the 100 $in.oz$ torque sensor shown in Chapter 2, the M_o values of the pure fluids are down to the levels that approach the measurement limits of the torque sensors. Therefore, the fitting curves of the pure fluids torque measurements are assumed to pass through the origin of the coordinate system, corresponding to $M_o = 0$.

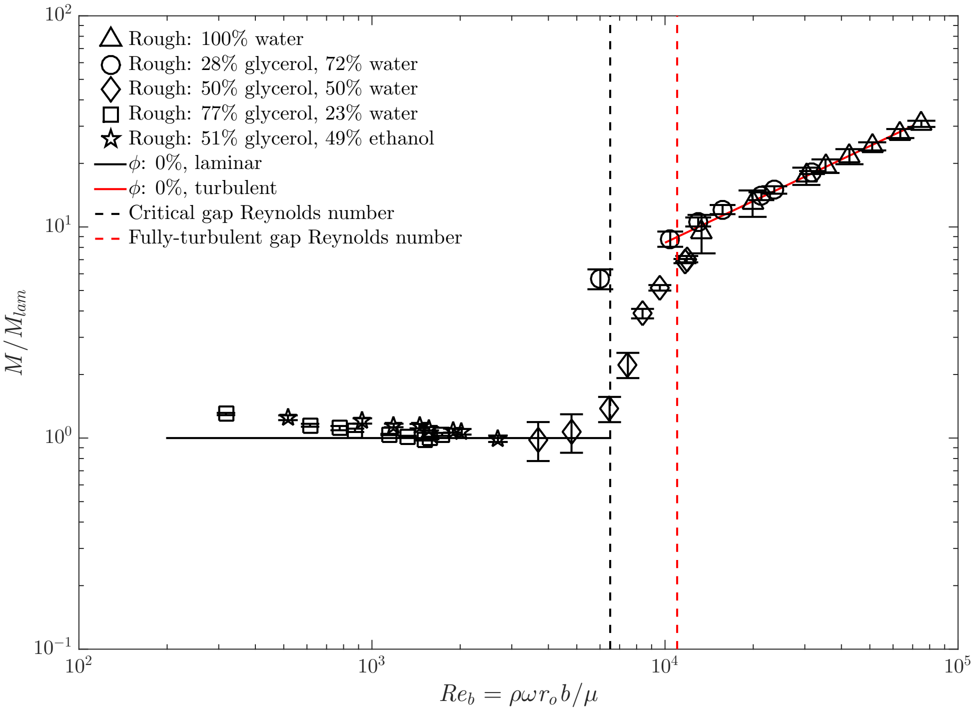

Figure 3.3: Normalized torque with respect to Re_b for glycerol-water mixtures of 28%, 50%, 77%, glycerol-ethanol mixture of 51%, and pure water without particles. The black solid line is the theoretical laminar solution considering smooth walls. The red solid line corresponds to the fitting curve ($M/M_{lam} = 0.0202{Re_b}^{0.655}$) for turbulent results. The black dashed line is the critical Re_b. The red dashed line represents the fully-turbulent Re_b.

Figure 3.3 shows M/M_{lam} (normalized torques) with respect to Re_b for the current results of pure fluids. The temperature and the density of the testing fluid were measured individually for each data point during the experiments and used to calculate the normalized torque. Based on the direct torque measurements for 50%

glycerol-water mixture shown in Figure 3.2, the transition to turbulence starts at the data point around 70 s^{-1}, where the 50% glycerol-water measurement starts to deviate from the laminar theory. Therefore, the critical Re_b at which the flow in the rheometer starts to become unstable is 6.5×10^3 considering rough walls. Based on the work of Taylor (1936a), Taylor (1936b), and Coles (1965), the Re_b at which the pure fluids become fully turbulent for the Caltech Couette flow device with rough walls is 1.1×10^4. The Reynolds number range of the 77% glycerol-water mixture is from 3.18×10^2 to 1.74×10^3. The measurements of 51% glycerol-ethanol mixture cover a gap Reynolds number regime from 5.17×10^2 to 2.69×10^3. Therefore, both the 77% glycerol-water and the 51% glycerol-ethanol experiments are in the laminar regime. The 28% glycerol-water and water experiments have Reynolds number ranges of $6.02 \times 10^3 - 3.17 \times 10^4$ and $1.33 \times 10^4 - 7.49 \times 10^4$, respectively, and most of the data points are beyond the critical Re_b. The 50% glycerol-water experiment has a Reynolds number range of $3.69 \times 10^3 - 1.19 \times 10^4$, which fills the Reynolds number gap corresponding to the laminar-turbulent transition.

In the case of 77% glycerol-water and 51% glycerol-ethanol mixtures, the normalized torques are close to 1, showing a good agreement with the laminar theory. The normalized torques of the 77% glycerol-water and 51% glycerol-ethanol mixtures are close to the measurement resolution of the Caltech Couette flow device. The uncertainty in the small value measurements may have contributed to the gradually decreasing behaviors of the normalized torques for both 77% glycerol-water and 51% glycerol-ethanol mixtures. The normalized torque of 50% glycerol-water mixture shows a transition around $Re_b = 6.5 \times 10^3$, with the maximum uncertainty occurring near the smallest Re_b. The normalized torque starts to increase gradually, and deviates from the laminar behavior around $Re_b = 3.7 \times 10^3$. At this stage, the turbulence has started to develop at the top and bottom corners of the outer-rotating rheometer, but has not affected the direct torque measurements significantly, which are implemented at the middle testing section of the rheometer (Figure 2.1). At the Re_b of 6.5×10^3, the torque ratio shows a sharp increase until the flow reaches a fully-turbulent state of Re_b at 1.1×10^4. This sudden change in magnitude corresponds to the propagation of the turbulence from annulus corners to the middle measurement section, and this laminar-torque transition contributes substantially to the torque measurement. This sudden increase of normalized torque is similar to the observation of Atta (1966), in which Atta described it as the catastrophic transition. For the normalized results of pure water and 28% glycerol-water mixture beyond the critical Re_b, the two data sets align well. The normalized torque for

28% glycerol-water mixture is approximately 18 times greater than the theoretical laminar torques at the highest shear rate. The M/M_{lam} for water is 31 times greater than the theoretical laminar results at the highest shear rate. However, there is one outlier data point of 28% glycerol-water mixture around $Re_b = 6.02 \times 10^3$, with a magnitude significantly higher than the 50% glycerol-water result. This suggests that once the 28% glycerol-water mixture enters the turbulent regime, the flow cannot transit back to the laminar region by reducing the shear rate. On the other hand, if we start the experiments for the 28% glycerol-water mixture at the lowest Re_b around 6.02×10^3, the 28% glycerol-water mixture is already in the turbulent regime, resulting in a higher normalized torque value. The fully turbulent measurements are best fitted as $M/M_{lam} = 0.0202 {Re_b}^{0.655}$, with the Re_b coefficient of the fully turbulent flow being 0.655. The comparison between the Re_b coefficients for pure fluids and liquid-solid flows is discussed in detail in Chapter 4.

Figure 3.4 compares the current results and the previous experimental results of Linares (2015) using the same rheometer with rough walls. Unlike previous pure-fluid experiments that only test the same fluids used in the neutrally-buoyant suspension studies, the present pure fluids are selected to extend the rheological measurements to the previously untested regime of laminar-turbulent transition.

For the comparison of 77% glycerol-water results, the values show favorable agreement, with the highest deviation in the magnitude of 42.3% at the lowest Reynolds number. In the transition region, the minimum and the maximum values of 50% glycerol-water results match well with the corresponding torque values from 77% and 28% glycerol-water mixtures, respectively. The normalized torque for the higher range of gap Reynolds number (water and 28% glycerol-water mixture) compares well with the previous result of water. However, a deviation in the normalized torque of 21% glycerol-water mixture (Linares, 2015) occurs at higher Reynolds numbers. Even for the comparison within Linares results, the normalized torque of water is considerably higher than that of 21% glycerol-water mixture, while these two data sets of normalized torque are assumed to align well over the same region of Reynolds number. This discrepancy can be explained by the different experimental methodologies to measure the torque employed by the previous and the present studies. Instead of using torque sensors, Linares, 2015 performed torque measurements by analyzing the elongation of springs with different stiffness connected to the inner rotating cylinder, and the springs were used as consumables. For example, in the original torque data of Linares, 2015 using two different springs (different stiffness)

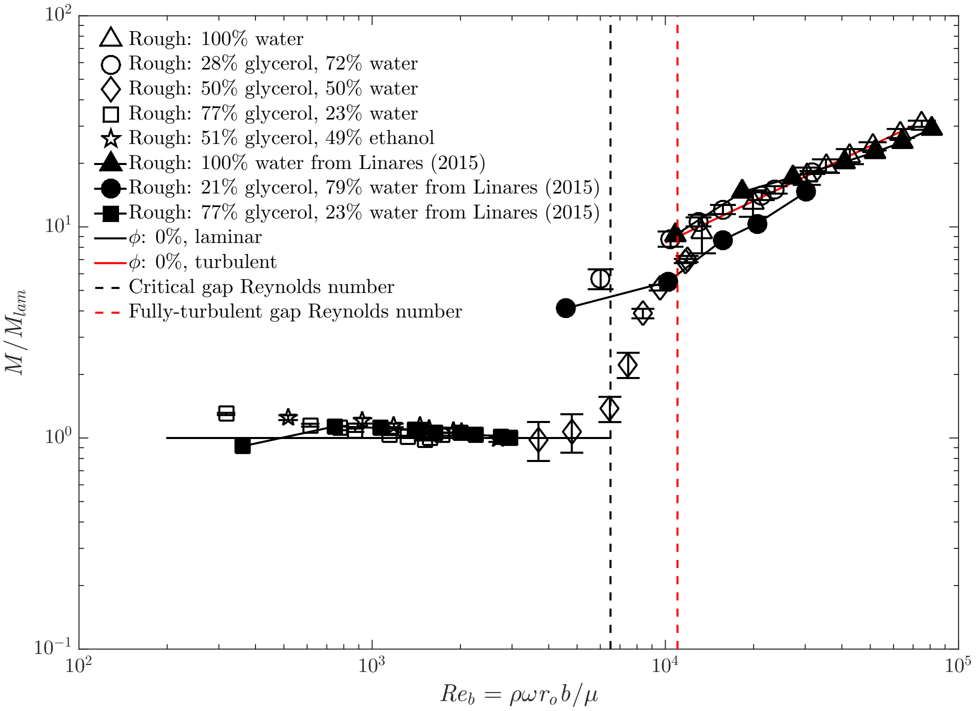

Figure 3.4: Direct torque measurement normalized by M_{lam}, with respect to Re_b for different fluids with no particles. The black solid data points are the results from Linares (2015).

for the same experiments over the same Reynolds number region, there was a difference in the measured torque. Therefore, the small measurement uncertainties introduced by the mechanical properties of different springs, though their magnitudes were limited in the original torque data, were inevitably amplified through the torque normalization, especially for the measurements in the high Re_b regions. However, for the present study, similar torque sensors from the same manufacturer are used in the experiments repeatedly. Section 2.1 already shows that the torque sensors have consistent calibration curves over the experimental torque range with good resolutions. As a result, the reaction torque sensors, combined with the new data acquisition system, have ensured the repeatability of the torque measurements.

The pure fluids results extend the rheological measurements to the previously untested Reynolds number regime for the Caltech Couette flow device. The results also verify the accuracy and reliability of the reaction torque sensor and the new data acquisition system.

Chapter 4

RHEOLOGICAL MEASUREMENTS OF NEUTRALLY-BUOYANT SUSPENSIONS

4.1 Motivation

To determine the effective viscosity of liquid-solid flows considering previously-untested intermediate Reynolds number regime, experiments with neutrally-buoyant particles were implemented. With the roughened walls, spherical particles with different sizes were sheared to investigate the effects of solid fractions, particle sizes, and particle collisions on the torque measurement and the transitional Reynolds numbers.

At Caltech, Koos et al. (2012) had made rheological measurements of particulate flows at high Reynolds numbers with different particles and various solid fractions. This study showed evidence of particle slip on the smooth walls of the rheometer. Following that, Linares et al. (2017) used rough walls to study the liquid-solid suspension considering the elliptical polystyrene particles.

With an upgraded experimental apparatus, further rheological experiments have been done using neutrally buoyant particles dispersed in low-viscosity and high-viscosity fluids separately to expand the Reynolds number regime tested. There are two types of particles used in the neutrally buoyant suspension experiments: the 3.22 *mm* SAN particles and the 1.27 *mm* polystyrene particles. To match the density of the immersed particles, there are two types of liquids considered: a glycerol-water (GW) mixture of 18% glycerol and 82% water (liquid mixture with low-viscosity) or a glycerol-ethanol mixture of 51% glycerol and 49% ethanol (liquid mixture with high-viscosity). Under the neutrally-buoyant state, the particles are evenly distributed in the rheometer annulus along the axial direction. The experimental results cover particle solid fractions, ϕ, from 10% to 50%, with Re from 0.51 to 773. Only these solid fractions are tested since the particles have almost filled the entire rheometer annulus at the 50% volume fraction.

Based on the studies of Buscall et al. (1993) and Barnes (1995), particle slip near the rheometer walls can be reduced with roughened walls. The roughened wall is also expected to enhance the interactions between the particles and the walls. For these reasons, all the neutrally buoyant rheological measurements performed in this study use particle-roughened walls.

This chapter summarizes the experimental results of neutrally-buoyant particles using rough walls for Re from 0.51 to 773. The torque measurements of small polystyrene particles and large SAN particles immersed in liquids with high and low viscosities are described in Section 4.2 and Section 4.3 separately, following the order of increasing particle Reynolds number. Section 4.4, Section 4.5, and Section 4.6 compare the SAN and polystyrene experimental results in detail to determine the effect of particle size, solids fraction, and Re on the effective viscosity of suspensions.

Most importantly, we propose a particle Reynolds number Re' ($Re' = \rho_f d U_{wall}/\mu$) based on the maximum shear flow velocity and the particle diameter instead of Re ($Re = \rho_f \dot{\gamma} d^2/\mu$) to examine the effective viscosity of the liquid-solid flows in Section 4.5. Section 4.6 further compares the neutrally-buoyant measurements as functions of $Re_b{}'$ and G'. Finally, Section 4.7 and Section 4.8 compare the present experimental measurements with the previous numerical results and the simulation results over the similar particle Reynolds number regime as functions of Re and Re'.

4.2 Rheological experiments of neutrally-buoyant particles in high-viscosity liquid

This section covers experimental results using neutrally-buoyant polystyrene and SAN particles immersed in high-viscosity fluids. The small polystyrene particle and the large SAN particle results are presented in separate subsections, with particle Reynolds number (Re) ranging from 0.51 to 8.5, and from 4.97 to 48, respectively. The SAN particles are nearly spherical and have an effective diameter of 3.22 mm, about 2.5 times the size of the spherical polystyrene particles. The dynamic viscosity for the 51% glycerol-ethanol mixture is 0.029 Ns/m^2 under the lab temperature of 20 °C. All the experimental results presented in this section use polystyrene and SAN particles with annulus width to particle diameter ratios of 19.61 and 7.73, respectively. The results of direct torque measurements and the results of normalized effective viscosity are presented and discussed in detail in each subsection.

Polystyrene particles in high-viscosity liquid

Figure 4.1 shows the results of direct torque measurements of the 1.27 mm polystyrene particles in the high-viscosity fluid mixture of glycerol and ethanol. The torque data points and the error bars reflect the methodologies discussed in Chapter 2. The 10%

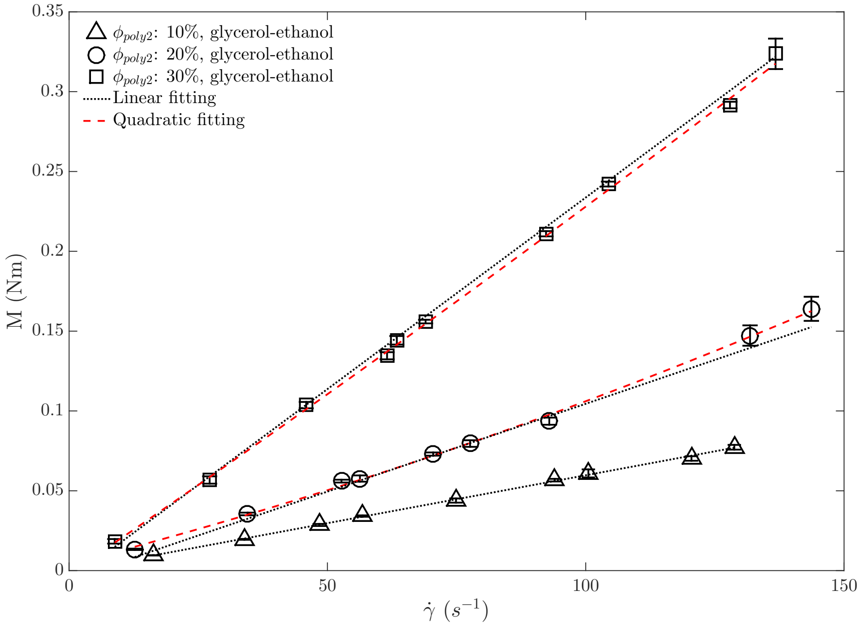

Figure 4.1: Direct torque measurement in terms of $\dot{\gamma}$ for ϕ = 0.1, 0.2, and 0.3 considering small polystyrene particles in fluid mixture with high viscosity. The linear fitting curves are $M = 6\times10^{-4}\dot{\gamma}-2.8\times10^{-4}$, $M = 1.1\times10^{-3}\dot{\gamma}-5.5\times10^{-3}$, and $M = 2.4\times10^{-3}\dot{\gamma} - 6.3\times10^{-3}$ for 10%, 20%, and 30% solid fractions, respectively. The quadratic fitting curves are $M = 1.9\times10^{-6}\dot{\gamma}^2 + 8.3\times10^{-4}\dot{\gamma} + 4.1\times10^{-3}$ and $M = 1\times10^{-6}\dot{\gamma}^2 + 2.2\times10^{-3}\dot{\gamma} - 2\times10^{-3}$ for 20% and 30% solid fractions, respectively. $\rho_p/\rho_f = 1$.

solid fraction results are best fitted with a linear fitting curve, indicating that the effective viscosity is independent of $\dot{\gamma}$ over the regime examined. While for the 20% and 30% solid fraction results, the data sets are fitted with both linear and quadratic fitting curves. The two data sets match well with the linear fitting curves at low and intermediate shear rates. However, the results deviate from the linear fitting curves at shear rates of approximately 143 s^{-1}, and are best fitted with the quadratic fitting curves. All three linear fitting curves almost pass through the origin of the coordinate system. This indicates a minimum yield stress on the middle testing cylinder. M_o is the torque value at the intercept between the torque fitting curve and the y axis, and can be also understood as the torque value at $\dot{\gamma} = 0$. For the 10%, 20%, and 30% solid fractions, the M_o values for the linear fitting curves are -2.8×10^{-4} Nm, -5.5×10^{-3} Nm, and -6.3×10^{-3} Nm, which are approaching the resolution of 1.4×10^{-3} Nm for the 100 $in.oz$ torque sensor. Therefore, the linear fitting curves are assumed to pass through the origin and the linear fitting curves are

$M = 6 \times 10^{-4}\dot{\gamma}$, $M = 1.1 \times 10^{-3}\dot{\gamma}$, and $M = 2.4 \times 10^{-3}\dot{\gamma}$ for 10%, 20%, and 30% solid fractions, respectively.

Figure 4.2 shows the original torque measurements using small polystyrene particles in the fluid mixture of glycerol and ethanol for 40% and 50% solid fractions, respectively. The 40% solid fraction data set are fitted with both linear and quadratic fitting curves. As the shear rate gradually increases, the torque increases slowly at low shear rates, but starts to deviate from the linear fitting curve around 60 s^{-1}. The 50% solid fraction data fits well with the linear curve. At the 40% and 50% solid fraction states, the torque at 0 shear rate (M_o) are estimated to be 0.032 Nm (quadratic) and 0.35 Nm, corresponding to yield stresses of 1.72 N/m^2 and 18.87 N/m^2.

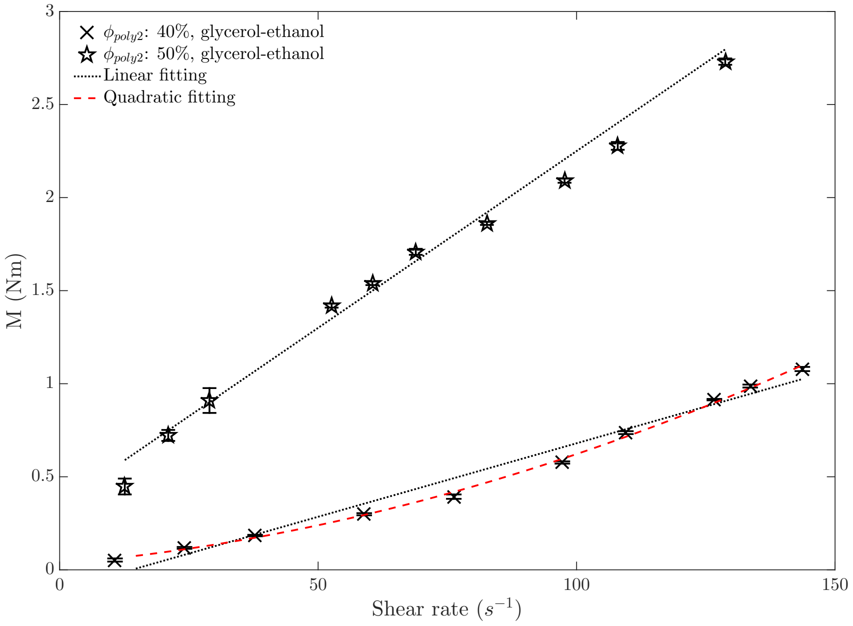

Figure 4.2: Direct torque measurement in terms of $\dot{\gamma}$ for $\phi = 0.4$ and 0.5 considering small polystyrene particles in fluid mixture with high viscosity. The linear fitting curves are $M = 7.9 \times 10^{-3}\dot{\gamma} - 0.11$ and $M = 1.9 \times 10^{-2}\dot{\gamma} + 0.35$ for 40% and 50% solid fractions, respectively. The quadratic fitting curve is $M = 3.5 \times 10^{-5}\dot{\gamma}^2 + 2.4 \times 10^{-3}\dot{\gamma} + 0.032$ for 40% solid fraction. $\rho_p/\rho_f = 1$.

All the direct torque measurements were then normalized by the theoretical laminar torque predicted using the glycerol-ethanol mixture viscosity considering smooth walls. The processed normalized torque as a function of Re_b is shown in Figure 4.3 along with the suspending fluid results and the critical Re_b considering pure fluids.

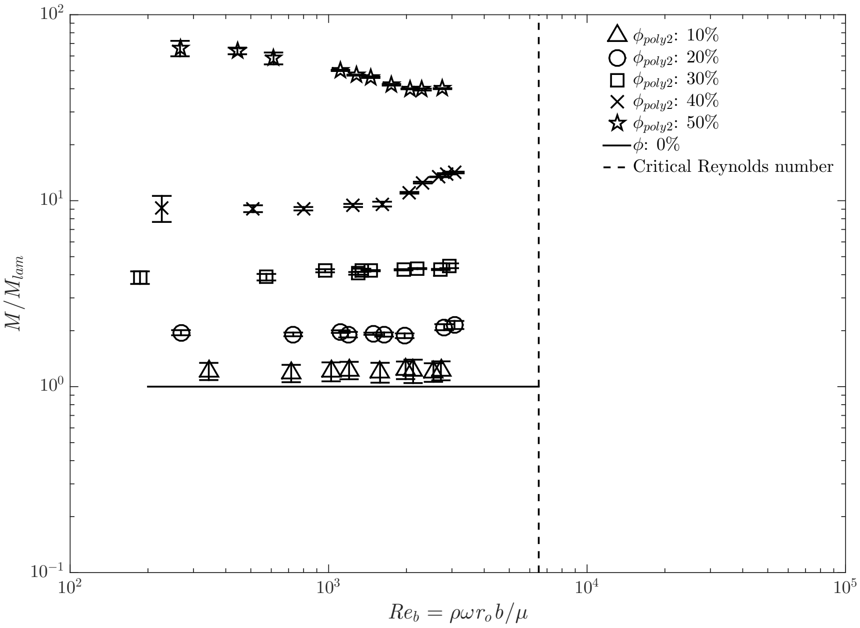

Figure 4.3: Direct torque measurement normalized by the laminar torque in terms of gap Reynolds number. The experiment considers 1.27 *mm* polystyrene particles in the fluid mixture of glycerol and ethanol. $\rho_p/\rho_f = 1$.

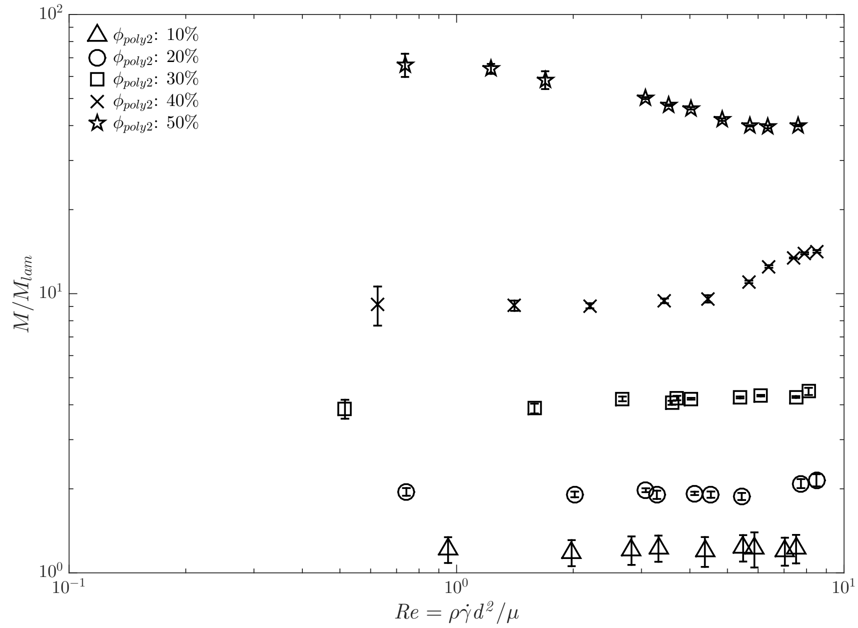

Figure 4.4: Direct torque measurements normalized by the laminar torque in terms of particle Reynolds number considering 1.27 *mm* polystyrene particles in the fluid mixture of glycerol and ethanol (high-viscosity fluid). $\rho_p/\rho_f = 1$.

Figure 4.4 shows the same data but presented in terms of the particle Reynolds number rather than the gap Reynolds number. Using the gap Reynolds number, all of these measurements are below the critical Re_b for the laminar-turbulent transition found for pure fluids. The normalized torque presented in Figure 4.3 and in Figure 4.4 is equivalent to the effective viscosity (μ'/μ) as shown in the following equation if $M_o = 0$:

$$\frac{M}{M_{lam}} = \frac{\mu'}{\mu}. \tag{4.1}$$

As discussed in the experimental procedures of Section 2.1, to account for the uncertainty in the temperature measurements considering small polystyrene particles immersed in the fluid mixture of glycerol and ethanol, the normalized torques of the 10% solid fraction measurements shown in Figure 4.3 and Figure 4.4 are the average values of the maximum and the minimum error bars.

In examining the results as a function of Re, the normalized torque of the 10% solid fraction results shows little variation over the Reynolds number regime tested. At the 20% and the 30% solid fraction states, the normalized torques are relatively constant until approximately $Re = 5$. Near the particle Reynolds number around 8.5, due to an increase from inertial effects, both the 20% and 30% solid fraction results show slight shear-thickening behaviors, which are consistent with the observations of cubic fitting curves in Figure 4.1. For the 40% solid fraction result, the normalized torque shows little change for Re from 0.62 to 3.44, but starts to increase from Reynolds number of approximately 4.45. This magnitude change in the 40% solid fraction may be caused by the increasing inertial effects and the particle packing structure change as the shear rate increases. The 50% result appears to gradually decrease as Re increases. The shear-thinning behaviors are caused by the large M_o at $\dot{\gamma} = 0$ and the limited particle migration space in the annulus.

SAN particle in high-viscosity liquid

Experiments with SAN particles were conducted using a glycerol-ethanol fluid of 51% glycerol and 49% ethanol by volume.

Figure 4.5 presents the direct torque measurements in terms of $\dot{\gamma}$ for SAN particles in glycerol-ethanol solutions considering lower solid fractions (ϕ = 10%, 20% and 30%). Both linear (dotted lines) and quadratic (dashed lines) fitting curves are plotted for three solid fractions. For the 10% and the 20% solid fractions, the linear

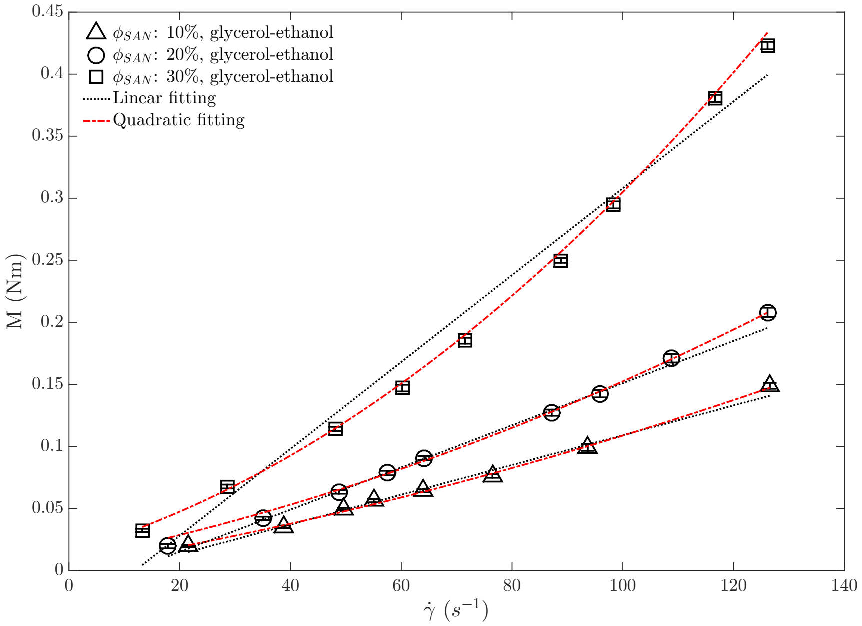

Figure 4.5: Direct torque measurement in terms of $\dot{\gamma}$ for ϕ = 0.1, 0.2, and 0.3 considering large SAN particles in fluid mixture with high viscosity. $\rho_p/\rho_f = 1$. The linear fitting curves are $M = 1.2\times10^{-3}\dot{\gamma} - 1.1\times10^{-2}$, $M = 1.7\times10^{-3}\dot{\gamma} - 1.9\times10^{-2}$, and $M = 3.5\times10^{-3}\dot{\gamma} - 4.2\times10^{-2}$ for 10%, 20%, and 30% solid fractions, respectively. The quadratic fitting curves are $M = 3.1\times10^{-6}\dot{\gamma}^2 + 7.5\times10^{-4}\dot{\gamma} + 2.7\times10^{-3}$, $M = 5.4\times10^{-6}\dot{\gamma}^2 + 9\times10^{-4}\dot{\gamma} + 8.4\times10^{-3}$, $M = 1.6\times10^{-5}\dot{\gamma}^2 + 1.3\times10^{-3}\dot{\gamma} + 1.5\times10^{-2}$ and for 10%, 20%, and 30% solid fractions, respectively.

fittings compare well with the data sets, indicating a relatively constant effective viscosity of the particulate flow. The 10% and the 20% results are not strictly linear, and can also be fitted with quadratic curves. Around the maximum shear rate of 127 s^{-1}, the torque data points of 10% and 20% solid fractions also show increasing dependence on the shear rate. The 30% solid fraction result is better fitted with the quadratic curve, showing an increasing effective viscosity. For the 10%, 20%, and 30% quadratic fitting curves, the M_o values are 2.7×10^{-3} Nm, 8.4×10^{-3} Nm, and 1.5×10^{-2} Nm, which are down to the levels of the resolution for the 100 $in.oz$ torque sensor. Therefore, M_o values are assumed to be 0 and the quadratic fitting curves are $M = 3.1\times10^{-6}\dot{\gamma}^2 + 7.5\times10^{-4}\dot{\gamma}$, $M = 5.4\times10^{-6}\dot{\gamma}^2 + 9\times10^{-4}\dot{\gamma}$, $M = 1.6\times10^{-5}\dot{\gamma}^2 + 1.3\times10^{-3}\dot{\gamma}$ for 10%, 20%, and 30% solid fractions, respectively.

Higher solid fractions (ϕ = 40% and 50%) of SAN particles immersed in 51% glycerol-ethanol mixture are tested as seen in Figure 4.6. The 40% solid fraction result matches closely with the linear fitting and quadratic fitting. While for the

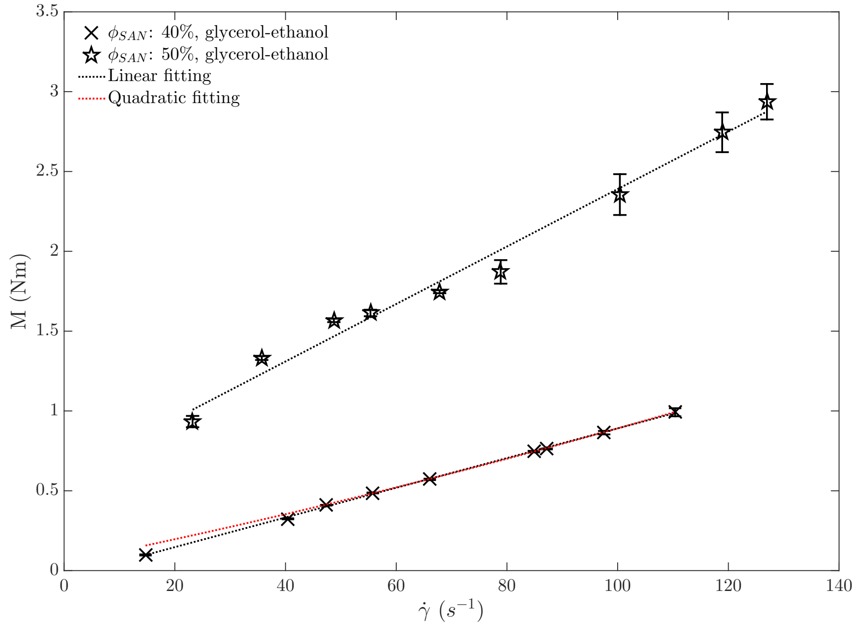

Figure 4.6: Direct torque measurement in terms of $\dot{\gamma}$ for $\phi = 0.4$ and 0.5 considering large SAN particles in fluid mixture with high viscosity. The linear fitting curves are $M = 9.3 \times 10^{-3}\dot{\gamma} - 3.9 \times 10^{-2}$ and $M = 1.8 \times 10^{-2}\dot{\gamma} + 0.59$ for ϕ of 0.4 and 0.5. The quadratic fitting curve is $M = 1.4 \times 10^{-5}\dot{\gamma}^2 + 7 \times 10^{-3}\dot{\gamma} + 0.051$ for 40% solid fraction. $\rho_p/\rho_f = 1$.

50% solid fraction data, the data points are best fitted with a linear curve, with a positive intercept with the y-axis. At the 40% and 50% solid fraction states, M_o are approximately 0.051 Nm (quadratic) and 0.59 Nm, corresponding to yield stresses of 2.75 N/m^2 and 31.81 N/m^2.

Figure 4.7 presents the normalized torque in terms of Re_b along with the critical gap Reynolds number considering pure fluids. Figure 4.8 presents the same results of normalized torque (M/M_{lam}), but the results are presented with respect to Re ranging from 4.97 to 48. Using the gap Reynolds number, the current liquid-solid flow measurements are still below the critical gap Reynolds number considering pure fluids. For ϕ = 10%, 20%, and 30%, the normalized torques increase with Re. For the result of 40% solid fraction, the effective viscosity increases with the particle Reynolds number over the Re regime of 5.52 to 20.9, then reaches a relatively constant value. Similar to what was found for polystyrene particles, the 50% solid fraction results decrease at lower Reynolds numbers, and then show little variation with the Reynolds number around $Re = 48.2$.

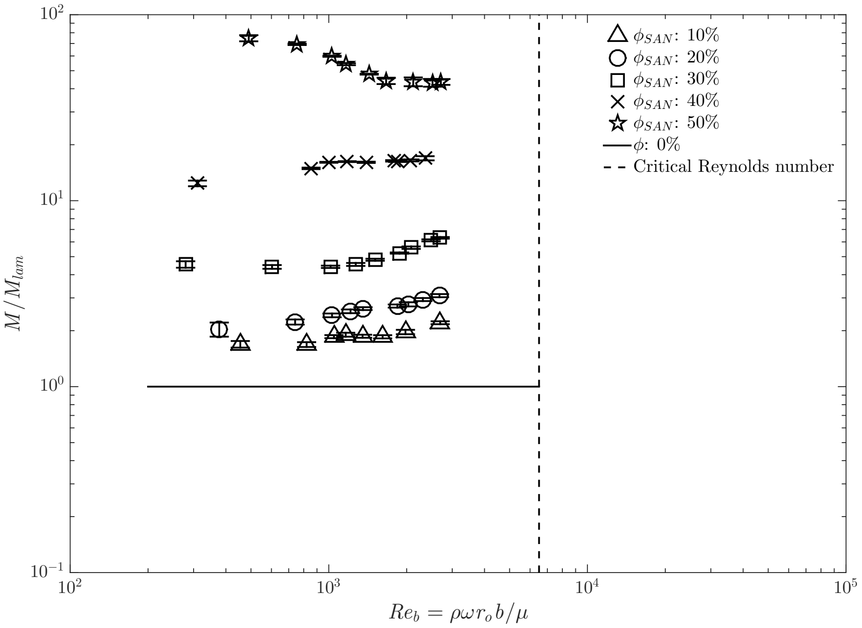

Figure 4.7: Direct torque measurement normalized by the laminar torque in terms of gap Reynolds number. The experiment considers 3.22 *mm* SAN particles immersed in the fluid mixture of glycerol and ethanol (high viscosity). $\rho_p/\rho_f = 1$.

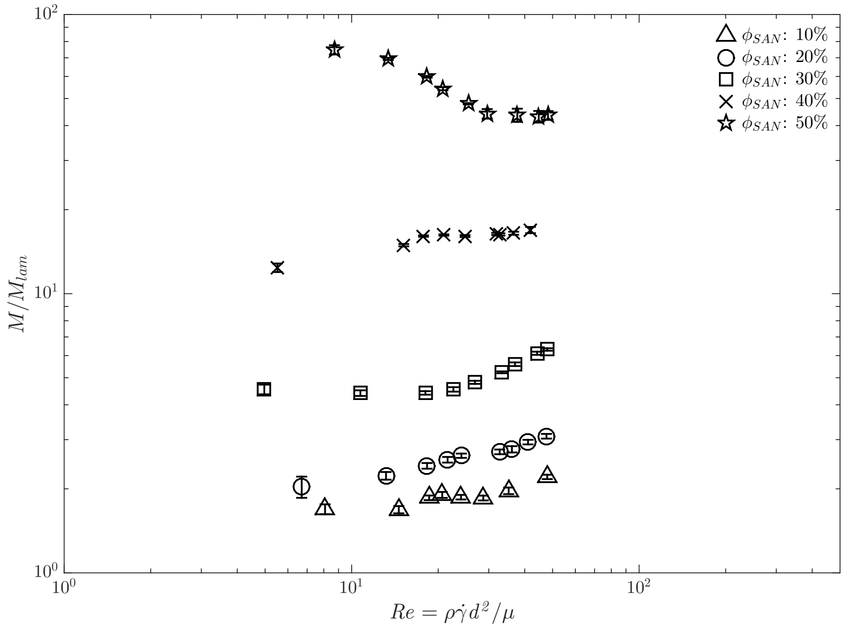

Figure 4.8: Direct torque measurements normalized by the laminar torque in terms of particle Reynolds number considering large SAN particles in the fluid mixture of glycerol and ethanol (high viscosity). $\rho_p/\rho_f = 1$.

4.3 Rheological experiments of neutrally-buoyant particles in low-viscosity liquid

This section covers experimental results using neutrally-buoyant polystyrene and SAN particles immersed in low-viscosity liquids. The experiments using small polystyrene particles cover a particle Reynolds number (Re) regime from 13.2 to 135, while the results considering large SAN particles have a Reynolds number region from 120 to 773. All the experiments use the same suspending fluids of 18% glycerol and 82% water. Under the lab temperature of 20 °C, the dynamic viscosity for 18% glycerol and 82% water mixture is 0.0018 Ns/m^2.

For the experimental results presented in this section, the rough walls (elliptical polystyrene particles glued on the surface walls) of the rheometer are the same ones used for the experiment considering high-viscosity fluids. The results of direct torque measurements and the normalized torques are presented in the following sections.

Polystyrene particles in low-viscosity liquid

Figure 4.9 shows the direct torque measurements for solid fractions of 10%, 20%, and 30% of 1.27 mm polystyrene particles (poly2) immersed in 18% glycerol and 82% water mixture (low-viscosity fluid).

For solid fractions of 10% and 20%, each data set is fitted with two linear curves with different slopes based on the shear rates. The torque increases linearly at low shear rates from approximately 16 s^{-1} to 65 s^{-1}, showing good agreements with the dotted linear fitting curves. Similar to the transitional shear rate of 70 s^{-1} found in Figure 3.2, once the shear rate further increases around 70 s^{-1} in Figure 4.9, the particulate flow starts to transit to the turbulent flow. As a result, the torques start to deviate from the laminar results, and increase linearly along the dashed fitting curves with higher slopes.

At the solid fraction of 30%, the direct torque measurement increases linearly with $\dot{\gamma}$ initially. At a shear rate of approximately 45 s^{-1}, the torque starts to increase in a nonlinear way with the shear rate, which is best fitted with a cubic fitting curve (dash-dotted line). It is assumed that the presence of more polystyrene particles has augmented the magnitude of the turbulence and caused the measured torque to increase at a faster rate. The M_o values for the 10%, 20%, and 30% solid fractions at low shear rates are -4.1×10^{-3} Nm, -1.7×10^{-3} Nm, and -1.8×10^{-3} Nm, which are very close to the torque sensor resolution of 1.4×10^{-3} Nm. The M_o values are

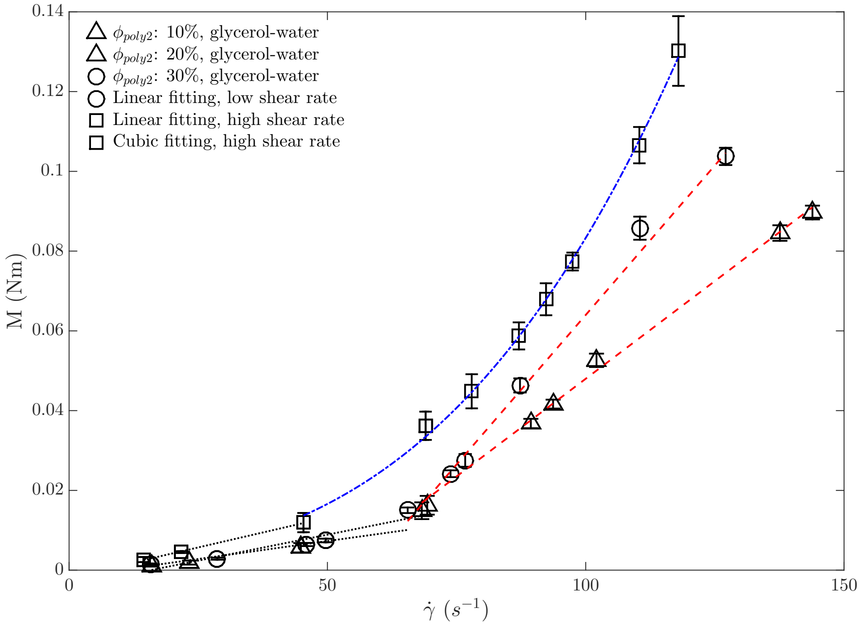

Figure 4.9: Direct torque measurement in terms of $\dot{\gamma}$ for $\phi = 0.1$, 0.2, and 0.3 considering small polystyrene particles in the fluid mixture with low viscosity. $\rho_p/\rho_f = 1$. Dotted lines and dashed lines are the linear curve fitting for the low $\dot{\gamma}$ and high $\dot{\gamma}$ experimental data. Dash-dotted line is the cubic fitting for the high-shear-rate data of the 30% polystyrene experiment. At low shear rates, the linear fitting curves are $M = 2.6 \times 10^{-4}\dot{\gamma} - 4.1 \times 10^{-3}$, $M = 1.8 \times 10^{-4}\dot{\gamma} - 1.7 \times 10^{-3}$, and $M = 3 \times 10^{-4}\dot{\gamma} - 1.8 \times 10^{-3}$ for 10%, 20%, and 30% solid fractions, respectively. At high shear rates, the linear fitting curves are $M = 9.8 \times 10^{-4}\dot{\gamma} - 0.05$ and $M = 1.5 \times 10^{-3}\dot{\gamma} - 8.6 \times 10^{-2}$ for 10% and 20% solid fractions, respectively. The cubic fitting curve for the 30% solid fraction is $M = 6.4 \times 10^{-8}\dot{\gamma}^3 + 4.3 \times 10^{-7}\dot{\gamma}^2 + 1.5 \times 10^{-4}\dot{\gamma} + 2.9 \times 10^{-5}$.

assumed to be 0, and the linear fitting curves at low shear rates are $M = 2.6 \times 10^{-4}\dot{\gamma}$, $M = 1.8 \times 10^{-4}\dot{\gamma}$, and $M = 3 \times 10^{-4}\dot{\gamma}$.

Figure 4.10 presents the direct torque measurements for solid fractions of 40% and 50% considering polystyrene particles in the fluid mixture of glycerol and water. Unlike the low solid fraction results, the torques are best modeled using linear and quadratic fitting curves. The 50% fitting curve has a positive intercept with the y-axis. For the 40% and 50% solid fraction measurements, M_o are approximately 9.3×10^{-4} Nm (cubic) and 0.11 Nm, and the corresponding yield stresses are 0.05 N/m^2 and 5.93 N/m^2.

Figure 4.11 presents the direct torque measurements normalized by the theoretical

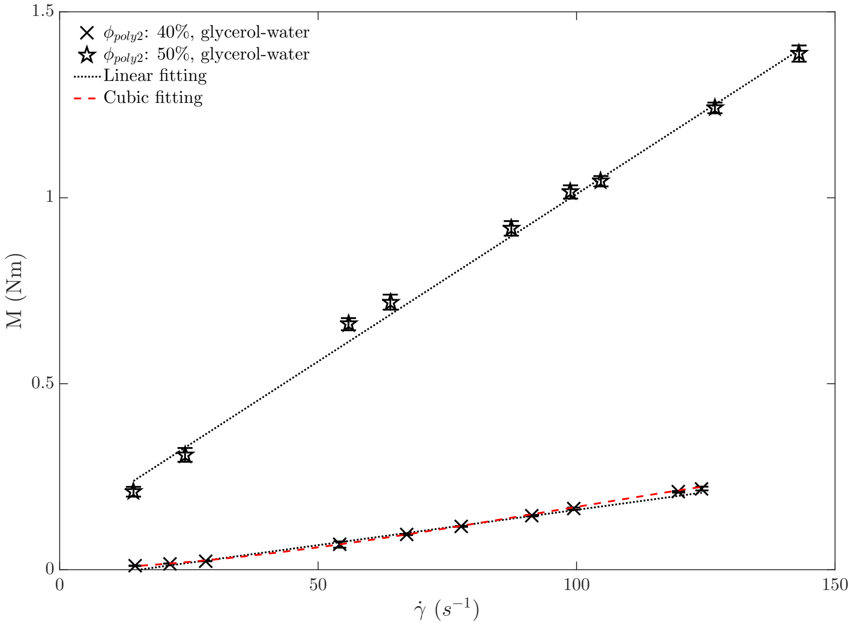

Figure 4.10: Direct torque measurement in terms of $\dot{\gamma}$ for ϕ = 0.4 and 0.5 considering small polystyrene particles in the fluid mixture with low viscosity. The linear fitting curves are $M = 1.9 \times 10^{-3}\dot{\gamma} - 0.029$ and $M = 9 \times 10^{-3}\dot{\gamma} + 0.11$ for ϕ of 0.4 and 0.5. The cubic fitting curve is $M = -7.4{\times}10^{-8}\dot{\gamma}^3{+}2.1{\times}10^{-5}\dot{\gamma}^2{+}3.2{\times}10^{-4}\dot{\gamma}{+}9.3{\times}10^{-4}$.

laminar torques predicted from laminar theory using the dynamic viscosity of the suspending fluid in terms of Re_b. The image also includes the normalized torque of the suspending glycerol-water mixture (red line) and the same pure fluids critical gap Reynolds number as shown in Figure 3.3. Using the gap Reynolds number, the results are near the transition to turbulence considering the critical Re_b found for pure fluids. Near the critical Reynolds number, the data for the 10% and 20% solid fractions lie below the data corresponding to a pure fluid suggesting the addition of small polystyrene particles delays the transition.

Figure 4.12 presents the same normalized torque results in terms of Re. For ϕ = 10%, 20%, and 30%, the normalized torques increase slightly until Re of approximately 40, and the increasing measurements are mainly driven by the inertial effects from the liquid-solid flow. Once the shear rates further increase, the results of the 10%, 20%, and 30% solid fractions show strong shear-thickening behaviors, which are caused by the laminar-turbulent transition and are discussed in Section 4.4. At higher shear rates, because the corresponding Stokes numbers are greater than 10, the collisions of the particles may also contribute to the measured torque. At the

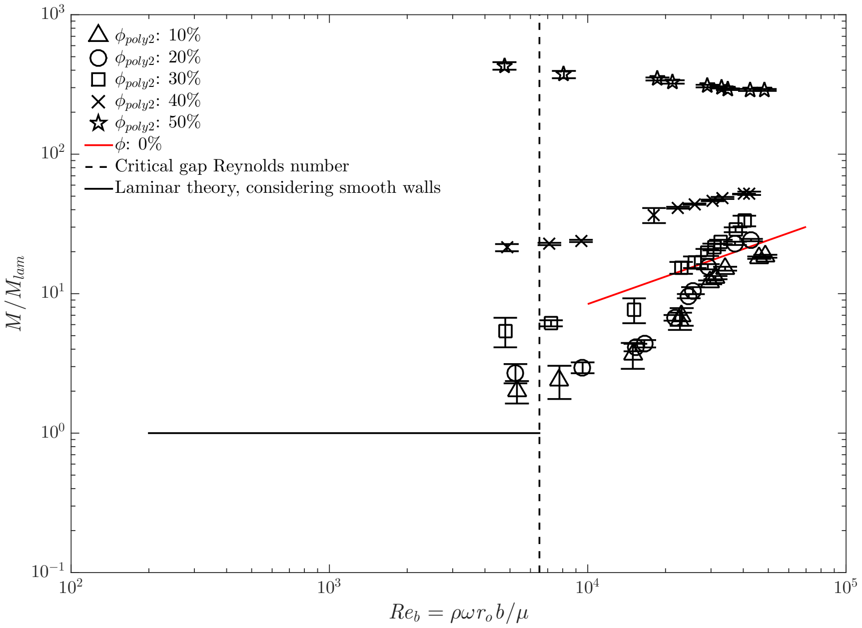

Figure 4.11: Direct torque measurement normalized by the laminar torque in terms of gap Reynolds number. The experiment considers 1.27 *mm* polystyrene particles in the fluid mixture of glycerol and water. $\rho_p/\rho_f = 1$.

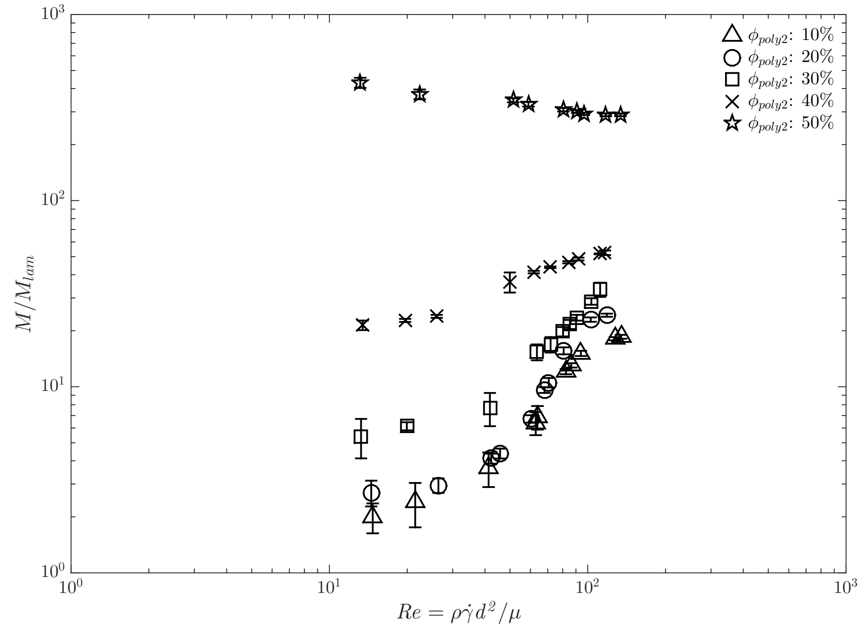

Figure 4.12: Direct torque measurement normalized by the laminar torque in terms of particle Reynolds number. The experiment considers 1.27 *mm* polystyrene particles in the fluid mixture of glycerol and water. $\rho_p/\rho_f = 1$.

solid fraction of 40%, the normalized torque increases slightly over the particle Reynolds number regime examined. For $\phi = 50\%$, the effective viscosity decreases slightly at lower particle Reynolds numbers, and appears to reach a steady state at Reynolds numbers above 91. At the 40% and 50% solid fraction states, the limited migration space of polystyrene particles has suppressed the magnitudes of the normalized torque.

SAN particles in low-viscosity liquid

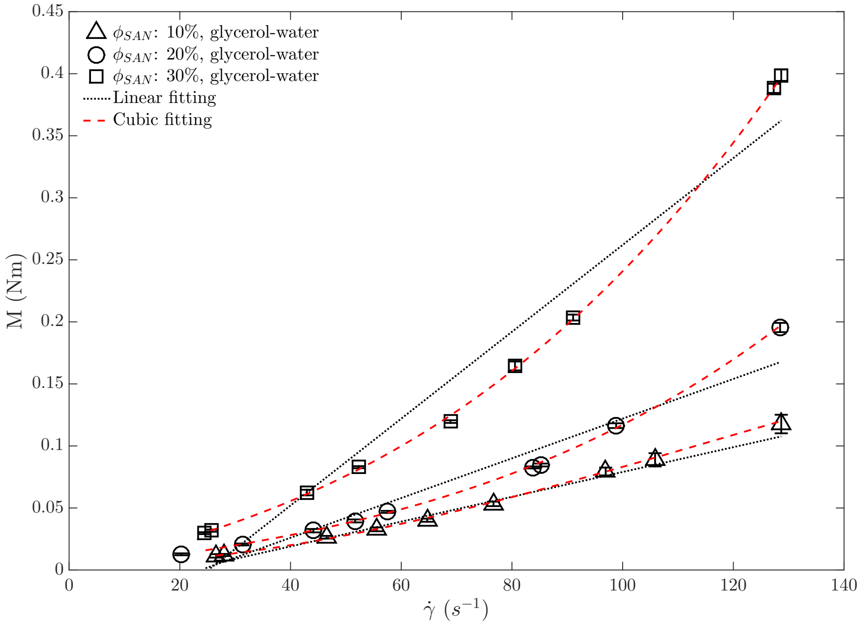

Figure 4.13: Direct torque measurement in terms of $\dot{\gamma}$ for $\phi = 0.1$, 0.2, and 0.3 considering large SAN particles in the fluid mixture with low viscosity. $\rho_p/\rho_f = 1$. The linear fitting curves are $M = 1\times10^{-3}\dot{\gamma} - 2.1\times10^{-2}$, $M = 1.6\times10^{-3}\dot{\gamma} - 3.8\times10^{-2}$, and $M = 3.5\times10^{-3}\dot{\gamma} - 8.8\times10^{-2}$ for 10%, 20%, and 30% solid fractions, respectively. The cubic fitting curves are $M = -3.1\times10^{-8}\dot{\gamma}^3 + 1.1\times10^{-5}\dot{\gamma}^2 - 4.7\times10^{-6}\dot{\gamma} + 4.6\times10^{-3}$, $M = 5.6\times10^{-8}\dot{\gamma}^3 - 1.5\times10^{-7}\dot{\gamma}^2 + 6.3\times10^{-4}\dot{\gamma} - 3.8\times10^{-4}$, $M = 7.3\times10^{-8}\dot{\gamma}^3 + 7.2\times10^{-6}\dot{\gamma}^2 + 9.4\times10^{-4}\dot{\gamma} + 1.8\times10^{-3}$ and for 10%, 20%, and 30% solid fractions, respectively. $\rho_p/\rho_f = 1$.

Figure 4.13 presents the direct torque measurements for $\phi = 10\%$, 20%, and 30% considering SAN particles immersed in the low-viscosity fluid mixture of glycerol and water.

In Figure 4.13, as the shear rate increases, the torque increases as expected. This plot also includes linear curve fit and cubic curve fit for each data set. At constant

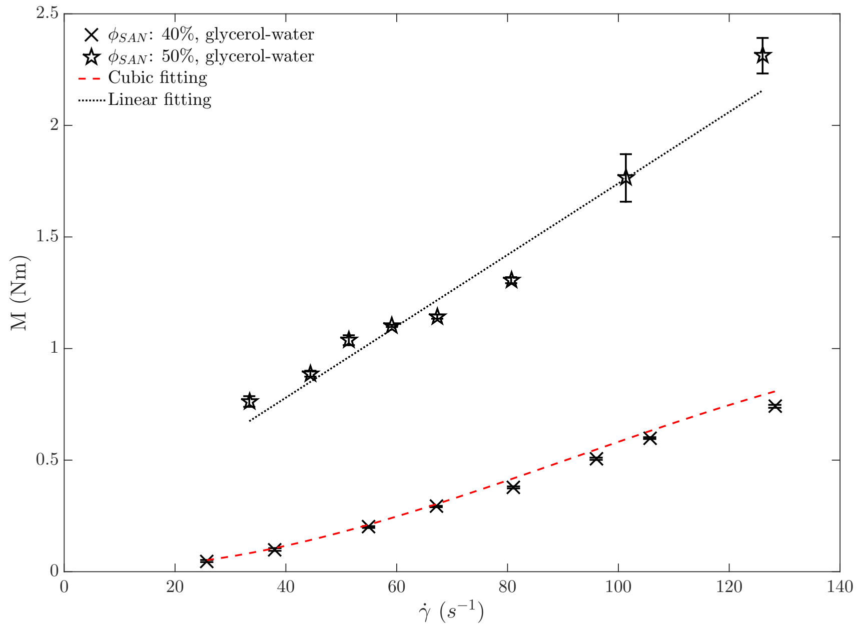

Figure 4.14: Direct torque measurement in terms of $\dot{\gamma}$ for $\phi = 0.4$ and 0.5 considering large SAN particles in the fluid mixture with low viscosity. The cubic fitting curve is $M = -4 \times 10^{-7}\dot{\gamma}^3 + 1.1 \times 10^{-4}\dot{\gamma}^2 - 1.4 \times 10^{-3}\dot{\gamma} + 0.022$. The linear fitting curve is $M = 1.6 \times 10^{-2}\dot{\gamma} + 0.14$.

temperature, a linear fitting relation between the shear rate and the torque indicates a Newtonian behavior of the liquid-solid flow. However, for these three data sets, the linear fit does not match the distribution of the data points very well, and the linear fitting curves have negative intercepts with the y-axis. As shown by the red dashed lines, the three data sets are fitted with cubic curves closely, indicating an increasing dependence of torque on the shear rate for ϕ = 10%, 20%, and 30% solid fractions. The M_o values for the 10%, 20%, and 30% solid fractions considering cubic fittings are 4.6×10^{-3} Nm, -3.8×10^{-4} Nm, and 1.8×10^{-3} Nm, which are approaching the torque sensor resolution of 1.4×10^{-3}. Therefore, the M_o values are assumed to be 0, and the cubic fitting curves are $M = -3.1 \times 10^{-8}\dot{\gamma}^3 + 1.1 \times 10^{-5}\dot{\gamma}^2 - 4.7 \times 10^{-6}\dot{\gamma}$, $M = 5.6 \times 10^{-8}\dot{\gamma}^3 - 1.5 \times 10^{-7}\dot{\gamma}^2 + 6.3 \times 10^{-4}\dot{\gamma}$, $M = 7.3 \times 10^{-8}\dot{\gamma}^3 + 7.2 \times 10^{-6}\dot{\gamma}^2 + 9.4 \times 10^{-4}\dot{\gamma}$.

Figure 4.14 presents the direct torque measurements for ϕ = 40% and 50% considering SAN particles immersed in a glycerol-water mixture. Unlike the lower solid fraction results presented in Figure 4.13, these two data sets are best fitted with cubic fitting curve and linear fitting curve separately. For the data sets of ϕ = 50%, the linear fitting has the positive intercept with the y-axis. M_o for the 40% and 50% solid

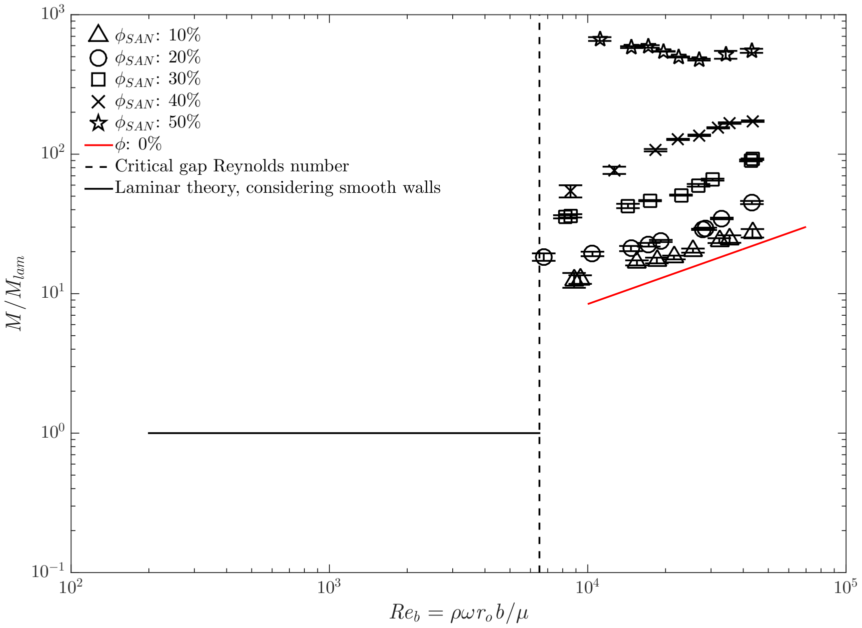

Figure 4.15: Direct torque measurement normalized by the laminar torque in terms of gap Reynolds number. The experiment considers 3.22 *mm* SAN particles in the fluid mixture of glycerol and water. $\rho_p/\rho_f = 1$.

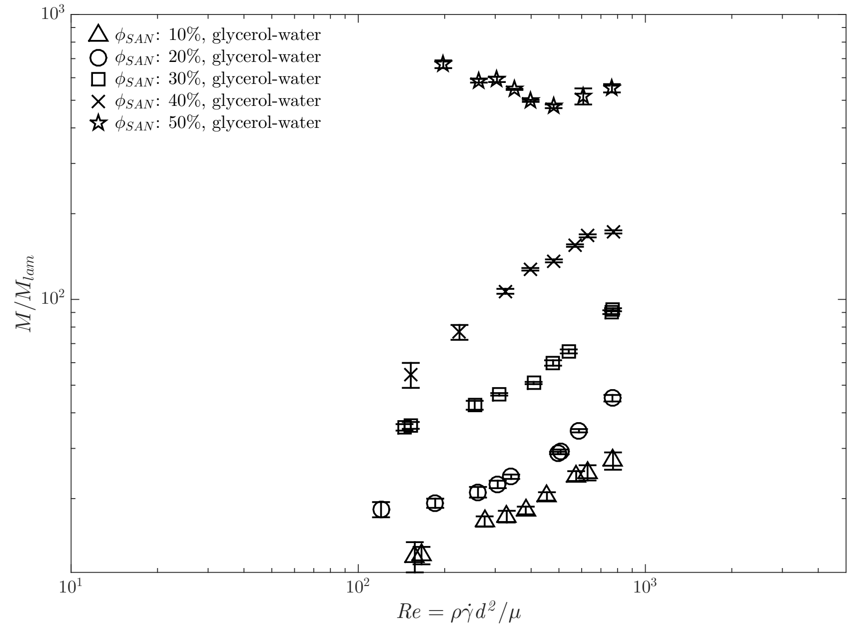

Figure 4.16: Direct torque measurement normalized by the laminar torque in terms of particle Reynolds number. The experiment considers 3.22 *mm* SAN particles in the fluid mixture of glycerol and water. $\rho_p/\rho_f = 1$.

fraction measurements are approximately 0.022 Nm and 0.14 Nm, corresponding to yield stresses of 1.18 N/m^2 and 7.55 N/m^2.

The torque measurements are then normalized by the laminar flow theory torque considering the dynamic viscosity of the suspending liquid, and the results are presented in terms of Re_b in Figure 4.15. The vertical dashed line represents the critical Re_b found for pure fluids. Using the gap Reynolds number, most of the experimental measurements are beyond the critical Reynolds number for laminar-turbulent transition found for pure fluids, and the measured torques are larger than the values found in the pure fluid results over the same Reynolds number regimes.

Figure 4.16 presents the same normalized torque but the results are presented in terms of Re. For ϕ from 10% to 40%, the normalized torque increases with particle Reynolds number. However, for ϕ = 50%, the normalized torque decreases slightly with Reynolds number, and eventually reaches a relatively constant value for Re of approximately 765.

4.4 Comparison between SAN and polystyrene results with respect to gap Reynolds numbers

To study the impact of the different particle sizes, along with the turbulent transition, solid fractions, particle collision, and velocity fluctuation on the torque measurement, the 20 neutrally-buoyant data sets using SAN and polystyrene particles in high-viscosity and low-viscosity fluids from the previous sessions are presented together and compared in detail in this section.

Starting from this section, to avoid data confusion, the same neutrally-buoyant data set with specified particle and suspending fluid is presented using the same color. The experimental results cover solid fractions, ϕ, from 10% to 50%, with the specified solid fraction presented using the same plot markers.

The normalized torque for the same particle type (SAN or polystyrene) immersed in the low- and high- viscosity fluids are presented as a function of Re_b to investigate the laminar-turbulent transition. After that, the results of the normalized torques considering two different particles are presented in terms of Re_b for laminar regions and near-turbulence regimes, respectively.

Laminar-turbulent transition

Figure 4.17 presents the polystyrene results (M/M_{lam}) as a function of Re_b immersed in glycerol-ethanol and glycerol-water mixtures, with ϕ = 10%, 20%, and 30%. For measurements using high-viscosity fluid, the measurements have smaller slopes than the pure fluid turbulent fitting curve ($M/M_{lam} = 0.0202 Re_b^{0.655}$), indicating the flows are still laminar. While for the measurements using low-viscosity fluids, in comparison with the pure fluids result and the corresponding pure fluid critical Reynolds number, the 1.27 *mm* polystyrene particles have delayed the transition to turbulence and suppressed the magnitude of the turbulence at the solid fractions of 10%, 20%, and 30%. This observation is similar to the neutrally-buoyant results from Matas et al. (2003), which are based on the pressure fluctuations of the liquid-solid flows. Their results show that the critical Reynolds number depends on the solid fraction and the ratio of the pipe diameter to the particle diameter (D/d). For small particles with $D/d \geq 65$, the laminar to turbulent transition shifted to larger critical Reynolds numbers for all solid fractions (maximum $\phi = 35\%$). The difference between the thresholds of b/d and D/d could be explained by the different wall roughness and the different flow types (Taylor-Couette flow vs. pipe flow).

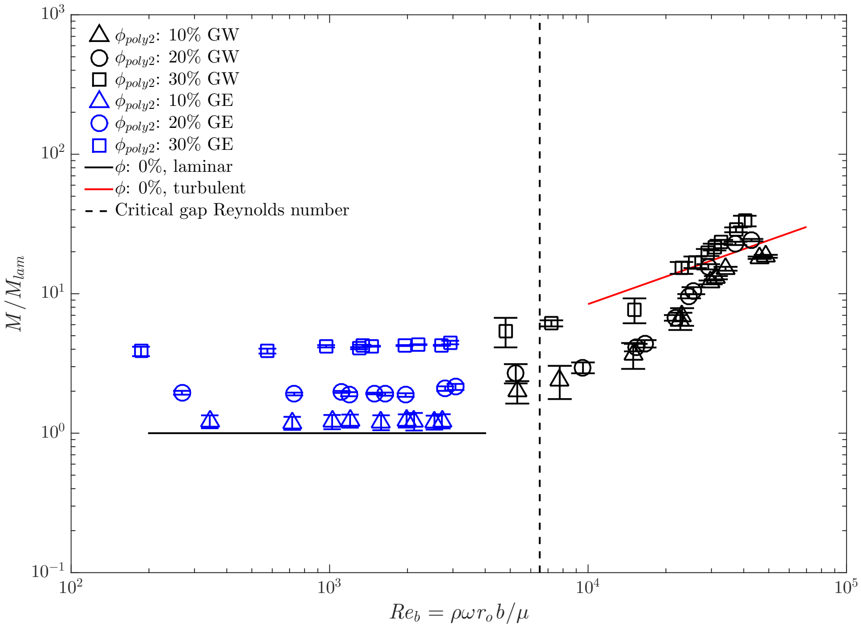

Figure 4.17: Direct torque measurement normalized by the laminar torque in terms of gap Reynolds number considering polystyrene particles in the glycerol-ethanol and glycerol-water mixtures, separately. The results include solid fractions of ϕ = 0.1, 0.2, and 0.3.

At the 10% and 20% solid fractions, the corresponding normalized torques of the liquid-solid mixtures are smaller than the normalized torque of the suspending

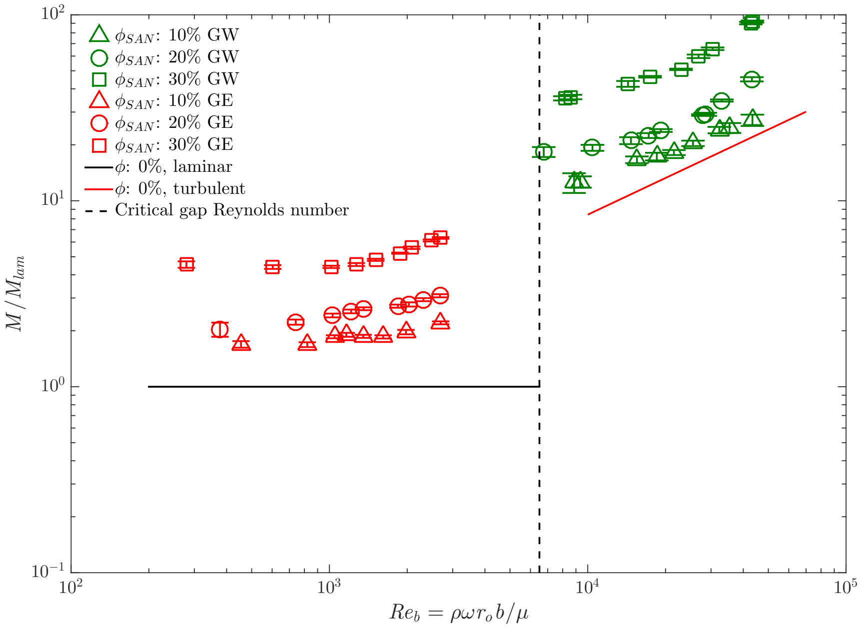

Figure 4.18: Direct torque measurement normalized by the laminar torque in terms of gap Reynolds number considering SAN particles in the glycerol-ethanol and glycerol-water mixtures, separately. The results include solid fractions of $\phi = 0.1$, 0.2, and 0.3.

fluid until Re_b of approximately 3×10^4. As the shear rates further increase, the normalized torques of the 10% and 20% solid fractions match up with the results of the pure fluids, and the liquid-solid flows share similar slopes as the pure fluid results ($M/M_{lam} \propto {Re_b}^{0.655}$), indicating the liquid-solid flows have reached the fully turbulent state.

Figure 4.18 shows the normalized torque measurements (M/M_{lam}) considering SAN particles in the low-viscosity and high-viscosity liquids separately for 10%, 20%, and 30% solid fractions. The results of the pure fluids and the pure fluids critical Reynolds number are plotted along with the liquid-solid flow measurements. For measurements using high-viscosity fluid, similar to what was found for the polystyrene measurements, the data has smaller slopes than the pure fluid turbulent fitting curve, and the measurements are still in the laminar region. But for the results using low-viscosity fluid, as compared to the results of pure fluids in Figure 3.3, for the 10%, 20%, and 30% solid fractions, the experimental measurements show that the relatively large 3.22 mm SAN particles augment the turbulent effects by causing the particulate flow to transition at lower gap Reynolds numbers and increasing the magnitudes of the measured torque. The slopes of the 10%, 20%, and 30% solid fraction measurements compare well with the turbulent fitting curve, indicating the particulate flows have become fully turbulent. Unfortunately, there is no overlap between the low- and high-viscosity fluid data sets in terms of gap Reynolds numbers, even though the rheometer is run at the maximum speed.

Measurements below transition to turbulence

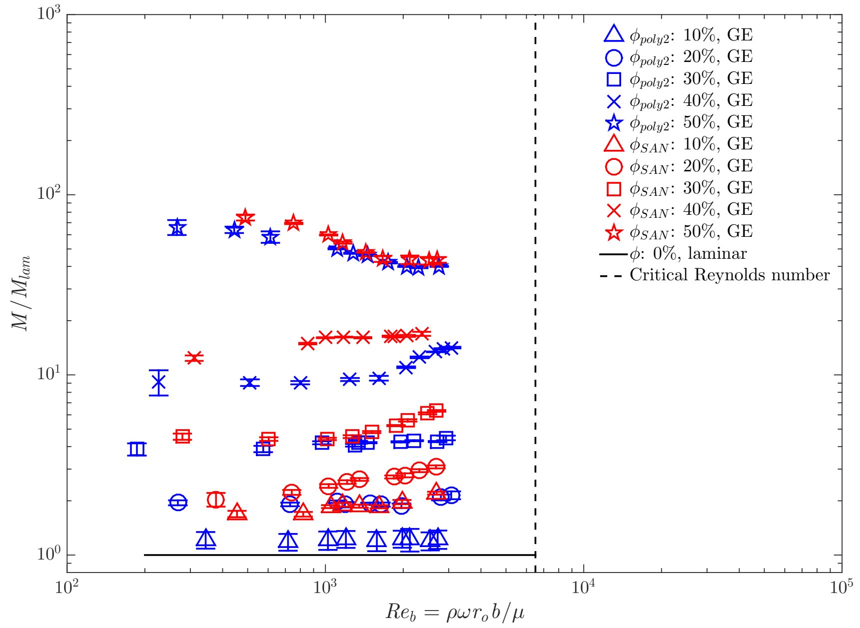

Figure 4.19: Direct torque measurements normalized by the laminar torque in terms of gap Reynolds number for comparison between the 1.27 *mm* polystyrene particles and 3.22 *mm* SAN particles in the fluid mixture of glycerol and ethanol considering $\phi = 0.1, 0.2, 0.3, 0.4$, and 0.5.

Figure 4.19 shows the normalized results considering both SAN and polystyrene particles immersed in high-viscosity fluids as a function of Re_b for solid fractions from 10% to 50%, along with the suspending pure fluid results. As shown in the contexts of Figure 4.3 and Figure 4.7, the examined gap Reynolds numbers for both measurements in the fluid mixture of glycerol and ethanol are below the critical gap Reynolds number considering pure fluids. For solid fractions of 10%, 20%, and 30%, polystyrene particle measurements presented in this image show little variation until Re_b around 2.2×10^3, and start to increase slightly for Re_b from 2.2×10^3 to 3×10^3. Over the approximately same Re_b regimes tested, all the SAN particle measurements show increased dependence on the particle Reynolds numbers, and the magnitudes of the effective viscosities are approximately 80%, 48%, and 47% greater than the polystyrene particles measurements at the highest gap Reynolds number for 10%, 20%, and 30% solid fractions, respectively. The differences are mainly caused by the inertial effects, which are examined in Section 4.5.

While both the 40% solid fraction results increase as Re_b increases, the 50% solid fraction results show shear-thinning behaviors. In terms of the magnitudes of the normalized torques, the 40% SAN particle result is approximately 35% larger than the polystyrene particle result for Re_b of approximately 2.3×10^3, but the 50% SAN particle result matches well with the corresponding polystyrene particle result near the highest Re_b of approximately 2.7×10^3. The differences in the measurements of 40% solid fraction can be explained by the different particle packing structures and the different b/d ratios (Fornari et al., 2016; Gallier et al., 2016). However, at the 50% solid fraction state in the high-viscosity fluids, the normalized torques are nearly independent of the particle Reynolds number.

Measurements near transition to turbulence

Figure 4.20 presents the torque normalized by the laminar torque considering the dynamic viscosity of the suspending glycerol-water mixture for both SAN and polystyrene particles (ϕ = 10%, 20%, 30%, 40% and 50%) immersed in low-viscosity fluids in terms of gap Reynolds number (Re_b). The pure fluid critical Reynolds number and the suspending fluid measurement are shown along with the results. At the 10%, 20%, and 30% solid fractions, while the 3.22 *mm* SAN particles have enhanced the turbulence as discussed for Figure 4.18, the 1.27 *mm* polystyrene particles are found to delay the transition to turbulence in Figure 4.17. Around the highest Re_b of approximately 4.2×10^4, the SAN normalized torques are 50%, 86%, and 176% larger than the corresponding polystyrene measurements for 10%, 20%, and 30% solid fractions, respectively. Besides the magnitude difference caused by the laminar-turbulent transition, the different particle sizes, the annulus gap to particle diameter ratios (b/d = 7.73 and 19.61), and the velocity fluctuations also contribute to the differences. With a Stokes number region from St = 2 to St = 85, particle collisions may also contribute to the torque measurements once St is greater than 10 (Yang and Hunt, 2006). Due to the larger particle size and the corresponding larger particle inertia, SAN particle (3.22 *mm*) collisions may contribute more to the torque measurements as compared to the collisions of polystyrene particles (1.27 *mm*).

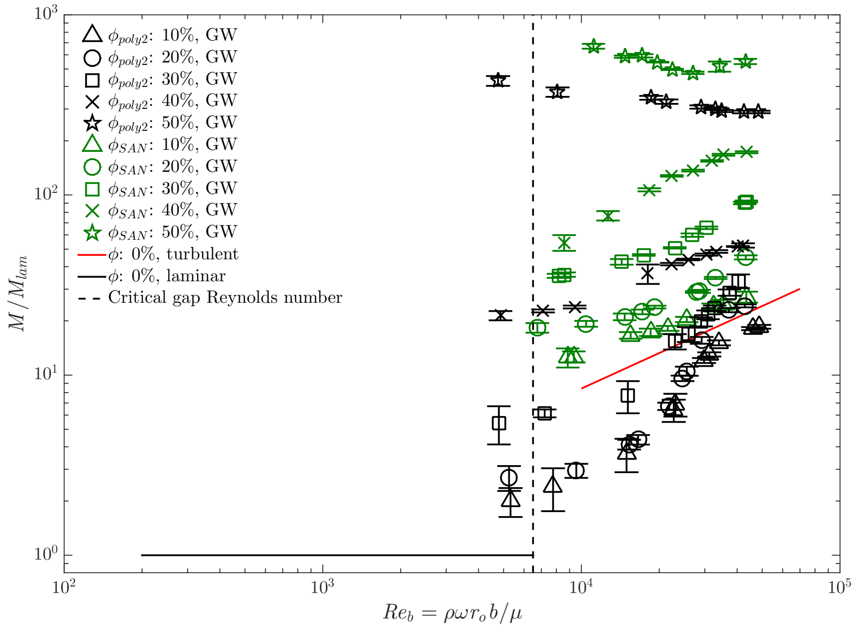

Figure 4.20: Direct torque measurements normalized by the laminar torque in terms of gap Reynolds number for comparison between the 1.27 *mm* polystyrene particles and 3.22 *mm* SAN particles in the fluid mixture of glycerol and water considering ϕ = 0.1, 0.2, 0.3, 0.4, and 0.5.

Both the 40% solid fraction results show shear thickening behaviors, with the SAN result being 229% greater than the corresponding polystyrene results near the maximum Re_b around 4.2×10^4. At the solid fraction of 50%, the measurement for SAN results decrease slightly for $Re_b < 2.70 \times 10^4$ followed by a subsequent shear-thickening behavior for Re_b ranging from 2.70×10^4 to 4.30×10^4. The 50% solid fraction polystyrene particle measurements show slight shear-thinning behavior over the examined region, and are approximately 48% smaller in comparison with the SAN particle measurements at the highest shear rate. Previous studies have shown changes in the microstructures of suspending particles in the high-solid-fraction flow (Kulkarni and Morris, 2008; Yeo and Maxey, 2013). This mismatch could be explained by the different layering structures of SAN and polystyrene particles, considering the small gap size of the rheometer.

4.5 Comparison between SAN and polystyrene results with respect to Re and Re'

In this section, each normalized torque data set for ϕ from 10% to 50% with specified particle and liquid is compared one by one following the order of increasing solid fractions. Unlike the widely-used particle Reynolds number ($Re = \rho_f \dot{\gamma} d^2/\mu$) based on d^2, a defined Reynolds number ($Re' = \rho_f d U_{wall}/\mu$) based on d is introduced. Immediately after each plot using Re, the results are compared with respect to the Reynolds number using the maximum shear flow velocity (U_{wall}) to examine the matching differences between Re and Re' in detail. The normalized torques (M/M_{lam}) for ϕ from 10% to 30% are compared with respect to Re and Re' following the order of increasing particle Reynolds numbers. Then the yield stresses of the 40% and 50% solid fractions are taken into account, and the 40% and 50% measurements are examined using $(M - M_o)/M_{lam}$ vs. Re and $(M - M_o)/M_{lam}$ vs. Re'.

Normalized torque as functions of Re and Re' for ϕ from 10% to 30% considering low Reynolds number

This subsection covers the normalized torque results for neutrally-buoyant experiments as functions of Re and Re', respectively, considering low Reynolds numbers and solid fractions ranging from 10% to 30%.

Figure 4.21 shows the normalized torque measurements as functions of particle Reynolds number before the laminar-turbulent transition, considering polystyrene particles in the high-viscosity (blue data points) and low-viscosity (black data points) fluids, as well as SAN particles in the high-viscosity fluid (red data points). The plot also includes the rheological models for measurements of $\phi \leq 30\%$. The implemented measurements cover a Reynolds number regime from 0.51 to 48. As discussed in the contexts of Figure 4.19, both the measurements of the polystyrene and the SAN particles immersed in high-viscosity fluids are below the critical gap Reynolds number considering pure fluids. For $\phi = 0.1$, the effective viscosity is approximately constant for Re of $O(1)$. At $Re \approx 8$, the 10% SAN particle (red data) result is approximately 38% larger as compared to the 10% polystyrene (blue data) result. The uncertainty of the glycerol-ethanol temperature measurement may have contributed to the observed difference as discussed in the context of Figure 4.3. At the solid fractions of 20% and 30%, the polystyrene particle results (blue data) compare well with the SAN particle results (red data) immersed in high viscosity fluid for Re of approximately 10. As the shear rate increases, due to the contribution of the inertia of both the solid and the fluid phases, the effective viscosity gradually increases (Batchelor, 1970). The presence of the relatively large SAN particles may lead to velocity fluctuations in the flow that further increase the torque measurements (Cartellier and Riviere, 2001; Martinez et al., 2007; Mendez et al., 2013).

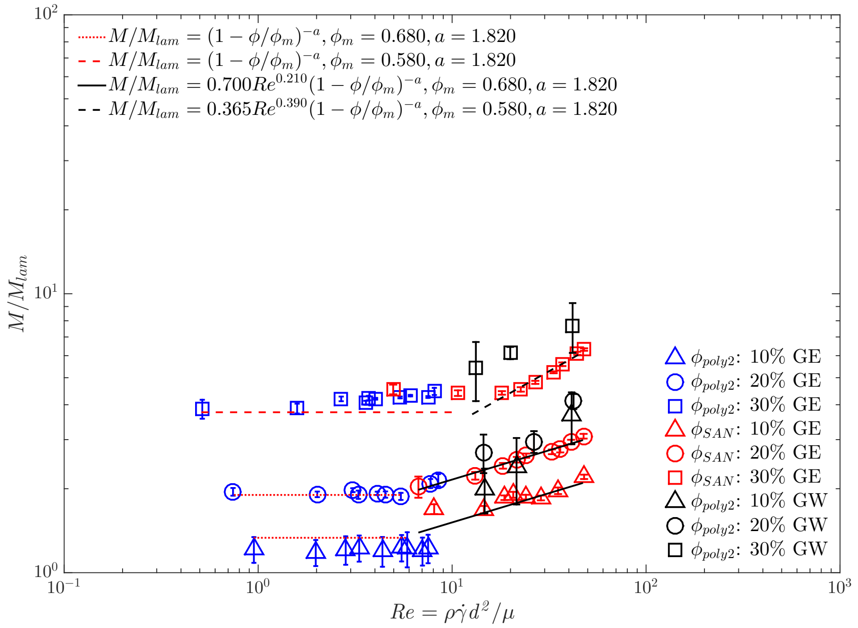

Figure 4.21: Direct torque measurements normalized by the laminar torque in terms of Re before the laminar-turbulent transition, considering 1.27 mm polystyrene particles in the fluid mixture of GE and GW, and 3.22 mm SAN particles in the fluid mixture of GE, with ϕ from 0.1 to 0.3. The red dotted lines and the red dashed line represent the Krieger-Dougherty correlations. The black solid lines and the black dashed line represent the rheological models for 10%, 20%, and 30% solid fractions. $\rho_p/\rho_f = 1$.

For comparison between the SAN particles (red data) immersed in the high-viscosity fluid and the polystyrene particles (black data) immersed the in low-viscosity fluid, at the 10%, 20%, and 30% solid fractions states, the polystyrene results (black data) are larger than the corresponding SAN results (red data) for overlapping Re regions from 13 to 43. However, some SAN measurement data points are still within the range of the error bars of the polystyrene results. The challenge to control the rheometer rotational speed at low shear rates to extend the polystyrene measurements to lower Reynolds numbers, contributes to the uncertainty in rotational speed measurement, and led to the relatively large error bars of the polystyrene results (black data).

Kriger-Dougherty correlations ($M/M_{lam} = (1 - \phi/\phi_m)^{-a}$) have been used to model the normalized torques for Re of $O(1)$. For Re from 0.5 to 6, the 10% and the 20% measurements are best modeled with Krieger-Dougherty relation using $a = 1.82$, and $\phi_m = 0.68$. But for the measurements of 30% solid fraction for Re from 0.5 to 10, the results are modeled with Krieger-Dougherty relation using $a = 1.82$, and $\phi_m = 0.58$. More extensive comparisons with simulation results as well as the Krieger-Dougherty and the Eilers relations are presented in Section 4.8. For Re of $O(10)$, the inertial effects play more important roles. Therefore, the 10% and 20% solid fractions results are best modeled as:

$$M/M_{lam} = 0.700Re^{0.210}(1 - \phi/\phi_m)^{-a} \tag{4.2}$$

where $\phi_m = 0.68$ and $a = 1.82$. The 30% results for Re of $O(10)$ show stronger dependence on the particle Reynolds number and is best modeled as:

$$M/M_{lam} = 0.365Re^{0.390}(1 - \phi/\phi_m)^{-a} \tag{4.3}$$

where $\phi_m = 0.58$ and $a = 1.82$.

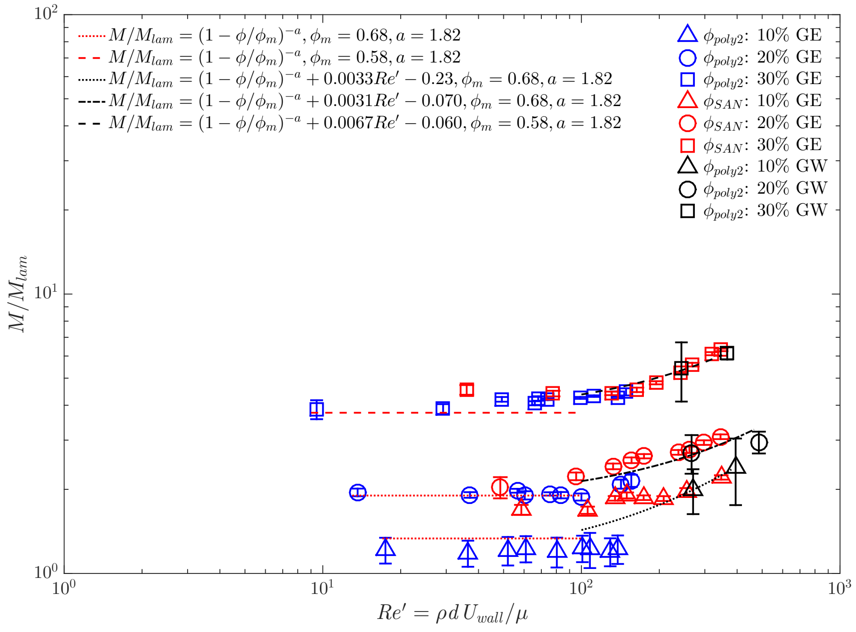

Figure 4.22: Direct torque measurements normalized by the laminar torque in terms of Re' before the laminar-turbulent transition, considering 1.27 mm polystyrene particles in the fluid mixture of GE and GW, and 3.22 mm SAN particles in the fluid mixture of GE, with ϕ from 0.1 to 0.3. The red dotted lines and the red dashed line represent the Krieger-Dougherty correlations. The black dotted line, the black dash-dotted line and the black dashed line represent the rheological models for 10%, 20%, and 30% solid fractions. $\rho_p/\rho_f = 1$.

Figure 4.22 shows the same normalized torque results before transition as functions of Re'. Re' is the non-dimensional Reynolds number that has a linear relationship with the particle diameter, d. Unlike the results in terms of particle Reynolds number, Re, the SAN particle and the polystyrene torque measurements have more overlapping regimes in terms of Re'. The 20% and 30% solid fractions measurements show agreement with what found in Figure 4.21. At the 10% solid fraction state, the normalized torques of SAN particles are larger as compared to the corresponding polystyrene results for Re' of approximately 100.

Figure 4.22 also presents the rheological fitting models in the form of M/M_{lam} vs. Re'. Over the Re' regime of $O(10)$, the red dotted lines and the red dashed line represent the same Krieger-Dougherty models using $a = 1.82, \phi_m = 0.68$ and $a = 1.82, \phi_m = 0.58$ as presented in Figure 4.21. For Re' of approximately 100, all the measurements start to show stronger dependence on Re'. Therefore, the normalized torques considering all measurements before the transition are modeled as linear relationships on the log-scale image and plotted for Re' of $O(100)$ as:

$$M/M_{lam} = (1 - \phi/\phi_m)^{-a} + 0.0033Re' - 0.23 \tag{4.4}$$

for $\phi = 10\%$, where $\phi_m = 0.68, a = 1.82$. The 20% solid fraction results before transition can be modeled as:

$$M/M_{lam} = (1 - \phi/\phi_m)^{-a} + 0.0031Re' - 0.070 \tag{4.5}$$

where $\phi_m = 0.68, a = 1.82$. The 30% solid fraction results before transition can be modeled as:

$$M/M_{lam} = (1 - \phi/\phi_m)^{-a} + 0.0064Re' - 0.060 \tag{4.6}$$

where $\phi_m = 0.58, a = 1.82$.

To further examine the rheological fitting models, the models in terms of M/M_{lam} vs. Re' are converted into the forms of M vs. $\dot{\gamma}$ considering the dynamic viscosity of 51% glycerol-ethanol mixture under the temperature of 20 °C. Then the converted models are compared with the quadratic fitting models considering direct torque measurements of SAN particles immersed in the glycerol-ethanol mixture from Figure 4.5, and the comparison results are presented in Table 4.1. For $\phi = 10\%$

ϕ	**Torque fitting from Figure 4.5**	**Converted model for M/M_{lam} vs. Re'**
10%	$M = 3.1 \times 10^{-6}\dot{\gamma}^2 + 7.5 \times 10^{-4}\dot{\gamma}$	$M = 4.8 \times 10^{-6}\dot{\gamma}^2 + 5.9 \times 10^{-4}\dot{\gamma}$
20%	$M = 5.4 \times 10^{-6}\dot{\gamma}^2 + 9.0 \times 10^{-4}\dot{\gamma}$	$M = 4.4 \times 10^{-6}\dot{\gamma}^2 + 9.7 \times 10^{-4}\dot{\gamma}$
30%	$M = 1.6 \times 10^{-5}\dot{\gamma}^2 + 1.3 \times 10^{-3}\dot{\gamma}$	$M = 9.8 \times 10^{-6}\dot{\gamma}^2 + 2.0 \times 10^{-3}\dot{\gamma}$

Table 4.1: Comparison of rheological models for ϕ from 10% to 30%. The data in Figure 4.5 considers SAN particles immersed in high-viscosity fluids. The converted models use all data for $Re' < 400$.

and 20%, the coefficients for $\dot{\gamma}$ and $\dot{\gamma}^2$ compare well between the direct torque measurement model and the model converted from M/M_{lam}. In the examination of the 30% solid fraction model, the coefficient for $\dot{\gamma}^2$ from the torque fitting model is 63% larger than the corresponding coefficient from the M/M_{lam} fitting model. However, for the coefficients of $\dot{\gamma}$ for the same solid fraction, the torque fitting coefficient is 35% smaller in comparison with the M/M_{lam} fitting value. The differences between the model coefficients are expected since the torque fitting model only considers the torque measurements of SAN particles in high-viscosity fluids (the corresponding normalized torques are labelled in red in Figure 4.22), while the model considering M/M_{lam} vs. Re' fits all the measurements before transition. However, the similarities between the torque fitting and the normalized torque fitting models suggest that M has a quadratic relationship in terms of $\dot{\gamma}$ for Re' of $O(100)$.

There are two assumptions for the model comparisons in Table 4.1. Even though most of the measurements before the transition were measured under the liquid temperature of 20 °C, the measurements with higher solid fractions towards the highest shear rate have slightly higher fluids temperature, which is discussed in detail in Chapter 2. The temperature variation has been taken into account for torque normalization, but for the model conversion from M/M_{lam} vs. Re' to M vs. $\dot{\gamma}$, it is assumed a consistent dynamic viscosity of high-viscosity fluid under 20 °C. The effects of the temperature variations for the rheological model fitting are limited since the liquid temperature variations were deliberately controlled for each measurement. On the other hand, the M_o values for the torque fittings from Figure 4.5 are neglected as discussed in Section 4.2 since the M_o values approach the torque sensor resolution limit.

To quantify the matching differences among the results in Figure 4.21 and Figure 4.22 separately, Table 4.2 summarizes the root mean square values considering the

ϕ	**RMS in Figure 4.21**	**RMS in Figure 4.22**
10%	0.5433	0.1801
20%	0.3746	0.2038
30%	0.9552	0.1856

Table 4.2: Root mean square of the deviation of measurements from the fitting curves considering M/M_{lam}. The data in Figure 4.5 considers the root mean square of the measurement deviation for Re from 10 to 100. The data in Figure 4.21 considers the root mean square of the measurement deviation for Re' from 100 to 400.

measurement deviations (M/M_{lam}) from the fitting models. At the state of the 10% solid fraction, the RMS of the matching difference in Figure 4.21 for Re from 10 to 100 is 0.5433. The corresponding RMS for the same data points in Figure 4.22 for Re' from 100 to 400 is 0.1801, which is approximately 3 times less than the matching value in terms of Re. The RMS values in Figure 4.22 are 0.2038 and 0.1856 for the 20% and 30% solid fractions, respectively, which are approximately 1.8 and 5 times less the corresponding RMS values in Figure 4.21.

In summary, for low-Reynolds-number particulate flows considering neutrally buoyant particles for Re from 0.51 to 48, the shear stress can be modeled using the effective viscosity that only depends on the particle solid fraction for particle Reynolds number of $O(1)$ and ϕ less than 30%. As the particle Reynolds number further increases, the effective viscosity also depends on the particle Reynolds number. Once the normalized torque results are plotted in terms of Re', M/M_{lam} is best modeled with the linear relationship of Re'.

Normalized torque as functions of Re and Re' for ϕ from 10% to 30% considering intermediate Reynolds number

Figure 4.23 shows the torque measurement, M/M_{lam}, in terms of Re for SAN particles (red markers) and polystyrene particles (black markers) immersed in high-viscosity and low-viscosity fluids separately, covering an intermediate Reynolds number region from 4.97 to 135. The SAN results show a relatively smooth transition while the polystyrene results show a sharp increase in terms of torque magnitudes. The shear-thickening behaviors of the SAN and polystyrene results are caused by different factors. For the SAN particles in the high-viscosity fluids, the increasing normalized torques are mainly caused by the inertial effects. While for

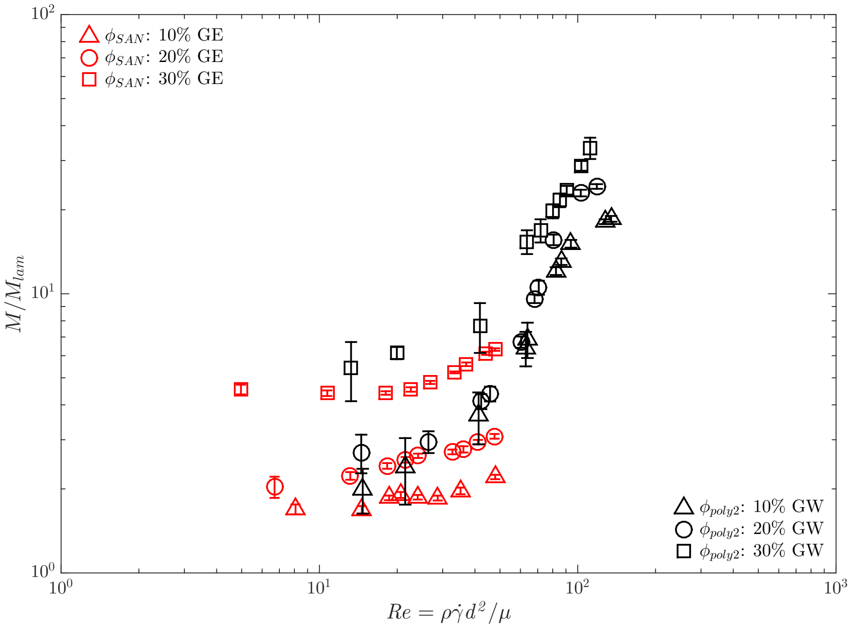

Figure 4.23: Direct torque measurements normalized by the laminar torque in terms of *Re*, considering polystyrene particles in the fluid mixture of GW, and SAN particles in the fluid mixture of GE, with ϕ from 0.1 to 0.3.

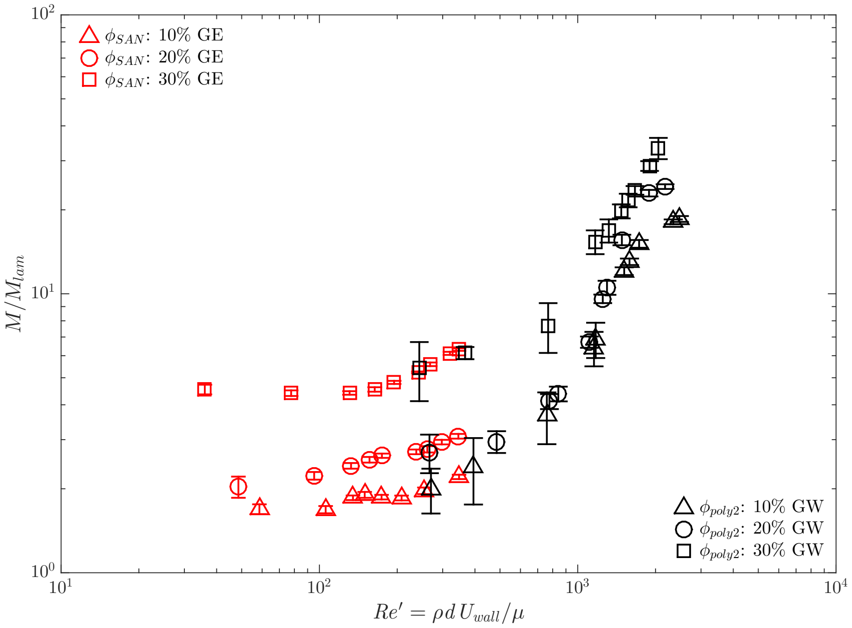

Figure 4.24: Direct torque measurements normalized by the laminar torque in terms of *Re′*, considering polystyrene particles in the fluid mixture of GW, and SAN particles in the fluid mixture of GE, with ϕ from 0.1 to 0.3.

the polystyrene particles immersed in the fluid mixture of glycerol and water, the torque measurements are near the transition to turbulence in comparison with the results of the pure fluids as discussed in the context of Figure 4.17. Besides the laminar-turbulent transition, the increasing inertial effects and the velocity fluctuations have contributed to the relatively larger normalized torques of the polystyrene results than the SAN results.

In Figure 4.24, the torque measurements for the same SAN and polystyrene particles in glycerol-ethanol and glycerol-water mixtures are presented as functions of Re'. At the 10%, 20%, and 30% solid fractions, the polystyrene results match closely with the SAN results for Re' from 243 to 347, showing a gradual increase in normalized torque followed by a significant jump at $Re' \approx 485$.

In summary, for neutrally-buoyant experiments with solid fractions from 10% to 30% over the Re region from 4.97 to 135, the effective viscosity increases with the Reynolds number of $0(1)$, followed by a sharp jump of effective viscosity for Reynolds number of $O(10)$, which corresponds to the regime near the transition to turbulence.

Normalized torque as functions of Re and Re' for ϕ from 10% to 30% considering high Reynolds number

Figure 4.25 shows both sets of polystyrene (black markers) and SAN (green markers) immersed in low viscosity mixtures (glycerol-water), covering a particle Reynolds number region from 13.2 to 773. For solid fractions from 10% to 30%, the polystyrene data sets in glycerol-water mixtures show sharp transitions in terms of effective viscosity, followed by a relatively smoother increase of effective viscosity for SAN results. For the 10% solid fraction state, the polystyrene data sets (black) show a transition trend from a sharp increase to a gradual increase. The Caltech Couette flow device was run at its maximum rotational speeds. Unfortunately, there is no overlap in Re between the two results corresponding to the 10% solid fraction. It is anticipated that the 10% solid fraction polystyrene result can eventually match with the corresponding SAN data set if the torque measurements are extrapolated to higher particle Reynolds numbers around 150. A similar change of shear-thickening behavior is observed at the 20% solid fraction state, with the polystyrene effective viscosity approximately 32% higher than the SAN effective viscosity for $Re \approx 120$. At the state of 30%, even though the polystyrene and SAN data sets have no overlapping Reynolds number regimes, it is expected that the polystyrene data sets can catch up with the SAN data if the measurements are extended to higher Reynolds numbers. As discussed in detail in Figure 4.17 and Figure 4.18, both the results of the polystyrene and the SAN particles in the low-viscosity fluids are affected by the laminar-turbulent transition, but in different ways. The polystyrene results (black data points) are near the transition to turbulence, but the smaller polystyrene particles suppress the turbulence as compared to the results of the pure fluids. While for the SAN particle results, the relatively larger SAN particles enhance the turbulence in comparison with the results of the pure fluids. Since the corresponding Stokes number regions for the measurements are from 1.4 to 85.9, the SAN particle collisions play an increasingly important role in the SAN particle torque measurements, which have *St* greater than 10. However, without the direct particle collisional pressure measurements, it is challenging to determine the relative contributions to the normalized torque from the polystyrene particle collisions.

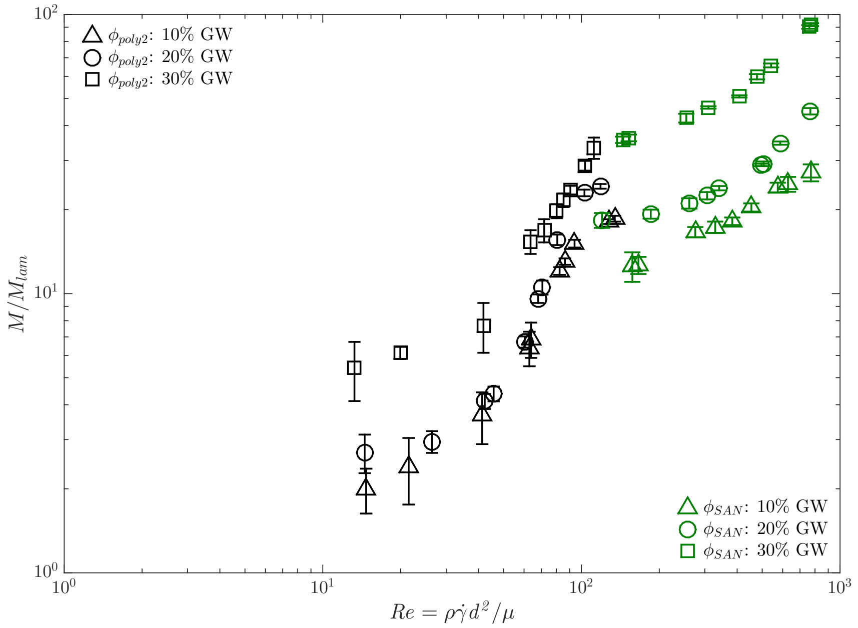

Figure 4.25: Direct torque measurements normalized by the laminar torque in terms of Re, considering polystyrene and SAN particles in the fluid mixture of glycerol and water, with ϕ from 0.1 to 0.3. $\rho_p/\rho_f = 1$.

To further study the impact of particle sizes on the torque measurements, the same data sets of SAN and polystyrene particles immersed in low-viscosity fluids are presented in terms of Re' in Figure 4.26. At the 10% and 20% solid fractions, the SAN and the polystyrene data sets compare well for Re' from 1×10^3 to 2×10^3. For

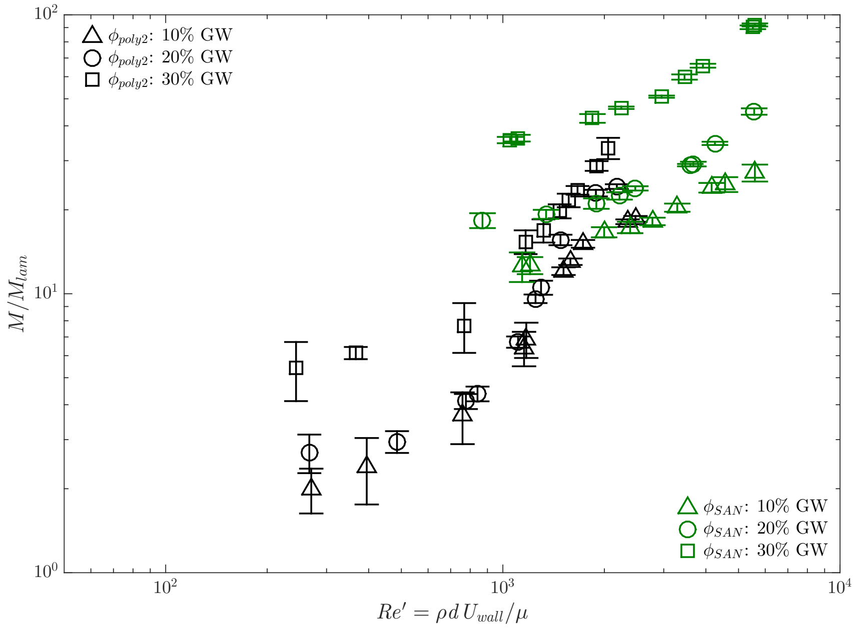

Figure 4.26: Direct torque measurements normalized by the laminar torque in terms of Re', considering polystyrene and SAN particles in the fluid mixture of glycerol and water, with ϕ from 0.1 to 0.3. $\rho_p/\rho_f = 1$.

the overlapping Re' regions of the 30% solid fraction, the SAN effective viscosities are slightly greater than the polystyrene results.

In summary, for neutrally-buoyant measurements considering high particle Reynolds number regions with Re from 13.2 to 773, the effective viscosities increase substantially for particle Reynolds number of $O(10)$ and solid fractions less than 30%. In comparison with the pure fluids measurements, the particles either enhance or suppress the transition to turbulence based on the different particle sizes. For experiments of Reynolds of $O(100)$ and ϕ less than 40%, the effective viscosities continuously increase with Reynolds numbers, but at slower rates. Once the results using high viscosity fluids are plotted with respect to Re', the SAN and polystyrene results show good agreements during the overlapping Reynolds number regimes for ϕ less than 30%.

Normalized torque as functions of Re and Re' for ϕ from 10% to 30% considering all Reynolds number regimes

Figure 4.27 shows the direct torque measurements normalized by the laminar torque in terms of Re for SAN and polystyrene particles in the glycerol-ethanol and glycerol-water mixtures, respectively, with solid fractions from 10% to 30%. Each data set with specified particles and suspending liquids is presented with the same color as shown in previous subsections (See previous figures for detailed legends of experimental data). For polystyrene particles in the fluid mixture of glycerol and ethanol (blue data set) with solid fractions from 10% to 30%, the effective viscosity is approximately constant, and then increases slightly at the highest shear rate. For SAN particles in the glycerol-water mixture (red data set) with solid fractions from 10% to 30%, the effective viscosity continuously increases over the Reynolds number range from 10 to 100. The 20% and the 30% results compare well with the corresponding torque measurements from polystyrene GE results. For polystyrene particles in the fluid mixture of glycerol and water (black data set), with solid fractions from 10% to 30%, the effective viscosity increases significantly over the Re range from 20 to 100, which is affected by the transition to turbulence. For SAN particles in the glycerol-water mixture (green data set), over the solid fractions range from 10% to 30%, experimental results show an increased dependence of effective viscosity on $\dot{\gamma}$, and the measurements are already in the turbulent regimes.

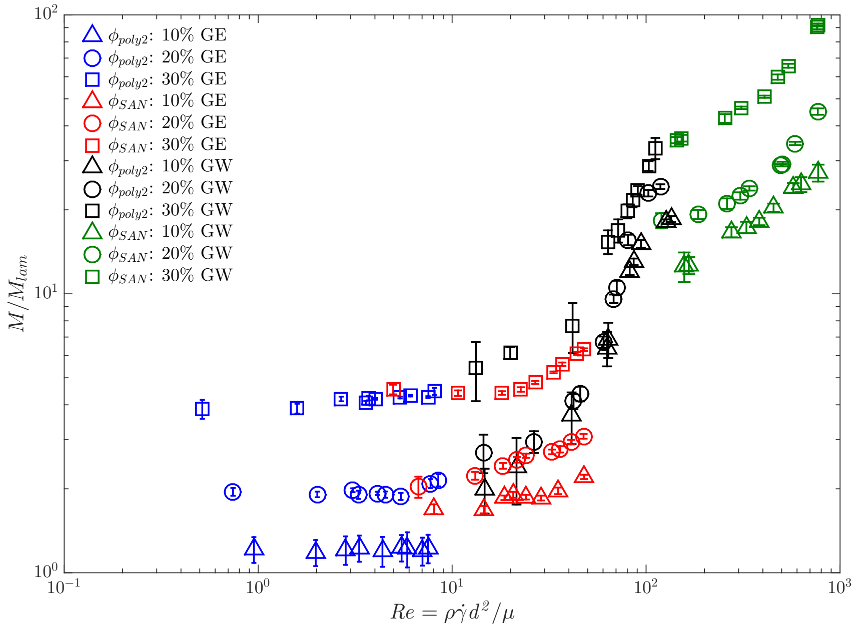

Figure 4.27: Direct torque measurements normalized by the laminar torque in terms of Re, considering polystyrene and SAN particles in the fluid mixture of GE and GW, with ϕ from 0.1 to 0.3. $\rho_p/\rho_f = 1$.

Figure 4.28 shows the normalized torque measurements, M/M_{lam}, for all data sets

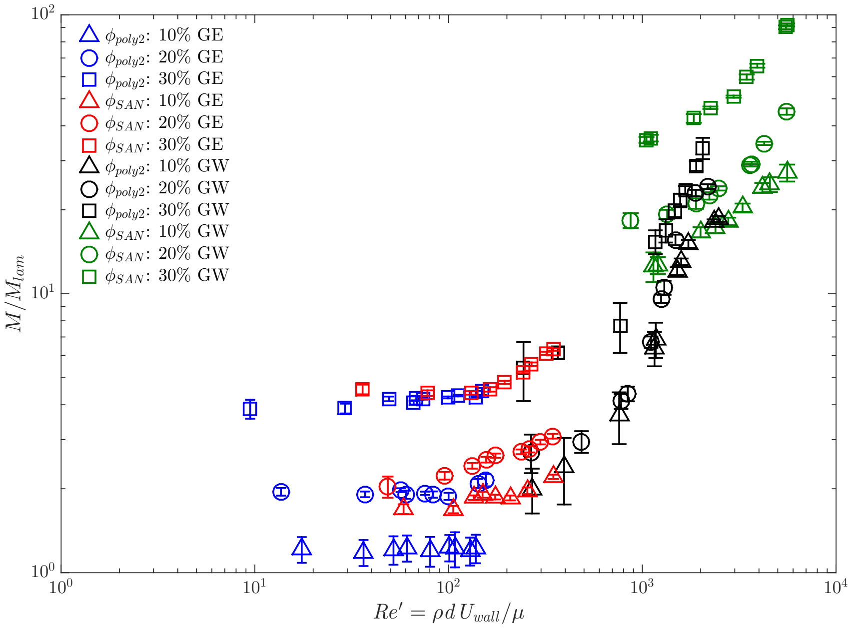

Figure 4.28: Direct torque measurements normalized by the laminar torque in terms of Re', considering polystyrene and SAN particles in the fluid mixture of GE and GW, with ϕ from 0.1 to 0.3. $\rho_p/\rho_f = 1$.

in terms of Re' over the solid fraction range from 10% to 30%. In looking at all of the data of 10%, 20%, and 30% solid fractions as found in Figure 4.28, the torque results as a function of Re' match better for solid fractions from 10% to 30%. This indicates that torque measurement results with ϕ from 10% to 30% have better correlations with respect to Re' (linear relationship of d) as compared to Re (square relationship of d).

In summary, the neutrally-buoyant results considering ϕ from 10% to 30% show an increased dependence of effective viscosity over the Reynolds number regime examined.

$(M - M_o)/M_{lam}$ as functions of Re and Re' considering 40% and 50% solid fractions for all Reynolds number regimes

This section introduces a new method to normalize the measured torque (M) by taking the M_o at the stationary states into account for solid fractions of 40% and 50%.

As shown in Figure 4.19 and Figure 4.20, all the 50% M/M_{lam} results show shear-thinning behaviors. However, there are relatively large M_o values for 40% and 50%

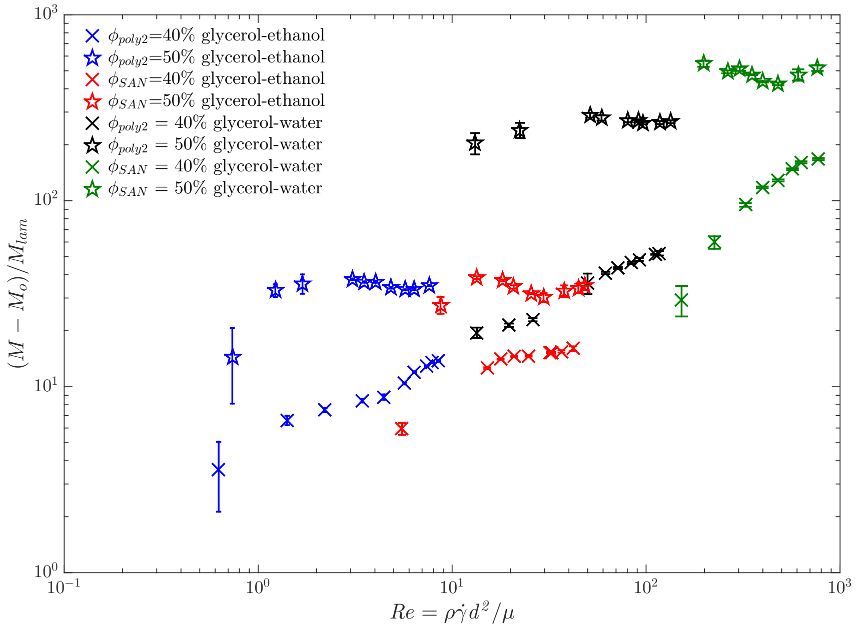

Figure 4.29: $(M - M_o)/M_{lam}$ in terms of of Re for 3.22 mm SAN particles and 1.27 mm polystyrene particles in the fluid mixtures of GE and GW, with ϕ from 0.4 to 0.5. $\rho_p/\rho_f = 1$.

direct torque measurements found in Section 4.2 and 4.3. Therefore, $(M - M_o)/M_{lam}$ as functions of Re considering all 40% and 50% measurements are presented in Figure 4.29 to separate the effects of yield stresses at $\dot{\gamma} = 0$. The M_o values from the 40% quadratic fitting curves for high-viscosity fluids and the M_o values from the 40% cubic fitting curves for low-viscosity fluids are found in Figure 4.2, Figure 4.6, Figure 4.10, and Figure 4.14. All the 50% M_o values considered in the calculations are from the linear fitting curves. Over the Reynolds number regimes examined, the 40% results continuously increase with the increasing particle Reynolds number. The shear thickening behaviors for Re of $O(1)$ and $O(10)$ are mainly driven by the increasing inertial effects of the liquid and solid phases, but the increasing behaviors for Re of $O(100)$ are affected by the turbulence. For the highest solid fractions of 50%, the experimental results have increased by a factor of 3 in the magnitude as compared to the 40% results, but show relatively consistent values over Re for each data set.

The same $(M - M_o)/M_{lam}$ data sets are plotted with respect to Re' in Figure 4.30. The 40% results show better agreements as compared to Figure 4.29. The 40% measurements before transition are best fitted with a linear relationship as

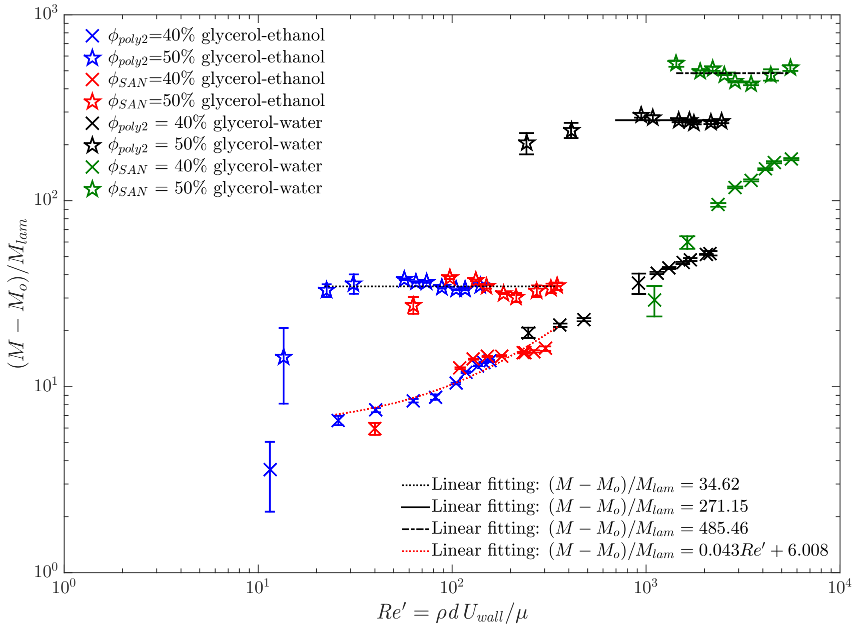

Figure 4.30: $(M-M_o)/M_{lam}$ as a function of Re' for SAN and polystyrene particles immersed in glycerol-water (GW) and glycerol-ethanol (GE) mixtures, with ϕ from 40% to 50%. $\rho_p/\rho_f = 1$. The linear fitting curve is $(M-M_o)/M_{lam} = 34.62$ for the 50% SAN and polystyrene particles immersed in high-viscosity fluids. The linear fitting curves are $(M-M_o)/M_{lam} = 271.15$ and $(M-M_o)/M_{lam} = 485.46$ for 50% polystyrene and 50% SAN particles immersed in low-viscosity fluids. The linear curve for the 40% measurements before transition is $(M-M_o) = 0.043Re' + 6.008$.

$(M-M_o)/M_{lam} = 0.043Re' + 6.008$. Following that, using the similar methods and assumptions discussed in the context of Table 4.1, the fitting model using $(M-M_o)/M_{lam}$ vs. Re' is converted to the form of $(M-M_o)$ vs. $\dot{\gamma}$ and compared with the quadratic fitting models for polystyrene (see Figure 4.2 for details) and SAN (see Figure 4.6 for details) particles immersed in high-viscosity fluids in Table 4.3. The models share the same format of quadratic relationship of $(M-M_o)$ in terms of $\dot{\gamma}$, which is consistent with the rheological models presented in Table 4.1 for the 10%, 20%, and 30% measurements before transition. The differences of coefficients for $\dot{\gamma}$ and $\dot{\gamma}^2$ are anticipated since the fitting of normalized torques consider all measurements before transition, but the fitting models of direct torque measurements only consider the SAN and polystyrene particles immersed in glycerol-ethanol mixtures, separately.

The 50% polystyrene results in glycerol-ethanol (blue data sets) and the 50% SAN results in glycerol-ethanol (red data sets) match closely for Re' around 100. Both data

40% fitting curves	**Rheological model**
Conversion of $(M - M_o)/M_{lam}$ vs. Re'	$M - M_o = 6.3 \times 10^{-5}\dot{\gamma}^2 + 3.2 \times 10^{-3}\dot{\gamma}$
$(M - M_o)$ vs. $\dot{\gamma}$ for polystyrene in GE	$M - M_o = 3.5 \times 10^{-5}\dot{\gamma}^2 + 2.4 \times 10^{-3}\dot{\gamma}$
$(M - M_o)$ vs. $\dot{\gamma}$ for SAN in GE	$M - M_o = 1.4 \times 10^{-5}\dot{\gamma}^2 + 7.0 \times 10^{-3}\dot{\gamma}$

Table 4.3: Comparison of rheological models for $\phi = 40\%$. The data of polystyrene and SAN particles in high viscosity fluids are from Figure 4.2 and Figure 4.6. The converted models use all data for $Re' < 400$.

50% fitting curves	**Rheological model**
Conversion of $(M - M_o)/M_{lam}$ vs. Re'	$M - M_o = 1.86 \times 10^{-2}\dot{\gamma}$
$(M - M_o)$ vs. $\dot{\gamma}$ for polystyrene in GE	$M - M_o = 1.90 \times 10^{-2}\dot{\gamma}$
$(M - M_o)$ vs. $\dot{\gamma}$ for SAN in GE	$M - M_o = 1.80 \times 10^{-2}\dot{\gamma}$

Table 4.4: Comparison of rheological models for $\phi = 50\%$. The data of polystyrene and SAN particles in high viscosity fluids are from Figure 4.2 and Figure 4.6. The converted models use all data for $Re' < 400$.

sets are best modeled using $(M - M_o)/M_{lam} = 34.62$. Therefore, the 50% results in high-viscosity fluids do not depend on the particle size, and the normalized torques are nearly independent of Re and Re'. Similar to the model comparison in Table 4.3, the normalized torque fitting model is converted to the form of $(M - M_o)/M_{lam}$ and compared with the 50% linear fitting models for polystyrene (see Figure 4.2 for details) and SAN (see Figure 4.6 for details) mixed with high-viscosity fluids in Table 4.4. The coefficients for $\dot{\gamma}$ match closely for three models. The 50% results considering polystyrene particles immersed in low-viscosity fluids (black data sets) are best modeled as $(M - M_o)/M_{lam} = 271.15$, which is 7.8 times larger than the 50% measurement in laminar regime. This substantial magnitude difference at the 50% solid fraction state indicates the significant effects of turbulence. The 50% solid fraction SAN results in the glycerol-water mixture (green data sets) are best modeled as $(M - M_o)/M_{lam} = 485.46$, which is 1.79 times larger than the 50% measurement of polystyrene particles immersed in low-viscosity fluids. The different levels of turbulent effects have contributed to the differences in $(M - M_o)/M_{lam}$.

In summary, once the torques (M) are normalized using $(M - M_o)/M_{lam}$ rather than M/M_{lam}, the 40% results show stronger dependence on the particle Reynolds number, and the 50% results for each data set are nearly independent of particle Reynolds number. The 40% and 50% results considering $(M - M_o)/M_{lam}$ also show better matching results with respect to Re' in comparison with Re.

Conclusion

As shown in the Figure 1.2, there are simulation papers considering liquid-solid flows of intermediate Reynolds numbers (Kulkarni and Morris, 2008; Yeo and Maxey, 2013; Picano et al., 2013; Rahmani et al., 2018). The present experimental results, with Re from 0.51 to 773, have significantly extended the Reynolds number regime in comparison with the Re regions examined in the numerical studies. Unlike the widely used $Re = \rho_f \dot{\gamma} d^2/\mu$ in the simulation papers concerning rheological measurements of intermediate particle Reynolds numbers, the present experimental measurements ($Re = 0.51$ to $Re = 773$) show that M/M_{lam} for ϕ from 10% to 30% and $(M-M_o)/M_{lam}$ for ϕ from 40% to 50% correlate better with $Re' = \rho_f d U_{wall}/\mu$.

4.6 Comparison between experimental results with respect to Re_b' and G'

This section examines the torque measurement differences considering two particle types with respect to Re_b' and G' in detail.

With the purpose to separate the effects from the solid fractions, a defined effective viscosity ($\mu' = \mu(1-\phi/\phi_m)^{-1.82}$) is introduced to calculate the defined gap Reynolds number ($Re_b' = \rho_f \dot{\gamma} r_o b/\mu'$) and normalize the torque measurement (Matas et al., 2003). The normalized torque (M/M_{lam}') is plotted with Re_b' to further investigate the transitional flows. Furthermore, to examine the experimental measurements of SAN and polystyrene particles in the laminar and turbulent regions separately, the experimental measurements are presented using an effective viscosity model considering the normalization of $G' = M/(H\mu'^2/\rho)$ as a function of Re_b'.

To separate the effects of the solid fractions, μ' ($\mu' = \mu(1-\phi/\phi_m)^{-1.82}$) is calculated using the Krieger-Dougherty relation (Krieger, 1972; Phillips et al., 1992). ϕ_m is equal to 0.68 considering the random close packing for spherical particles. Then the μ' is used to normalize Re_b and M_{lam} to obtain Re_b' and M'_{lam}.

$$Re_b' = \frac{\rho \omega r_o b}{\mu(1-\phi/\phi_m)^{-1.82}}. \tag{4.7}$$

$$M_{lam}' = 2\pi\mu(1-\phi/\phi_m)^{-1.82}\dot{\gamma} H {r_i}^2. \tag{4.8}$$

M_{lam}' is used to normalize the measured torque (M), and the results are presented in terms of Re_b' in Figure 4.31 for ϕ of 10%, 20%, and 30%. After the normalization using μ', the normalized torques of 10%, 20%, and 30% solid fractions have appeared to move closer, but the slopes are shallower than the turbulent pure fluid result. As discussed in Figure 3.3, the pure fluids measurements show a transition to turbulent flow for Re_b around 6.5×10^3, as indicated by the dashed line in Figure 4.18. Once the SAN particles are added to the flow, the torque measurements also show a laminar-turbulent transition. However, in comparison with the pure fluids critical Reynolds number, the presence of the larger particles has caused the transition to happen at smaller critical Reynolds numbers. In addition, the critical Reynolds number also depends on ϕ. The liquid-solid flows with higher solid fractions transition to turbulent flows at lower critical Reynolds numbers. This observation is consistent with the measurements from Matas et al. (2003) using relatively large particles in pipe flows.

Finally, using the μ' from Krieger-Dougherty relation, the measured torque M is normalized using the following equation:

$$G' = \frac{M}{\frac{H\mu'^2}{\rho}}. \tag{4.9}$$

The torque normalization using G' are presented in terms of Re_b' considering SAN particles in low-viscosity and high-viscosity fluids for $\phi = 0.1, 0.2, 0.3$, and 0.4. The 0% solid fraction results for the laminar and the turbulent flows are also plotted as solid and dashed lines, respectively. For laminar flows of pure fluids, G' has a linear relationship with Re_b'. While for the turbulent flows considering pure fluids beyond the critical Reynolds number, G' has a correlation of $Re^{1.695}$ (Ravelet, Delfos, and Westerweel, 2010). For measurements of SAN particles immersed in the glycerol-ethanol solution, the 10% and the 20% solid fractions results match with the laminar pure fluid curves closely at low shear rates, but start to deviate from the laminar pure fluids results as shear rate increases, showing a higher dependence of Re_b'. At the solid fractions of 30% and 40%, the measurements using glycerol-ethanol show higher magnitudes of G', but still have similar slopes as compared to the laminar pure fluids results. For the results immersed in the glycerol-water mixture, all data sets share similar slopes with the turbulent pure fluids curves. The magnitudes of the 10% and 20% solid fractions results compare well with the turbulent pure fluid results, but the 30% and the 40% have higher G' values. In summary, the SAN particles results immersed in low- and high-viscosity fluids show clear differences in the dependence of Re_b', with higher slopes of turbulent results as compared to

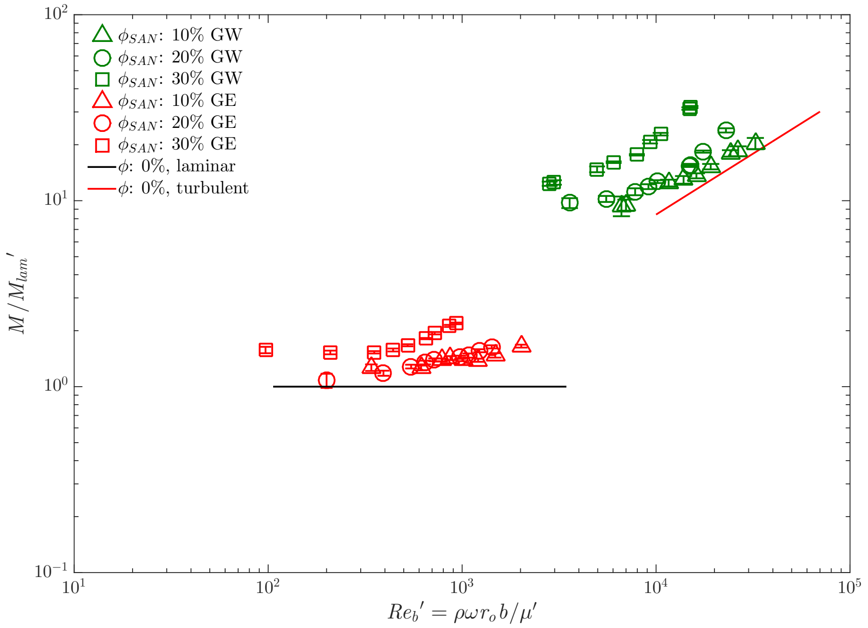

Figure 4.31: Direct torque measurement normalized by theoretical laminar torque in terms of effective gap Reynolds number considering SAN particles in the fluid mixtures of GE and GW, with solid fractions of $\phi = 0.1$, 0.2, and 0.3.

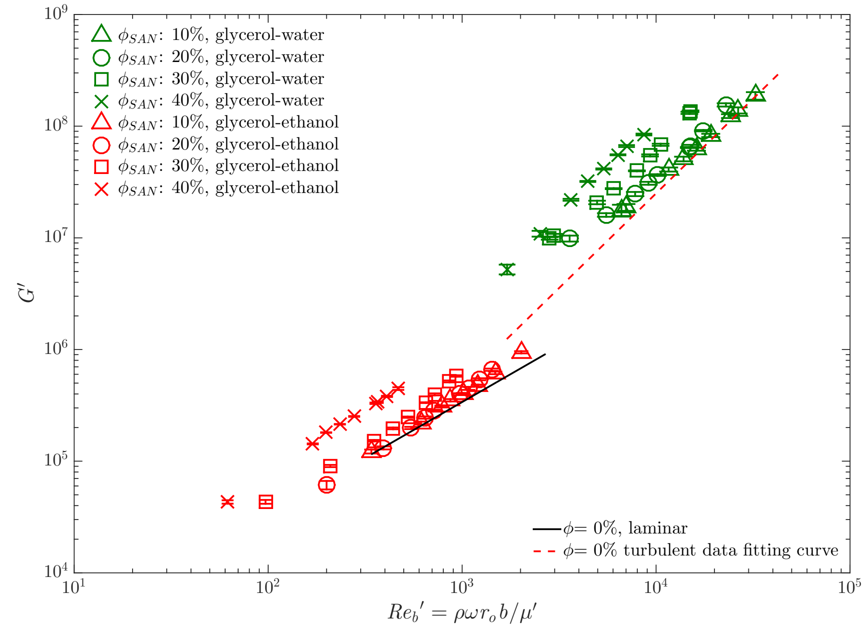

Figure 4.32: Normalized torque results for the SAN particle measurements, G' in terms of $Re_b{}'$ based on the Krieger-Dougherty model. The results include solid fractions of $\phi = 0.1$, 0.2, 0.3, and 0.4.

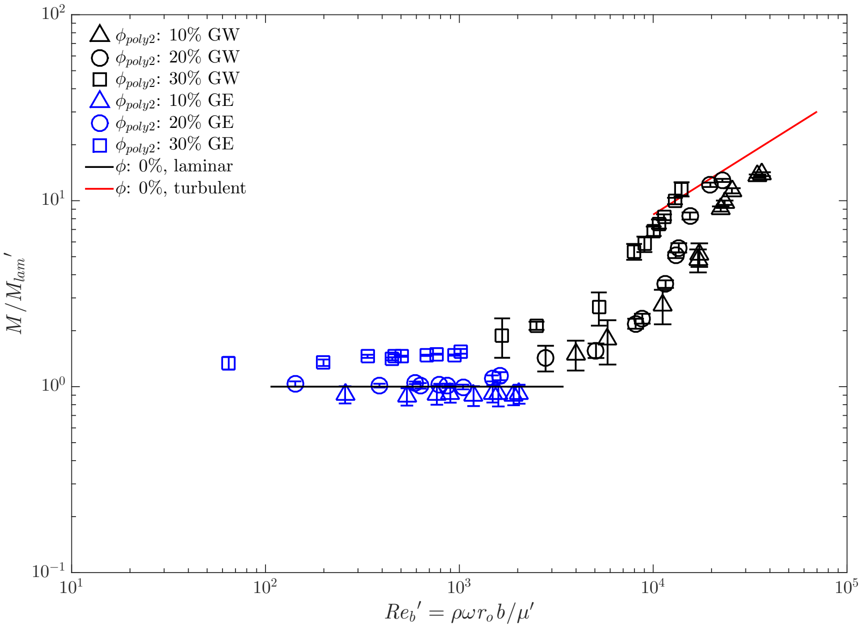

Figure 4.33: Direct torque measurement normalized by theoretical laminar torque in terms of effective gap Reynolds number considering polystyrene particles in the fluid mixtures of GE and GW, with solid fractions of ϕ = 0.1, 0.2, and 0.3.

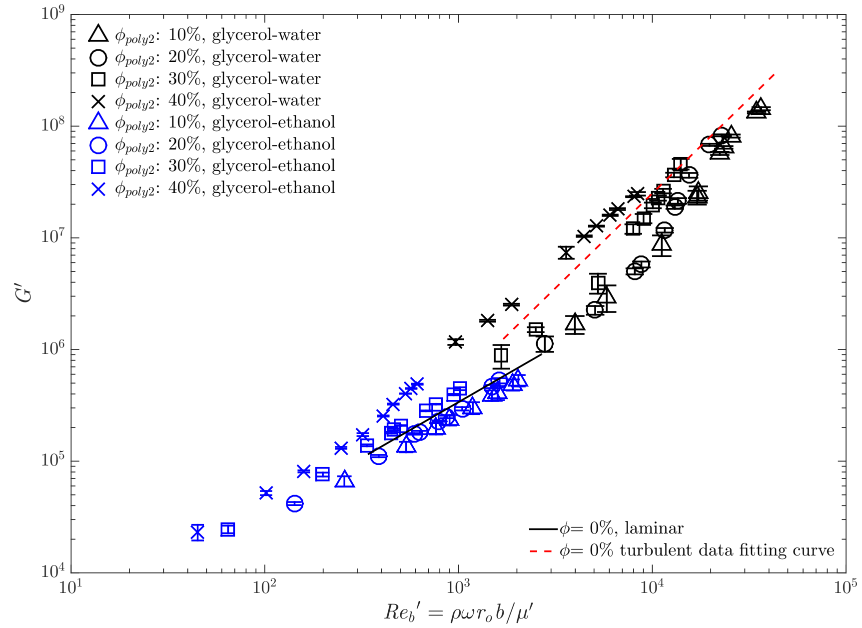

Figure 4.34: Normalized torque results for the polystyrene particle measurements, G' in terms of Re_b' based on the Krieger-Dougherty model. The results include solid fractions of ϕ = 0.1, 0.2, 0.3, and 0.4.

the laminar results.

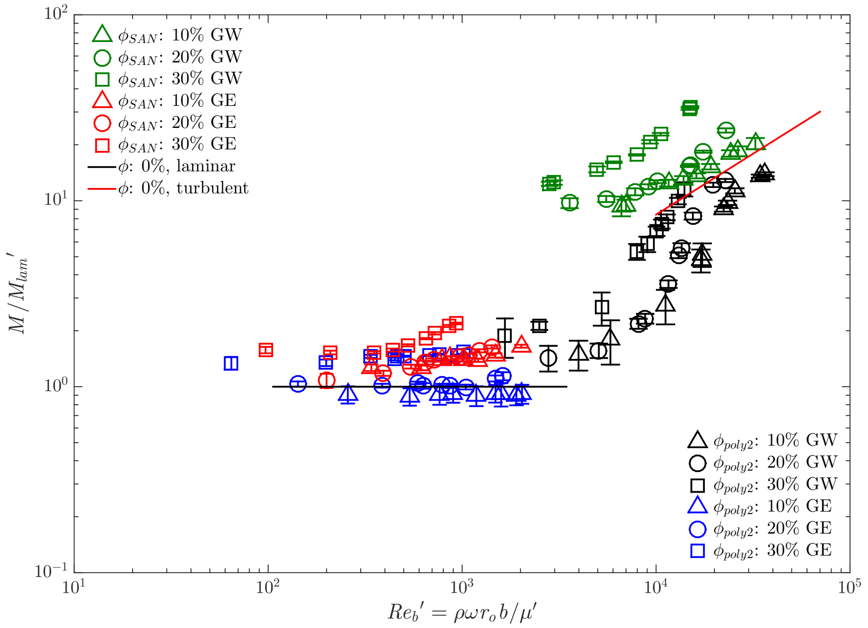

Figure 4.35: Direct torque measurement normalized by theoretical laminar torque based on the Krieger-Dougherty model in terms of effective gap Reynolds number considering polystyrene and SAN particles in the fluid mixture of glycerol-ethanol and glycerol-water, separately. The results include solid fractions of ϕ = 0.1, 0.2, and 0.3.

The polystyrene torque measurement (M) and the gap Reynolds numbers (Re_b) are normalized using μ', and the results are shown in Figure 4.33. After the normalization using μ', polystyrene results with different solid fractions move closer. As compared with the results using relatively larger SAN particles shown in Figure 4.31, the flows with polystyrene particles transition to turbulent flows at higher critical Reynolds numbers with smaller magnitudes over the same $Re_b{}'$ regions tested.

Furthermore, Figure 4.34 shows the results of G' in terms of $Re_b{}'$ considering polystyrene particles in low-viscosity and high-viscosity fluids for solid fractions of 10%, 20%, 30%, and 40%. The solid line and the dashed line are the same pure fluids curves for laminar flow and turbulent flow as shown in Figure 4.32. For results (blue data points) using the glycerol-ethanol mixture, the 10%, 20% and 30% solid fraction results have similar slopes as compared to the laminar pure fluid curve. For the 40% solid fraction results using the glycerol-ethanol mixture, it shows a higher dependence of ${Re_b}'$ than the laminar pure fluids. For the results (black data points) using glycerol-water mixture, the normalized values (G') of 10%, 20%, and 30% are smaller than the turbulent pure fluids curve at low shear rates, as the particulate flows are still near the transitions to the turbulent flows. Once the flows reach the fully-turbulent states, the magnitudes and the slopes of the 10%, 20%, and 30% results compare well with the turbulent pure fluids results. For the higher solid fraction (40%) result using glycerol-water mixture, it has a higher magnitude of G' in comparison with the turbulent pure fluids results, but shares a similar slope.

In summary, all torque measurements using the normalization of $M/{M_{lam}}'$ as a function of ${Re_b}'$ considering solid fractions from 10% to 30% are presented in Figure 4.35. In the laminar region, the normalized results of SAN particles are larger than the polystyrene results, and have higher dependence with respect to ${Re_b}'$. In the turbulent regime, the polystyrene measurements have smaller magnitudes of normalized torques than the corresponding SAN results, but they have a higher dependence on ${Re_b}'$ as the flows transition to the turbulent regimes.

4.7 Comparison with previous experimental results

This section examines the current rheological measurements in comparison with the previous experimental measurements. The normalized torques from present and previous experimental studies are compared with respect to the particle Reynolds number first. Then the comparison of the same normalized torques is examined using the Reynolds number using the maximum velocity, Re', which is introduced in Section 4.5.

Figure 4.36 shows on the log scale the normalized torque results using SAN particles immersed in high-viscosity fluid, along with the experimental results from Linares et al. (2017) for ϕ ranges from 10% to 50%. The Linares results use elliptical polystyrene particles, which differ from the SAN particles in particle shape, but have similar effective particle diameter. For ϕ = 0.1, the effective viscosity, or equivalently the normalized torque, in Linares data is approximately constant for Re from 17 to 39. The current data for the 10% solid fraction shows a similar trend as the Reynolds number increases, but is approximately 50% larger as compared to the Linares results around the maximum shear rate. For ϕ = 20% and 30%, both normalized torques increase slightly over the Re regime tested, and the current data compare well with the measurements from Linares. At ϕ of 40%, Linares data showed a slight decreasing behavior followed by an increase for Re from 20.6 to

40.6. Both the 50% results decrease with increasing Re. At the maximum shear rate, the current normalized torques are 42% and 73% higher than the Linares measurements for 40% and 50% solid fractions, respectively.

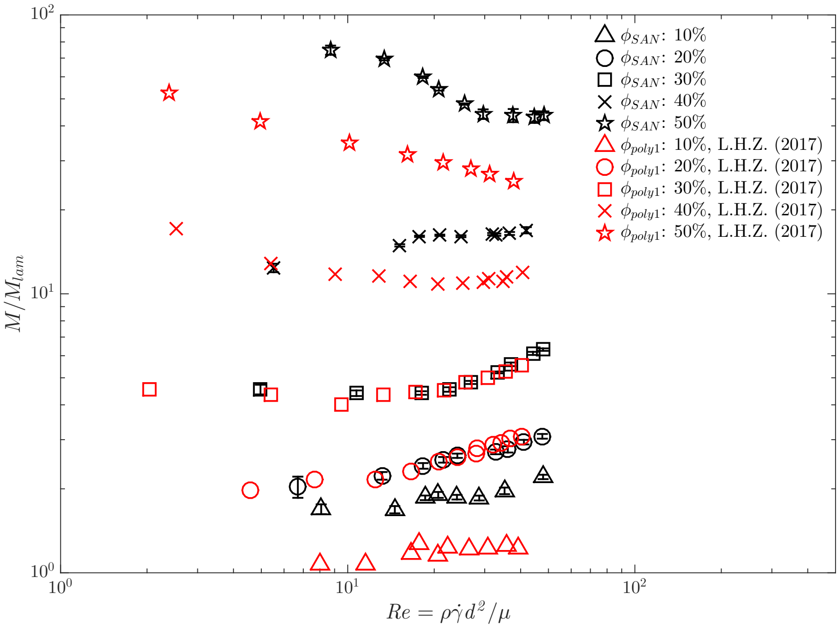

Figure 4.36: Direct torque measurements normalized by the laminar torque in terms of Re considering the present study and the results from Linares, Hunt, and Zenit (L.H.Z) (2017) for rough-walled experiments. The present study considers SAN particles in the fluid mixture of glycerol and ethanol. The L.H.Z study considers 3.34 mm polystyrene particles in the fluid mixture of glycerol and ethanol. $\rho_p/\rho_f = 1$.

Then the same normalized torques considering high-viscosity fluids are presented with respect to Re' in Figure 4.37. Though the results are plotted with respect to different Reynolds numbers, the comparisons of the experimental results are still similar between Figure 4.36 and Figure 4.37 due to similar particle sizes considered in each study (3.32 mm and 3.34 mm).

There are two types of differences between the Linares data and the current data observed in Figure 4.36 and Figure 4.37: the trend of shear thinning vs. shear thickening for $\phi = 40\%$, and the difference in effective viscosity magnitudes for $\phi = 10\%$, 40% and 50%. The different trends for $\phi = 40\%$ can be explained by the different shapes of the particles: the nearly spherical shape vs. the elliptical shape. At a solid fraction of 40%, particles almost fill the entire rheometer annulus with limited free space for particle migration. In this scenario, the nearly spherical shape allows

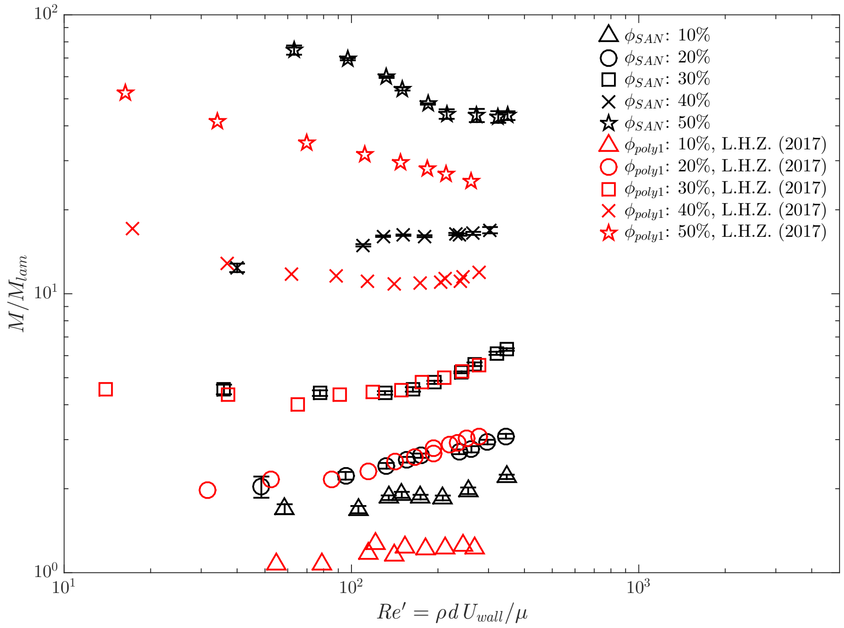

Figure 4.37: Direct torque measurements normalized by the laminar torque in terms of Re' considering the present study and the results from Linares, Hunt, and Zenit (L.H.Z) (2017) for rough-walled experiments. The present study considers SAN particles in the fluid mixture of glycerol and ethanol. The L.H.Z study considers 3.34 *mm* polystyrene particles in the fluid mixture of glycerol and ethanol. $\rho_p/\rho_f = 1$.

the SAN particles more flexibility to migrate vertically as compared to the elliptical polystyrene particles, and therefore contributes more to the torque measurements. While for the 50% solid fraction, the rheometer annulus has been completely filled up and the particles cannot move freely in the vertical direction regardless of the particle shape. For the magnitude differences observed in 10%, 40% and 50% solid fractions, the different particle packing structure, the temperature differences of the glycerol-ethanol mixture, and the corresponding glycerol-ethanol composition change in the mixture may have contributed to the differences. At the solid fraction of 10%, the temperature variation of liquid may affect the data processing accuracy. The Linares experiment and the current experiment were implemented at different physical locations in terms of laboratories, which have different room temperatures. As a result, to mix the 1050 kg/m^3 glycerol-ethanol mixture, Linares used 42% glycerol and 58% ethanol, while the current experiment uses 51% glycerol and 49% ethanol. Besides the room temperature difference, during the experiment, the temperature control is different even though both experiments have taken temperature and density measurements for each data point. Linares measurements have a temperature variation range of approximately 6 °C, with the highest temperature usually recorded at the maximum shear rates. With regard to the current data measurement, the temperature variation ranges are 20°C to 22.2°C and 20°C to 21.1°C for glycerol-water and glycerol-ethanol mixtures, separately. In addition, the glycerol-ethanol mixture density was deliberately controlled around 1050 kg/m^3 during the experiment. For glycerol-water mixture, the impact of fluid temperature variation is limited, with the density variation for glycerol-water mixture less than 0.2% over a liquid temperature variation range of 6°C. However, for the glycerol-ethanol mixture, the liquid density, the glycerol-ethanol composition, and the dynamic viscosity may vary significantly over the temperature range of 6°C. As a result, due to the different lab temperature environments and the challenge to control glycerol-ethanol mixture viscosity, there could be some data processing differences in the 10% solid fraction result of Linares, leading to the smaller Linares torque measurements observed in Figure 4.36 and Figure 4.37.

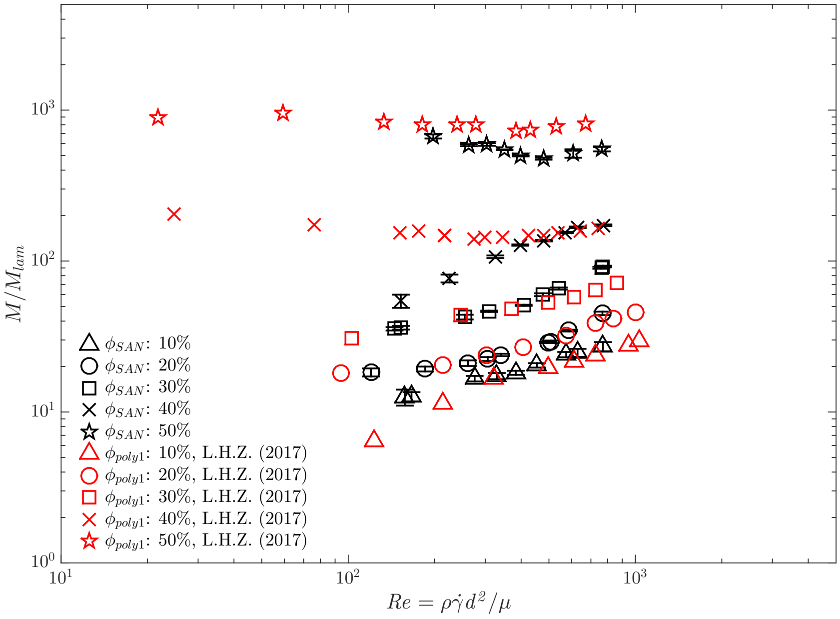

Figure 4.38: Direct torque measurements normalized by the laminar torque in terms of *Re* considering the present study and the results from Linares, Hunt, and Zenit (L.H.Z) (2017) for rough-walled experiments. The present study considers SAN particles in the fluid mixture of glycerol and water. The L.H.Z study considers 3.34 *mm* polystyrene particles in the fluid mixture of glycerol and water. $\rho_p/\rho_f = 1$.

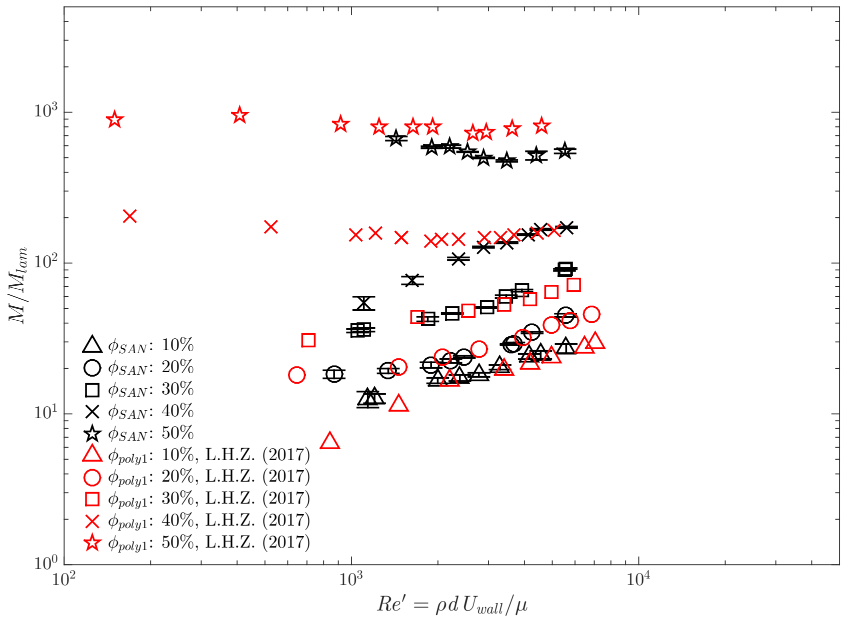

Figure 4.39: Direct torque measurements normalized by the laminar torque in terms of Re' considering the present study and the results from Linares, Hunt, and Zenit (L.H.Z) (2017) for rough-walled experiments. The present study considers SAN particles in the fluid mixture of glycerol and water. The L.H.Z study considers 3.34 *mm* polystyrene particles in the fluid mixture of glycerol and water. $\rho_p/\rho_f = 1$.

Figure 4.38 shows the SAN data immersed in low-viscosity fluid, along with the experimental measurements from Linares et al. (2017) using elliptical polystyrene (3.34 *mm*) for ϕ ranges from 10% to 50%. Both experiments use rough walls to shear the 1050 km/m^3 glycerol-water mixture. The loading particles differ in shape and effective diameter. The Linares results use elliptical polystyrene particles with an annulus gap width to particle diameter ratio of 7.46, which is 3.5% smaller as compared to the same ratio for SAN particles. For ϕ from 10% to 30%, the current experimental data compare well with the Linares data, as both effective viscosities increase with Reynolds number. For $\phi = 40\%$, the Linares data is relatively constant, while the current experimental data gradually increases around $Re = 152$ and finally matches with the Linares result around $Re = 770$. For $\phi = 50\%$, both experimental data show slight shear-thinning behaviors, with the current experimental results being approximately 32% smaller than the Linares results. Possible reasons for the difference at the 40% results could be that spherical particles are more easily to move freely in the vertical annulus direction as compared to the elliptical particles at ϕ = 40%; therefore, it leads to an increasing torque over the Reynolds number regime examined. While for the ϕ = 50% data, filled elliptical particles contribute more to the torque measurement as compared to the spherical particles due to the different particle packing structures.

Following that, Figure 4.39 presents the same normalized torques in terms of Re'. The current measurements still compare well with the Linares study for ϕ from 10% to 30%, but show slight differences at the 40% and 50% solid fraction states.

As shown in Figure 4.18, the SAN particles have augmented the turbulence effect and therefore increased the effective viscosity over the range of Re examined. This observation is similar to the experimental measurements of Gore and Crowe (1989) considering turbulent fluctuations of multiphase pipe flows, though for non-neutrally buoyant particles. Their results show that, for particle diameter larger than 10% of the turbulence length scale, the presence of the particles enhances the turbulent intensity. For the present study, one hypothesis is that, the relatively large SAN particles do not follow the motions of turbulent flows, and the induced particle relative motion may produce wakes that augment the flow turbulence.

In summary, the present experimental measurements in terms of normalized torques are in agreements with the results from Linares et al. (2017) for ϕ from 10% to 30% as functions of Re and Re'. The comparisons with the previous experimental measurements indicate the Reynolds number considering the maximum rotational velocity, Re', could be further used to examine the behaviors of liquid-solid flows in other experimental studies.

4.8 Comparison with simulation results

The normalized torque, which is equivalent to the effective viscosity, for the current experimental study and the numerical studies of the inertial suspensions are compared and discussed in this section. Specifically, the normalized torques of the current experiments and the effective viscosities from the simulations are compared with respect to the particle Reynolds number first. Then the same normalized results are examined using the Reynolds number (Re') to further validate the hypothesis of Re' proposed in Section 4.5.

Figure 4.40 shows on log scale the current experimental results considering polystyrene and SAN particles immersed in high-viscosity fluids, along with the numerical results from Rahmani et al. (2018) using neutrally-buoyant particles, for ϕ = 0.1, 0.2, and 0.3. The experimental setup is equivalent to rotating a layer of particles to

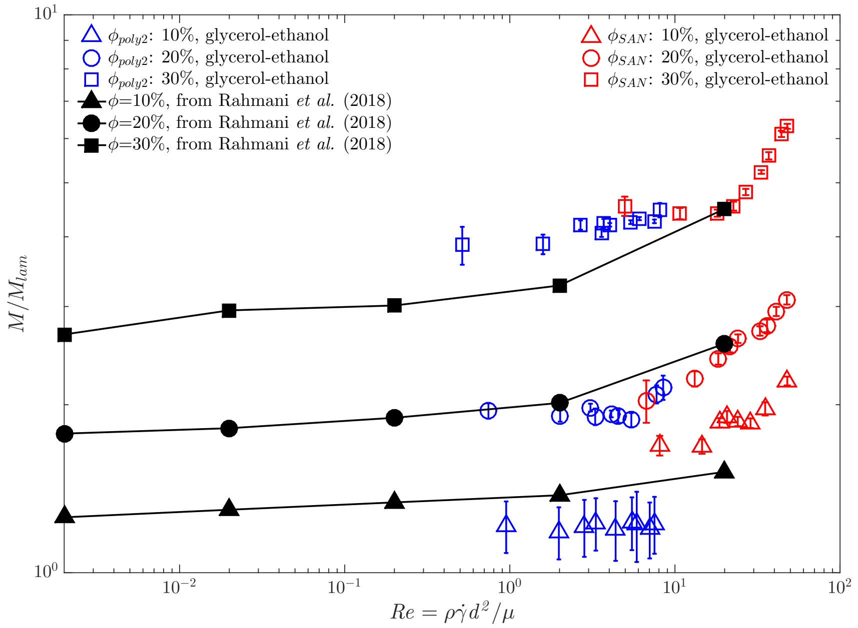

Figure 4.40: Normalized torque (experimental measurements) and effective viscosity (simulation results) in terms of Re considering neutrally buoyant suspensions. The experimental results consider polystyrene and SAN particles in the fluid mixture of glycerol and ethanol for 0.1, 0.2, and 0.3 solid fractions. The numerical results are from Rahmani et al. (2018).

generate the shear flow with spherical particles. However, for the simulation study from Rahmani et al. (2018), the flow is generated by the horizontal movements of two planes in the opposite directions, but with the same velocity magnitudes. For all solid fractions examined in Figure 4.40, the normalized torques for the present study show shear-thickening behaviors for Re from 2 to 20, which are consistent with the simulation results. For ϕ = 10%, the averaged experimental measurement for Re of approximately 2 is 14% smaller than the corresponding value from Rahmani et al. (2018), but the maximum experimental result at the same Re is only 5% smaller than the simulation result. At the same solid fraction of 10% for Re around 20, the experimental measurement is approximately 25% higher than the simulations. For ϕ = 20%, the experimental data at Re of 2 and 20 matches closely with the simulation results from Rahmani et al. (2018). For ϕ = 30%, the experimental measurement is approximately 18.6% larger than the values from Rahmani et al. (2018) at Re of 2, but the experimental measurement compares well with the numerical result for Re of 20. The slight mismatch between the experimental measurement and the simulation result may be caused by the difference of the particle shapes, since

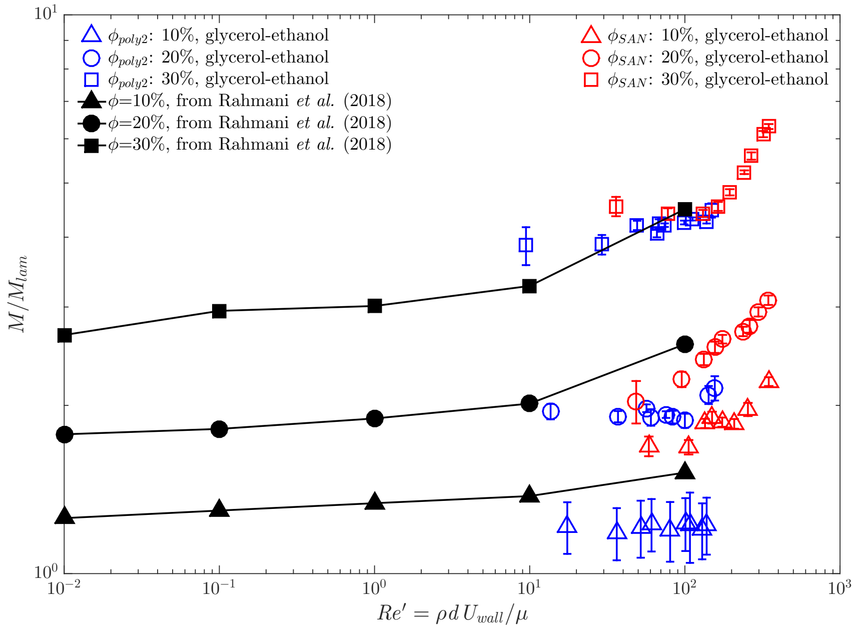

Figure 4.41: Normalized torque (experimental measurements) and effective viscosity (simulation results) in terms of Re' considering neutrally buoyant suspensions. The experimental results consider polystyrene and SAN particles in the fluid mixture of glycerol and ethanol for 0.1, 0.2, and 0.3 solid fractions. The numerical results are from Rahmani et al. (2018).

the experimental particles are not perfectly rigid spherical as the particle properties assumed in the simulation.

Then the same normalized torques and the effective viscosities are presented in terms of Re' in Figure 4.41. For the study of Rahmani et al. (2018), they considered a simple shear flow and used a gap (defined by the gap between $U = 0$ and $U = U_{max}$) to particle size (b/d) ratio of 5. The experimental results and the simulation results still compare well. At the 10% solid fraction state, the simulation result for Re' of 10 is slightly larger than the experimental result, but the simulation result for Re' of 100 is slightly smaller than the corresponding experimental measurement. The 20% and 30% simulation results for Re' of 10 and 100 show good agreements with the simulation results.

The same experimental results considering particles in the fluid mixture of glycerol and ethanol are compared with the simulation work from Picano et al. (2013) in Figure 4.42. The study of Picano et al. (2013) considers a plane Couette flow for neutrally-buoyant rigid spheres immersed in liquid, covering a particle Reynolds

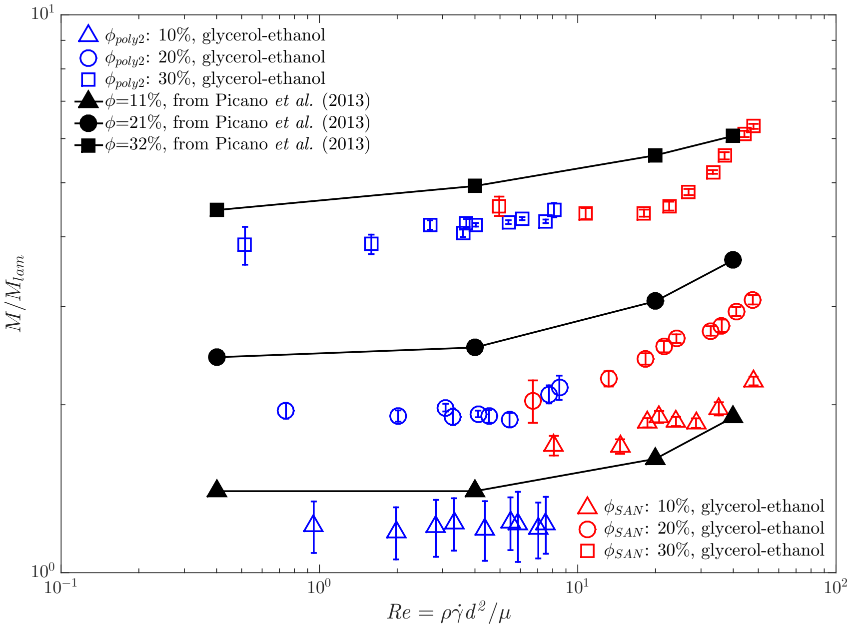

Figure 4.42: Normalized torque (experimental measurements) and effective viscosity (simulation results) in terms of Re considering neutrally buoyant suspensions. The experimental results consider polystyrene and SAN particles in the fluid mixture of glycerol and ethanol for 0.1, 0.2, and 0.3 solid fractions. The numerical results are from Picano et al. (2013).

number regime from 0.4 to 40, which is similar to the Re examined in the experimental study. At the 10% solid fraction state, the current measurement is 15% lower than the numerical study at Re of 4, but the experimental measurements for Re of approximately 20 and 40 compare well with the simulation data points. For $\phi = 0.2$, all current measurements are slightly smaller than the simulations, with a maximum deviation of 24% in terms of normalized torque values for Re around 4. In the examination of $\phi = 30\%$, the current results show good agreements with the values calculated by Picano et al. (2013) for Re of 4 and 40, but is 19% smaller in comparison with the simulation value at Re of 20. The experimental study shows a relatively stronger dependence of normalized torque on Re as compared to the simulation at the state of 30% solid fraction. Possible explanations are that the roughened walls reduce the particle slips near the inner testing cylinder for the current experimental setup.

Then the same normalized torques and the effective viscosities are compared in terms of Re' in Figure 4.43. The gap to particle size ratio (b/d) is 2.5 for the

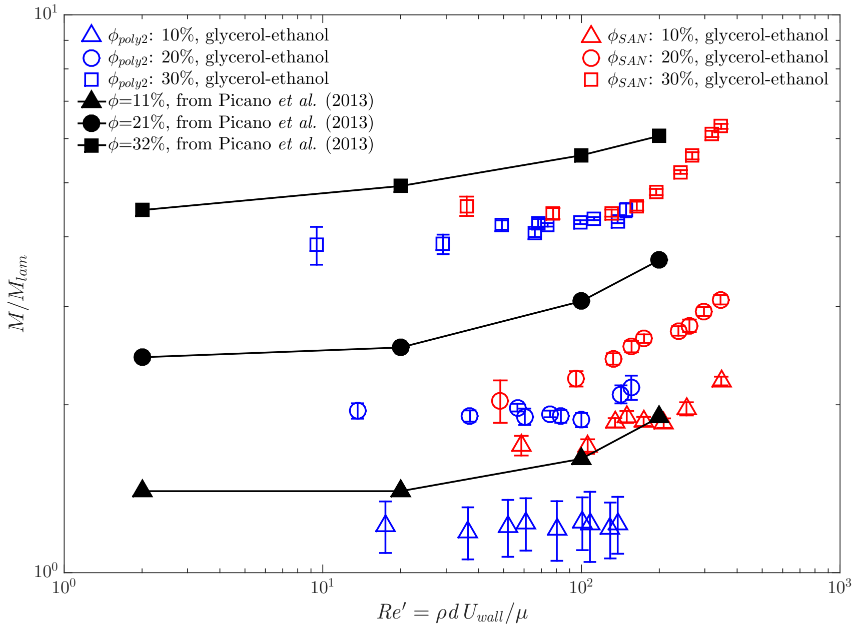

Figure 4.43: Normalized torque (experimental measurements) and effective viscosity (simulation results) in terms of Re' considering neutrally buoyant suspensions. The experimental results consider polystyrene and SAN particles in the fluid mixture of glycerol and ethanol for 0.1, 0.2, and 0.3 solid fractions. The numerical results are from Picano et al. (2013).

numerical study. The simulation results are higher than the experimental results over the similar Re' regions. The small b/d size in the simulation study of Picano et al. (2013) may have contributed to the difference in normalized torques.

The same numerical work from Picano et al. (2013) and the experimental measurements before the laminar-turbulent transition are also compared for effective viscosity in terms of solid fraction in Figure 4.44. The Eilers correlation ($\mu'/\mu = [1 + a\phi/(1 - \phi/\phi_m)]^2$ using $a = 1.5$, and $\phi_m = 0.58$) and the Krieger-Dougherty relationship ($\mu'/\mu = (1 - \phi/\phi_m)^{-a}$ using $a = 1.82$, and $\phi_m = 0.68$) are also plotted along the experimental and simulation results. The numerical results from Picano et al. (2013) have slightly larger solid fractions (11%, 21%, and 32%) at each state as compared to the experimental results, and the presence of more solid volume fraction has contributed to the relatively larger normalized torques from simulations observed in Figure 4.42. The Krieger-Dougherty relation compares well with the current measurements and the simulations from Picano et al. (2013) for Re from 0.4 to 8 at the ϕ = 10% and ϕ = 20% states. However, for ϕ = 30%,

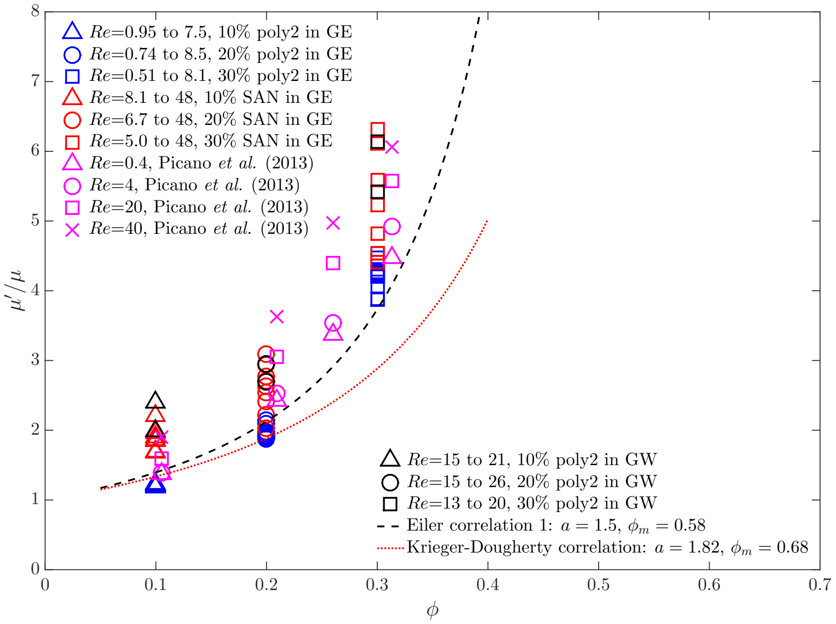

Figure 4.44: Effective viscosity of liquid-solid flows in terms of solid fraction from numerical studies of Picano et al. (2013) and experimental results with Reynolds numbers less than the critical Re_b. The red and the black lines correspond to the Krieger-Dougherty relation and the Eilers relation, respectively.

over the same particle Reynolds number examined, both the experimental and the simulation results deviate from the Krieger-Dougherty correlation, but match the Eilers relationship.

Figure 4.45 shows the comparison between the current measurements immersed in the glycerol-ethanol mixture and the simulation results from Kulkarni and Morris (2008). For the state of 10% solid fraction, the present experimental measurements are slightly smaller than the simulations at Re of 4 and 8, but are 13% higher than the simulation value for Re of 16. For $\phi = 20\%$, the current measurements show slightly smaller normalized torques, but still compare well with the numerical studies. For $\phi = 0.3$, the present normalized torque show good agreement with the result of Kulkarni and Morris (2008) for Re of 4, but are 8.4% and 16.1% smaller than the simulation data at Re of 8 and 16, respectively. There are different mechanisms of particle movements for the experimental and simulation works. In the study of Kulkarni and Morris (2008), the particles move closer to the walls and show higher concentrations near the wall. However, in the current experiments, due to the design of the outer-rotating cylinder, the particles tend to move away from the inner testing

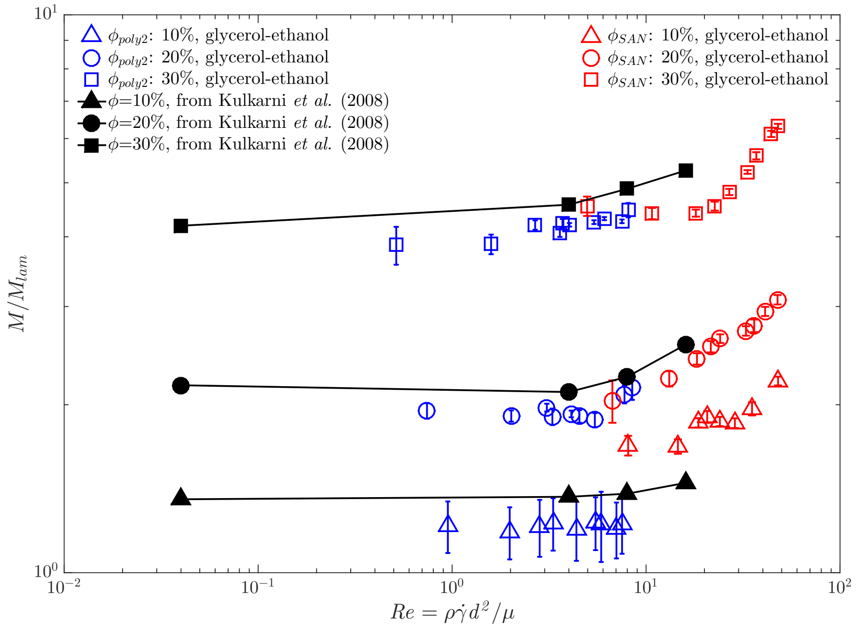

Figure 4.45: Normalized torque (experimental measurements) and effective viscosity (simulation results) in terms of Re considering neutrally buoyant suspensions. The experimental results consider polystyrene and SAN particles in the fluid mixture of glycerol and ethanol for 0.1, 0.2, and 0.3 solid fractions. The numerical results are from Kulkarni and Morris (2008)

cylinder, where the torque is measured. The different concentration mechanisms of particles may have some effects on the effective volume fractions in the liquid-solid mixture, and lead to the effective viscosity differences between the experimental and simulation work.

The same normalized torques from experiments and the effective viscosities from simulations are presented in Figure 4.46. The simulation results show the same shear-thickening behaviors as compared to the experimental results, but tend to be slightly larger in terms of magnitude.

Figure 4.47 presents the same comparison between the present study considering measurements before the laminar-turbulent transition and the simulation work from Kulkarni and Morris (2008), but for effective viscosity in terms of solid fraction. Two Krieger-Dougherty correlations with $\phi_m = 0.58$ and $\phi_m = 0.68$ are also plotted along with the results. The experimental and simulation results of 10% and 20% solid fractions considering Re from 0.5 to 8 are best fitted with the Krieger-Dougherty relation with $\phi_m = 0.68$. However, the 30% result, also in the Re regime from 0.5 to

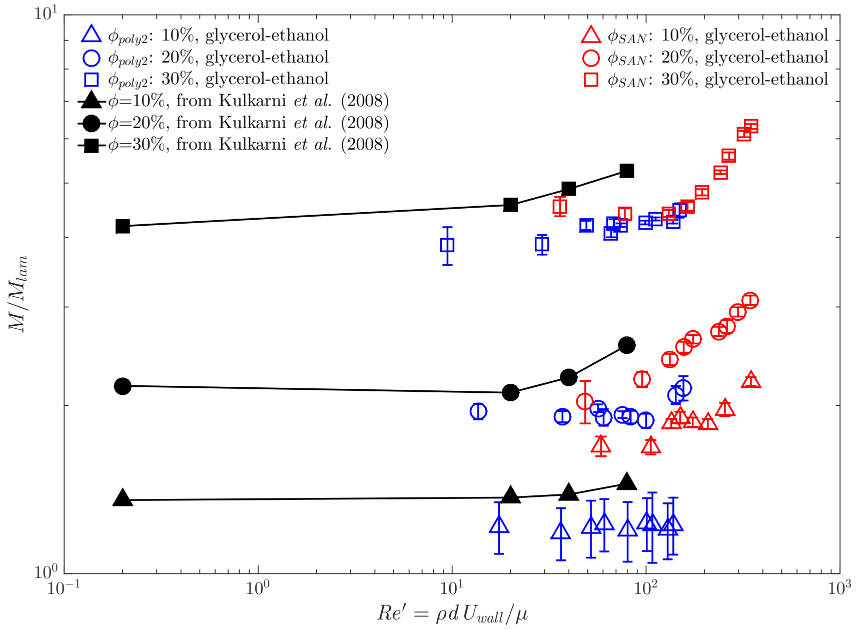

Figure 4.46: Normalized torque (experimental measurements) and effective viscosity (simulation results) in terms of Re' considering neutrally buoyant suspensions. The experimental results consider polystyrene and SAN particles in the fluid mixture of glycerol and ethanol for 0.1, 0.2, and 0.3 solid fractions. The numerical results are from Kulkarni and Morris (2008)

8, deviates from the fitting using $\phi_m = 0.68$, and matches better with the correlation using $\phi_m = 0.58$.

In summary, the current experimental results have shown that the normalized torques of the current experiments and the effective viscosities of the simulations compare well over the similar Re and Re' regimes. The comparison between the experiments and simulations shows that Re' has the potential for further investigation of liquid-solid flows with intermediate Reynolds numbers. In addition, the comparison shows that the effective viscosities from the simulations are larger than the normalized torques of experiments for the cases of 20% and 30% solid fractions. Possible reasons for the difference include the surface roughness, the gap to particle size ratios (b/d), and the numerical assumptions for Reynolds and collisional stresses. The limitation of the comparison is that the simulations presented in this section consider b/d ratios of 2.5 and 5. Comparisons with future simulations considering various b/d ratios and similar particle Reynolds numbers should be conducted to examine the applications of Re'.

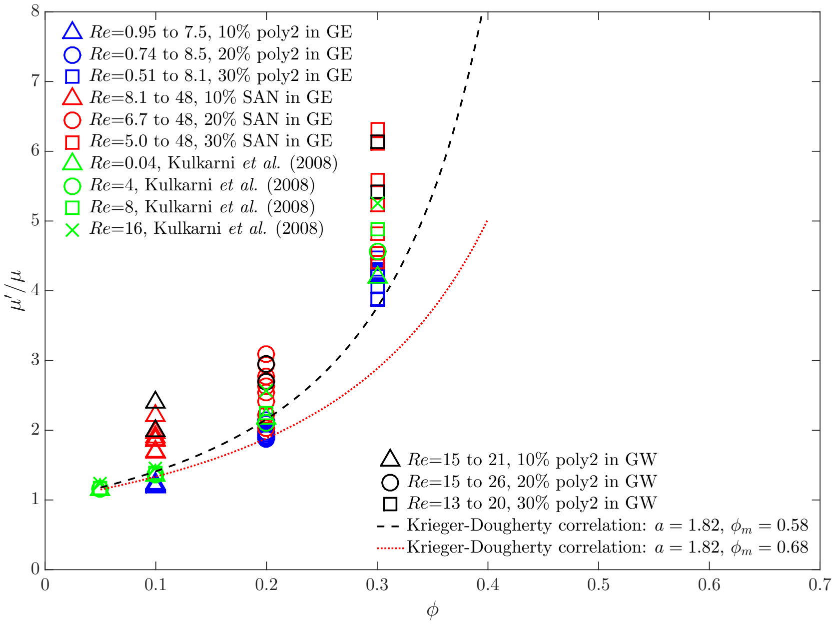

Figure 4.47: Effective viscosity of liquid-solid flows in terms of ϕ from simulation studies of Kulkarni and Morris (2008) and experimental results with Reynolds numbers less than the critical Re_b. The red and the black lines correspond to the Krieger-Dougherty relations with ϕ_m of 0.68 and 0.58.

4.9 Summary

This section presents the direct torques and the normalized torques of the rheological measurements for neutrally-buoyant particles. For liquid-solid flows with matched particle and fluid densities and solid fractions from 10% to 30%, the effective viscosity of the particulate flows only depends on ϕ until we observe the shear-thickening behaviors for Re of approximately 10. For the intermediate particle Reynolds number region from 10 to 100 and ϕ less than 40%, the effective viscosity of the liquid-solid flows not only depends on the solid fraction, but also shows increased dependence on the particle Reynolds number. For Reynolds number greater than 100, the suspensions transition to the turbulent flows, similar to what we observe for the pure fluids. The measurements before and after the laminar-turbulent transition are examined as functions of Re, Re_b, Re_b' and G'. The results show that the small polystyrene particles have suppressed the transition to turbulence while the larger SAN particles have augmented the turbulent transition. At the 40% and 50% solid fraction states, the measurements can be better analyzed by $(M - M_o)$ instead of M. The ratio of $(M - M_o)/M_{lam}$ increases with Re at the state of 40%

solid fraction, but is nearly independent of Re for $\phi = 50\%$.

Most importantly, by comparing the current experimental measurements as functions of Re and Re', the present normalized torque results match better when plotting with Re' rather than Re. Rheological model considering M/M_{lam} vs. Re' for 10%, 20%, and 30% solid fractions, as well as models concerning $(M - M_o)/M_{lam}$ vs. Re' for 40% and 50% solid fractions are proposed. With the observation of current experimental measurements with respect to Re', this chapter further uses Re' to re-examine the previous experimental and simulation studies, and the current results still compare well with the experimental and numerical results using Re'.

Chapter 5

RHEOLOGICAL MEASUREMENTS OF NON-NEUTRALLY BUOYANT SUSPENSIONS

5.1 Motivation

Besides all the experiments considering neutrally-buoyant particles presented in Chapter 4, particles that are denser than the suspending fluids were sheared in the Caltech Couette flow device to investigate the impact of additional solid-phase inertia on the particulate flow torque measurement.

As discussed in Table 1.2 of Section 1.5, there are previous experimental measurements considering settling particles (Hanes and Inman, 1985; Prasad and Kytömaa, 1995; Linares, 2015). However, there are limited experimental data points in the moderate Stokes number regime from 5 to 20. Therefore, a map similar to Figure 1.1 considering liquid-solid flows in which $\rho_p/\rho_f > 1$ for moderate Stokes numbers is largely unfilled.

To extend the measurements of Stokes number to the previously untested range, experiments considering the 3.22 mm SAN particles and the 1.27 mm polystyrene particles immersed in water were performed. Unlike the neutrally-buoyant experiments with a homogenous particle distribution throughout the suspending liquid, due to the particle-fluid density difference, the particles settle at the bottom of the annulus at the static state, forming a settled particle bed. Under the static condition, for low particle loading fractions of 0.1 and 0.2, particles do not reach the middle testing cylinder where torque measurements were implemented (Figure 2.1). Once the outer cylinder is sheared, settled particles fluidize with water, and gradually enter the middle testing cylinder region and the top cylinder region, leading to a gradient of particle concentration along the vertical direction based on the rheometer rotational speed. The effective solid fraction in the middle testing cylinder range is different from the overall particle volume fraction. Therefore, during these experiments, the liquid-solid mixtures are assumed to be heterogeneous, but the torque is only measured at the middle testing cylinder region ($h_{middle} \leqslant h \leqslant h_{top}$). For these reasons, the term of the loading fraction ($\overline{\phi}$) instead of the solid fraction (ϕ) is used to describe the filling state of experiments considering non-neutrally buoyant suspensions. Due to the different packing structures of polystyrene and SAN particles, the polystyrene and SAN beds have different bed heights (h_o) at static states considering the same loading fraction ($\overline{\phi}$). For example, at the state of $\overline{\phi}$ = 30%, both bed heights of polystyrene and SAN particles are greater than the height of the middle testing section ($h_o > h_{middle}$). The bed height of polystyrene particles is slightly greater than the height of the SAN particle bed (h_o(polystyrene, $\overline{\phi}$ = 30%) > h_o(SAN, $\overline{\phi}$ = 30%)), leading to more contact surface between the polystyrene particle bed and the middle testing cylinder than the SAN particle bed for $\dot{\gamma}$ =0. As the $\dot{\gamma}$ increases, based on the visualization results in the Caltech thesis of Linares (2015), the different h_o values also affect the distribution of effective solid fractions along the axial direction for polystyrene and SAN particles during bed expansion.

In this chapter, the liquid-solid flows were tested with the additional inertial effects of the non-neutrally buoyant particles. In Section 5.2, the experimental results of 1.27 *mm* polystyrene particles in water is discussed in detail first. Then the direct torque measurement and the normalized torque results for 3.22 *mm* SAN particles are presented in Section 5.3. Following that, the results considering the two different particles are compared as functions of St and St' ($St' = \rho_p d U_{wall}/9\mu$) in Section 5.4. Finally, the current non-neutrally buoyant results are compared with the previous experimental studies in Section 5.5.

5.2 Rheological experiments of non-neutrally buoyant polystyrene particles

For non-neutrally buoyant mixtures of polystyrene particles in water ($\rho_p/\rho_f = 1.05$), the middle testing cylinder is used to measure the torque generated by the liquid-solid flow, with similar procedures implemented in the neutrally-buoyant experiments. This section covers the non-neutrally buoyant torque measurements of 1.27 *mm* polystyrene particles immersed in water. The torque measurements cover a Stokes number regime from 3.3 to 27.

As shown in Section 2.3, the polystyrene particles have approximately 2.5 times smaller particle diameter as compared to the SAN particles, leading to different b/d ratios (19.61 vs. 7.73). In addition, there are differences in the particle shape (spherical vs. nearly spherical) and the particle surface roughness.

In Figure 5.1, it shows the direct torque measurements of polystyrene particles immersed in water for 10% and 20% loading fractions. As shown by the cubic curves, the 10% and the 20% measurements increase non-linearly as the shear rate increases. At the zero rotational speed, the torque of the 10% loading fraction is approximately zero, indicating that the 10% settled polystyrene bed has not reached

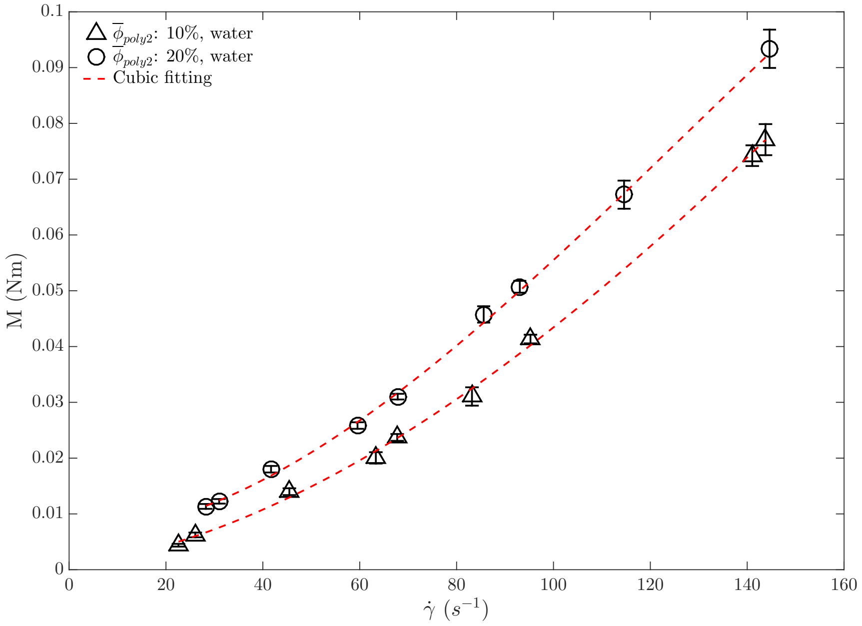

Figure 5.1: Direct torque measurement in terms of $\dot{\gamma}$ for $\overline{\phi} = 0.1$ and 0.2 considering polystyrene particles in water. $\rho_p/\rho_f = 1.05$. The cubic fitting curves are $M = -5.1 \times 10^{-9}\dot{\gamma}^3 + 3.6 \times 10^{-6}\dot{\gamma}^2 + 1.2 \times 10^{-4}\dot{\gamma} + 5.4 \times 10^{-4}$ and $M = -1.7 \times 10^{-8}\dot{\gamma}^3 + 6.5 \times 10^{-6}\dot{\gamma}^2 + 1.2 \times 10^{-5}\dot{\gamma} + 6.3 \times 10^{-3}$ for $\overline{\phi}$ of 10% and 20%.

the middle testing cylinder ($h_o < h_{middle}$). As the rheometer rotates, the settled particles enter the middle testing region, leading to the exponential increase of the torque measurements of the 10% and 20% loading fraction polystyrene particles.

Figure 5.2 and Figure 5.3 show the direct torque measurements with respect to shear rates considering polystyrene particles in water for the 30% and the 40% loading fractions. Both torque measurements show similar trends, but the 40% loading fraction results have higher magnitudes. The settled beds of the 30% and 40% polystyrene particles have reached the middle testing cylinder ($h_o > h_{middle}$), but have not reached the top cylinder region ($h_o < h_{top}$). As a result, polystyrene particles are fluidized and more particles enter the middle testing region ($h_{middle} < h < h_{top}$) at low shear rates. As $\dot{\gamma}$ further increases, particles further migrate to the top cylinder regions ($h > h_{top}$). Both measurements are best fitted using cubic fitting curves. With linear fitting curves, the M_o for the 30% and 40% loading fractions are estimated to be 0.090 Nm and 0.59 Nm, which are approximately 20 times larger than the M_o values of the 30% and 40% solid fraction neutrally-buoyant polystyrene particles in the fluid mixture of glycerol and ethanol as shown in Figure

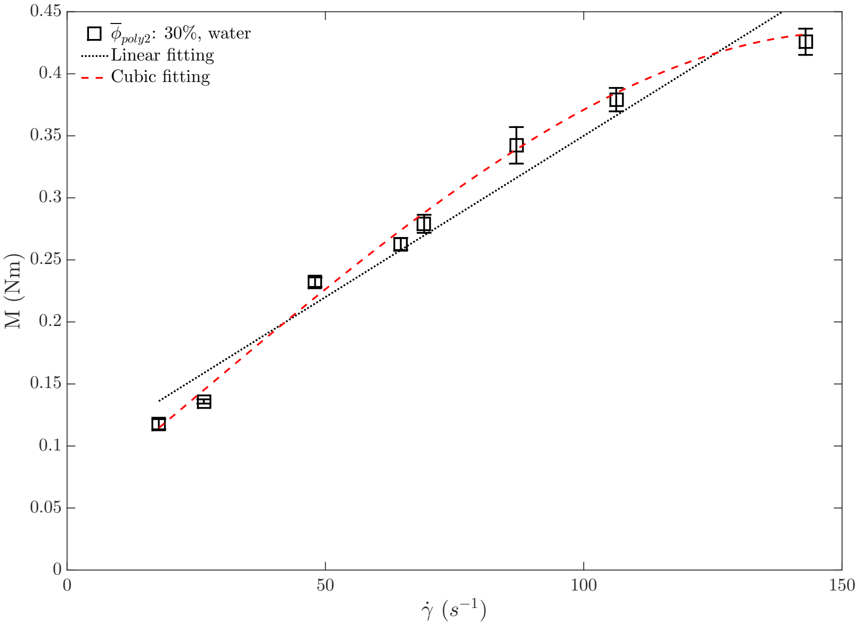

Figure 5.2: Direct torque measurement in terms of $\dot{\gamma}$ for $\overline{\phi} = 0.3$ considering polystyrene particles in water. The linear and the cubic fitting curves are $M = 2.6\times10^{-3}\dot{\gamma}+0.090$ and $M = -7.1\times10^{-8}\dot{\gamma}^3+4.9\times10^{-6}\dot{\gamma}^2+3.4\times10^{-3}\dot{\gamma}+5.3\times10^{-2}$.

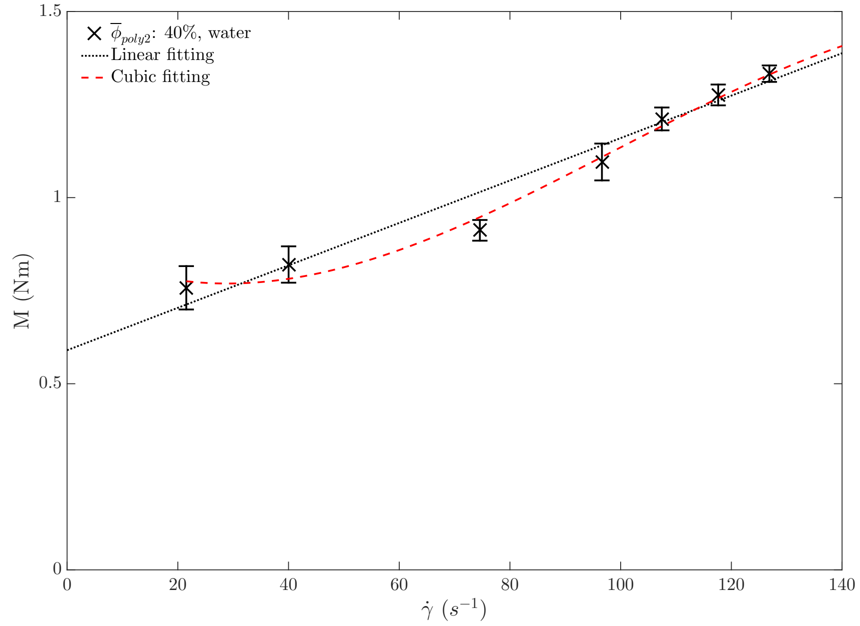

Figure 5.3: Direct torque measurement in terms of $\dot{\gamma}$ for $\overline{\phi} = 0.4$ considering polystyrene particles in water. The linear and the cubic fitting curves are $M = 5.7\times10^{-3}\dot{\gamma}+0.59$ and $M = -5.2\times10^{-7}\dot{\gamma}^3+1.5\times10^{-4}\dot{\gamma}^2-7.6\times10^{-3}\dot{\gamma}+0.87$.

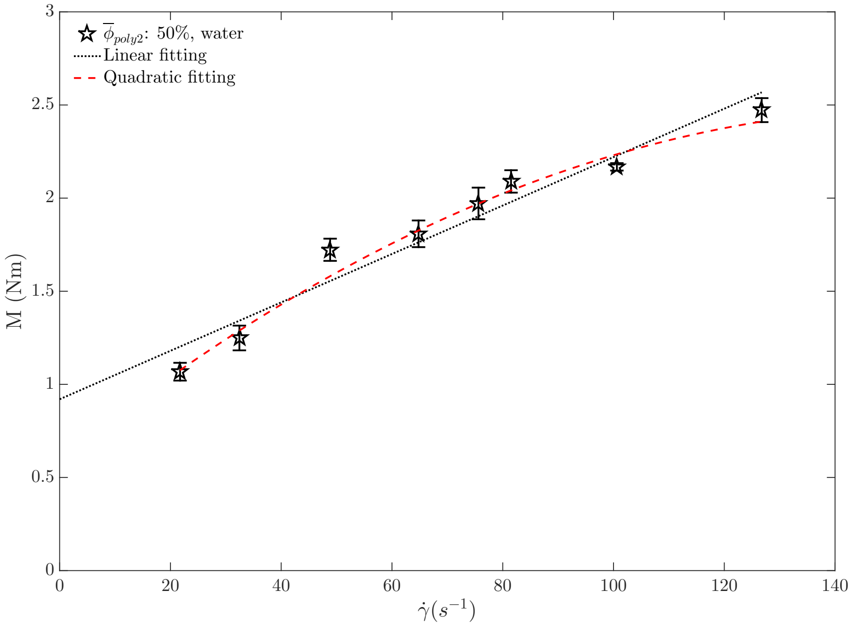

Figure 5.4: Direct torque measurement in terms of $\dot{\gamma}$ for $\overline{\phi} = 0.5$ considering polystyrene particles in water. The linear and the cubic fitting curves are $M = 1.3 \times 10^{-2}\dot{\gamma} + 0.92$ and $M = -7.6 \times 10^{-5}\dot{\gamma}^2 + 2.4 \times 10^{-2}\dot{\gamma} + 0.59$.

4.1 and Figure 4.2. The corresponding yield stresses for M_o values of 0.090 Nm and 0.59 Nm are 4.8 N/m^2 and 31.8 N/m^2, respectively.

Finally, Figure 5.4 presents the 50% loading fraction torque measurement with respect to the shear rate for polystyrene particles immersed in water. The torque increases with a decreasing slope as the rotational speed increases, and the data points are best fitted with the quadratic fitting curve. This can be explained by the decreasing effective solid fraction in the middle testing regions as more particles migrate vertically to the top cylinder area ($h > h_{top}$) due to the increasing shear rate at the 50% loading fraction state. Based on the linear fitting curve, M_o is calculated to be 0.92 Nm, which is approximately 3 times larger than the M_o value of the 50% solid fraction neutrally-buoyant polystyrene particles immersed in the fluid mixture of glycerol and ethanol as shown in Figure 4.2. The corresponding yield stress is 49.6 N/m^2.

Figure 5.5 presents the normalized torque in terms of Re_b for non-neutrally buoyant polystyrene particles in water. Figure 5.6 shows the same results of normalized torques, but the results are presented with respect to Stokes number from 3.3 to 27. Using the gap Reynolds number, the current rheological measurements are beyond

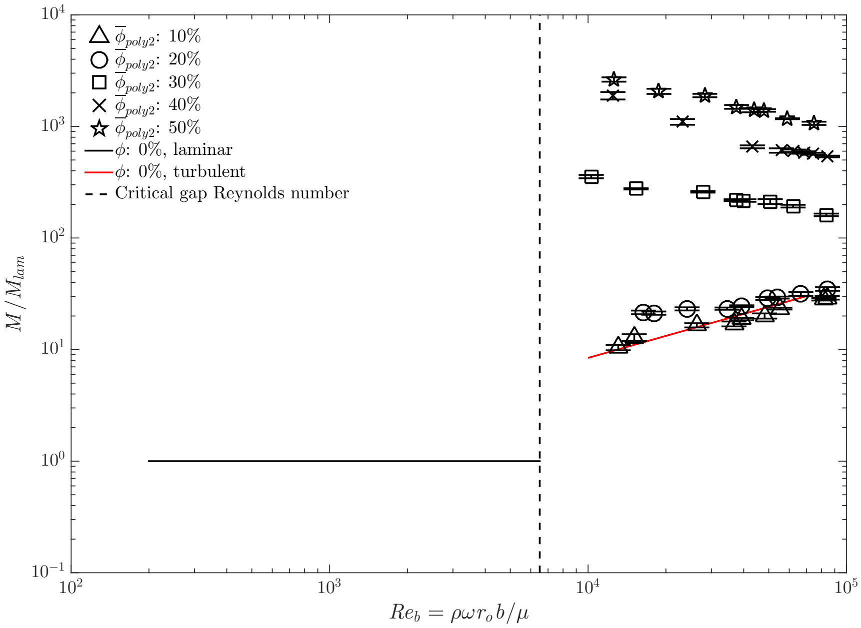

Figure 5.5: Direct torque measurement normalized by the laminar torque in terms of gap Reynolds number. The experiment considers 1.27 *mm* polystyrene particles in water. $\rho_p/\rho_f = 1.05$.

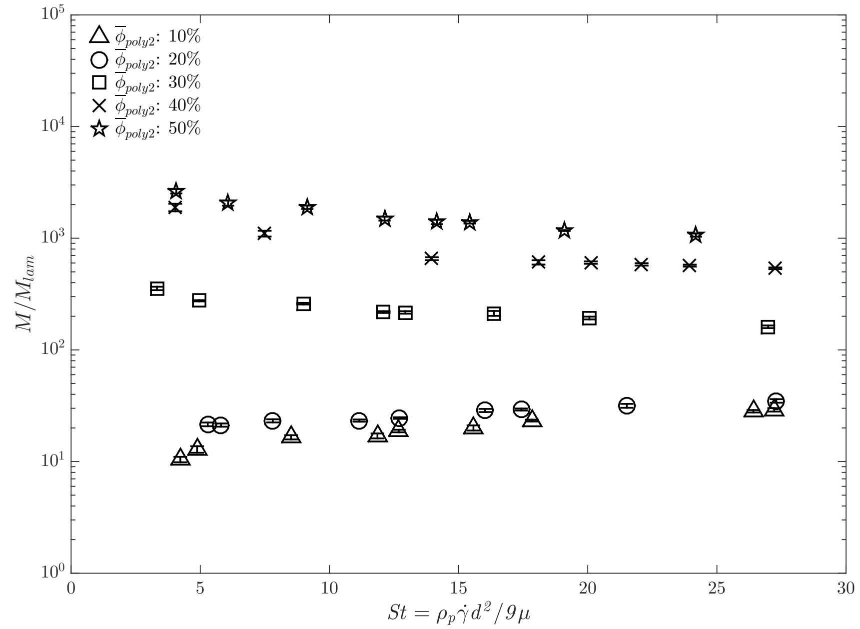

Figure 5.6: Direct torque measurement normalized by the laminar torque in terms of St. The experiment considers 1.27 *mm* polystyrene particles in water. $\rho_p/\rho_f = 1.05$.

the critical Reynolds number for pure fluids, and the non-neutrally measurements are in the turbulent regime. As shown in Figure 5.5, both the 0.1 and 0.2 loading fraction normalized torques increase as the Stoke number increases. For loading fraction of 10% and Re_b from 1.3×10^4 to 2.6×10^4, the normalized torque of the liquid-solid flow matches closely with the turbulent pure fluid fitting curve. This observation is consistent with the assumption that there are limited particles presented in the middle testing section near the lowest shear rates, leading to measurement results similar to pure fluids. For Re_b from 3.7×10^4 to 8.4×10^4, the measurements of the 10% loading fraction lie below the fitting curve corresponding to the pure fluids suggesting the presence of small polystyrene particles in the middle section has delayed the laminar-turbulent transition. For $\overline{\phi} = 30\%$, 40%, and 50%, the normalized torques of the suspensions decrease with increasing shear rates. As the resuspension mechanism explained in Section 5.1 for loading fractions $\geq 30\%$, during the bed expansion process, the increasing shear rate causes the initially settled particles to migrate to the top cylinder regions ($h > h_{top}$), leading to a continuous decrease of effective solid fraction until the effective solid fraction reaches a steady value at the highest shear rate.

5.3 Rheological experiments of non-neutrally buoyant SAN particles

This section presents the torque measurements of 3.22 mm SAN particles immersed in water, covering a Stokes number (St) region from 19 to 159.

Figure 5.7 presents the direct torque measurements considering SAN particles immersed in water for loading fractions of 0.1 and 0.2. The measured torques show exponential correlation with respect to the shear rates, and are best fitted with cubic curves. As $\dot{\gamma}$ increases, both the direct torque measurements increase exponentially. The fitting curve of the 10% solid fraction result is expected to pass through the origin of the coordinate system. This can be explained by the settling particle bed height ($h_o < h_{middle}$) and the design of the rheometer as shown in Figure 2.1. At the static state of 10% loading fraction, the settled particles cannot reach the middle test region for torque measurements. As the rheometer starts to rotate, settled particles mix with the water and gradually enter the middle test section ($h > h_{middle}$), leading to an exponential increase in torque measurements.

Figure 5.8 shows the direct torque measurements in terms of shear rate for SAN particles immersed in water considering 30% loading fraction. Like the corresponding polystyrene particle results presented in Figure 5.2, the 30% loading fraction mea-

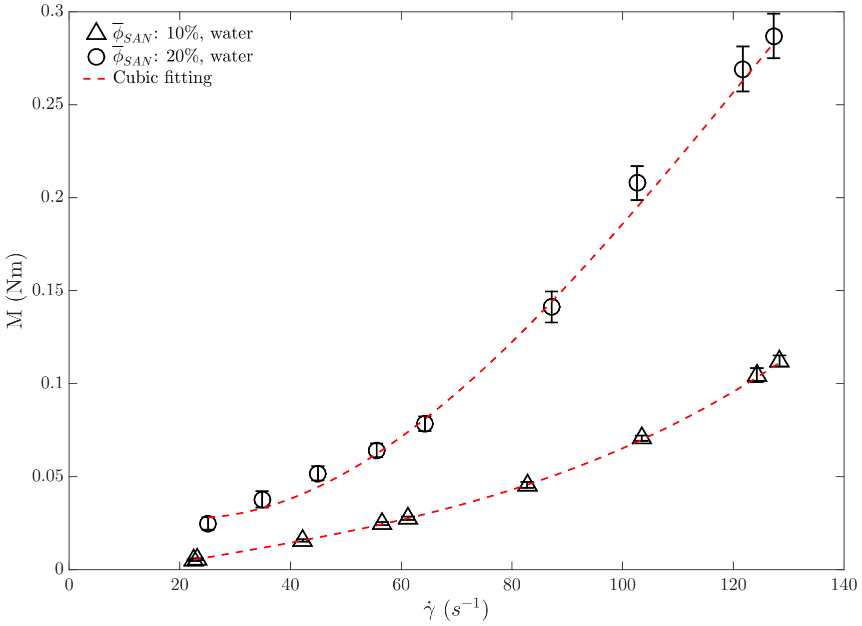

Figure 5.7: Direct torque measurement in terms of $\dot{\gamma}$ for $\overline{\phi} = 0.1$ and 0.2 considering SAN particles in water. $\rho_p/\rho_f = 1.05$. The cubic fitting curves are $M = 4.4 \times 10^{-8}\dot{\gamma}^3 - 3 \times 10^{-6}\dot{\gamma}^2 + 5.8 \times 10^{-4}\dot{\gamma} - 6.7 \times 10^{-3}$ and $M = -1.1 \times 10^{-7}\dot{\gamma}^3 + 4.2 \times 10^{-5}\dot{\gamma}^2 - 1.7 \times 10^{-3}\dot{\gamma} + 4.6 \times 10^{-2}$ for 10% and 20% loading fractions, respectively.

surements increase with a decreasing slope until shear rate around 60 s^{-1}, followed by an increase with relatively steady slope for shear rate from approximately 60 s^{-1} to 80 s^{-1}. The torque measurement shows stronger shear-thickening behaviors near the maximum shear rate of approximately 130 s^{-1}. Similar torque measurement results are also observed for 40% loading fraction of SAN particles immersed in water as shown in Figure 5.9, but with higher magnitudes of torques as compared to the 30% loading fraction results. At the 30% and 40% loading fractions, the settled beds of 30% and 40% SAN particles have reached the middle testing section under the stationary condition ($h_o > h_{middle}$), but have not reached the top cylinder ($h_o < h_{top}$) regions yet (Figure 2.1). This is consistent with the yield stresses observed for the 30% and the 40% loading fractions, which are caused by the presence of the settled beds in the middle test region at zero rotational speed. Based on the linear fitting curve, M_o are 0.27 Nm and 0.67 Nm, which are approximately 20 times greater than the the M_o values of the 30% and 40% solid fraction neutrally-buoyant SAN particles immersed in glycerol-ethanol mixture as shown in Figure 4.5 and Figure 4.6. The M_o values of 0.27 Nm and 0.67 Nm considering SAN particles

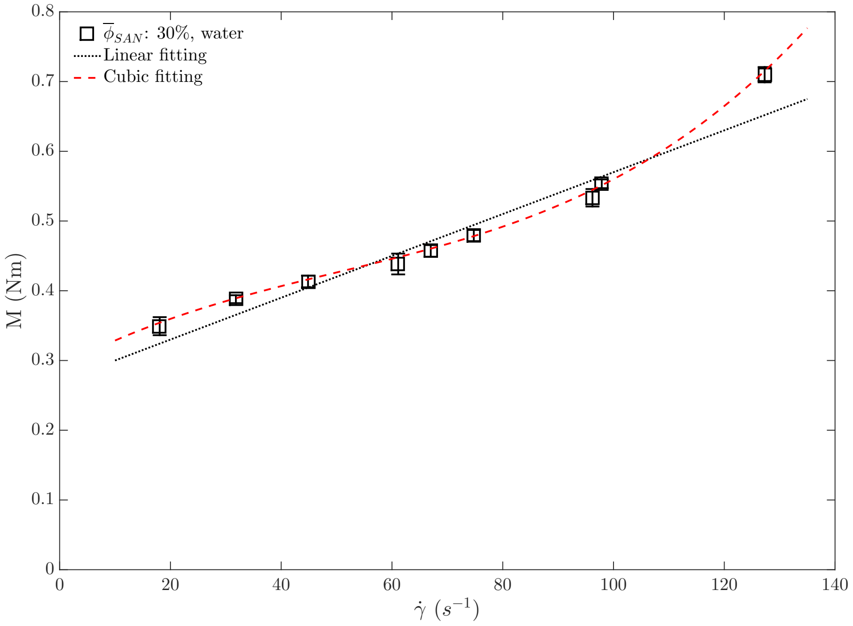

Figure 5.8: Direct torque measurement in terms of $\dot{\gamma}$ for $\overline{\phi} = 0.3$ considering SAN particles in water. $\rho_p/\rho_f = 1.05$. The linear fitting curve is $M = 3 \times 10^{-3}\dot{\gamma} + 0.27$. The cubic fitting curve is $M = 3.1 \times 10^{-7}\dot{\gamma}^3 - 4.7 \times 10^{-5}\dot{\gamma}^2 + 4.3 \times 10^{-3}\dot{\gamma} + 0.29$.

immersed in water are slightly larger than the M_o values of the 30% and 40% loading fraction polystyrene particles immersed in water as shown in Figure 5.2 and Figure 5.3. The corresponding yield stresses for the M_o values of 0.27 Nm and 0.67 Nm are 14.5 N/m^2 and 36.1 N/m^2 for 30% and 40% loading fractions, respectively.

Figure 5.10 shows the direct torque measurement of SAN particles with a loading fraction of 50% immersed in water, along with the quadratic fitting curve. Similar to the behavior of the 50% loading fraction polystyrene particles as shown in Figure 5.4, with an increasing shear rate, the torque measurements increase with a decreasing slope. At the 50% loading fraction static state, the settled bed has reached the top cylinder region ($h_o > h_{top}$). Once the outer cylinder starts to shear, suspended particles initially settled in the middle testing region enter the top cylinder area ($h > h_{top}$), leading to a decreasing effective particle solid fraction in the middle testing section. The M_o is estimated to be 1.6 Nm, which is approximately 3 times larger than the M_o value of the 50% solid fraction neutrally-buoyant SAN particles immersed in glycerol-ethanol mixture as shown in Figure 4.6, and is approximately 1.5 times larger than the M_o value considering 50% loading fraction polystyrene particles immersed in water as shown in Figure 5.4. The corresponding yield stress

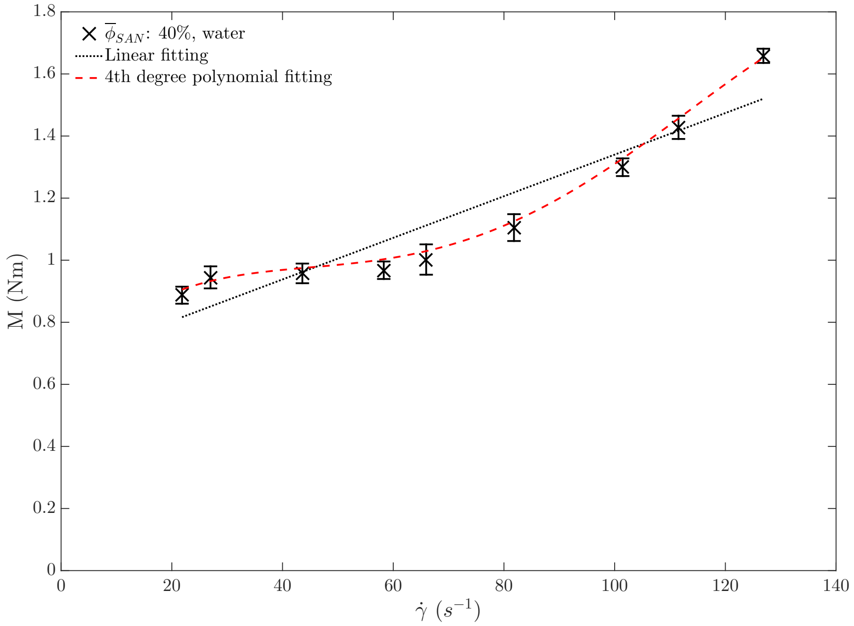

Figure 5.9: Direct torque measurement in terms of $\dot{\gamma}$ for $\overline{\phi} = 0.4$ considering SAN particles in water. $\rho_p/\rho_f = 1.05$. The linear fitting curve is $M = 6.7 \times 10^{-3}\dot{\gamma} + 0.67$. The polynomial fitting curve is $M = -1.8 \times 10^{-8}\dot{\gamma}^4 + 5.7 \times 10^{-6}\dot{\gamma}^3 - 5.5 \times 10^{-4}\dot{\gamma}^2 + 2.3 \times 10^{-2}\dot{\gamma} + 0.61$.

is 86.3 N/m^2.

Then the direct torque measurements are normalized by the theoretical laminar torque considering the dynamic viscosity of water, and the results are presented in Figure 5.11 in terms of Re_b. Using the gap Reynolds number, the current measurements are already turbulent using the critical Re_b found for the pure fluids. The same normalized torque in terms of Stokes number considering SAN particles in water is presented in Figure 5.12.

The 10% and the 20% loading fractions results increase as Re_b increases, and parallel with the results of the pure fluids for Re_b from 4.8×10^4 to 7.5×10^4 as shown in Figure 5.11. This is consistent with the observation that the presence of large SAN particles in the middle testing section facilitates the turbulent transition as discussed in the context for Figure 4.18. For loading fractions of 0.3, 0.4, and 0.5, they all show shear-thinning behaviors due to particle migration to the top cylinder region ($h > h_{top}$).

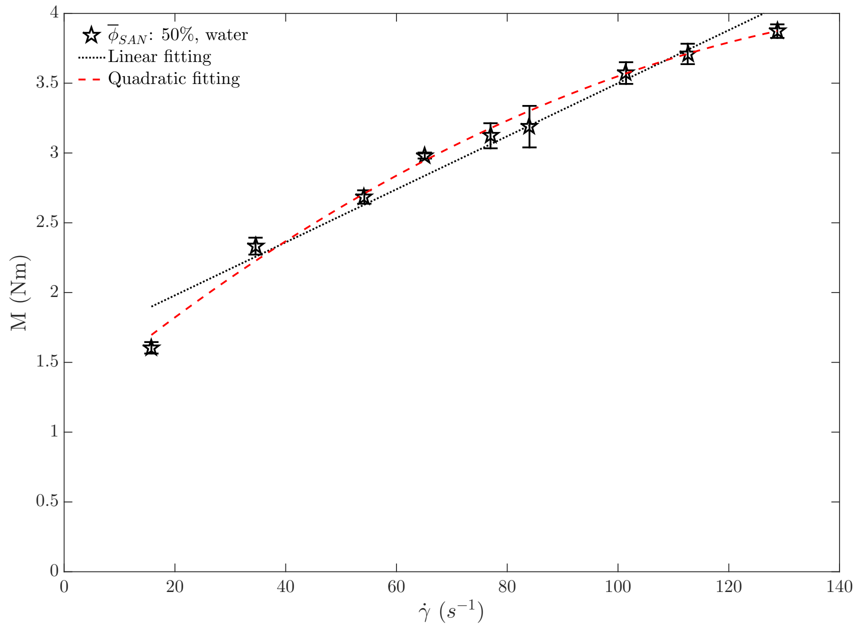

Figure 5.10: Direct torque measurement in terms of $\dot{\gamma}$ for $\overline{\phi} = 0.5$ considering SAN particles in water. $\rho_p/\rho_f = 1.05$. The linear fitting curve is $M = 1.9 \times 10^{-2}\dot{\gamma} + 1.6$. The quadratic fitting curve is $M = -9.5 \times 10^{-5}\dot{\gamma}^2 + 3.3 \times 10^{-2}\dot{\gamma} + 1.2$.

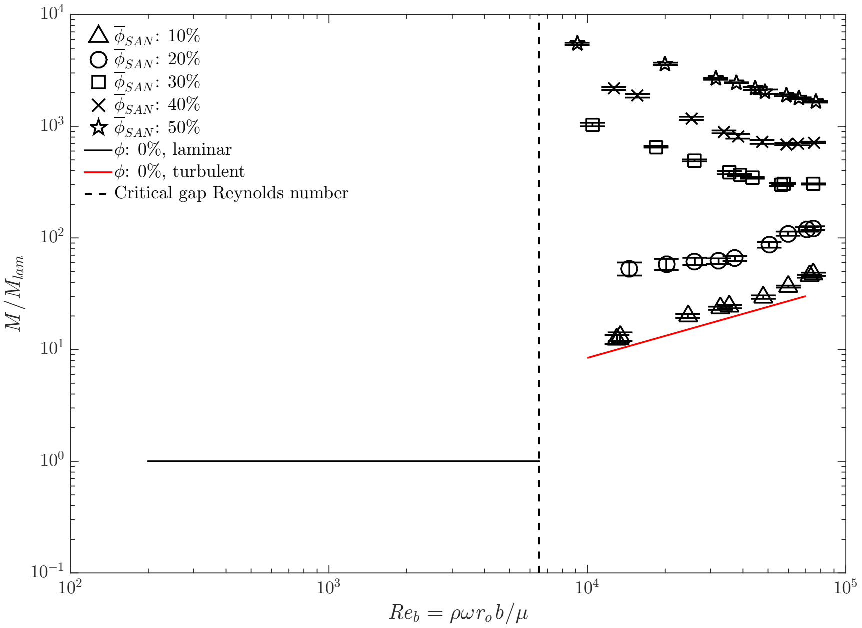

Figure 5.11: Direct torque measurement normalized by the laminar torque in terms of gap Reynolds number. The experiment considers 3.22 mm SAN particles immersed in water. $\rho_p/\rho_f = 1.05$.

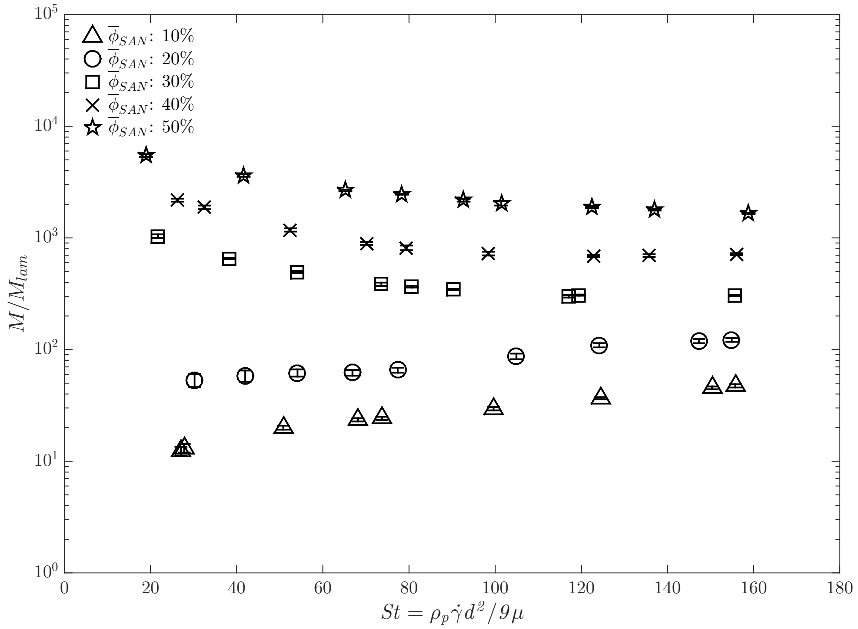

Figure 5.12: Direct torque measurement normalized by the laminar torque in terms of St. The experiment considers 3.22 mm SAN particles in water. $\rho_p/\rho_f = 1.05$.

5.4 Comparison of non-neutrally buoyant results using different particles

With the experimental results of two spherical particles with different diameters, this section aims to investigate the factors behind the differences in the torque measurements. The measurements are compared together with respect to Re_b. Following that, the experimental measurements are shown with respect to St and a defined Stokes number ($St' = \rho_p d U_{wall}/9\mu$) to further examine the matching differences between the polystyrene and SAN results.

Figure 5.13 presents the normalized results in terms of Re_b considering both polystyrene and SAN particles in water, with a $\rho_p/\rho_f = 1.05$. At the loading fractions of 10% and 20%, both results of M/M_{lam} increase with Re_b, but the dependence is reversed for $\overline{\phi} > 20\%$. For $\overline{\phi} = 10\%$, the SAN result matches well with the polystyrene result for Re_b from 1.3×10^4 to 2.6×10^4, but appear to be 62% larger than the polystyrene result for Re_b of 8.4×10^4. For $\overline{\phi} = 20\%$, the two measurements share similar slopes, but the SAN results are 2.3 times larger than the polystyrene measurements on average. For the 30% loading fraction measurement, the two measurements have similar shear-thinning behaviors, but the SAN normalized torque is 1.9 times larger than the corresponding polystyrene result for Re_b of approximately 7.5×10^4. At the state of $\overline{\phi} = 40\%$, the SAN normalized torque tends to be slightly

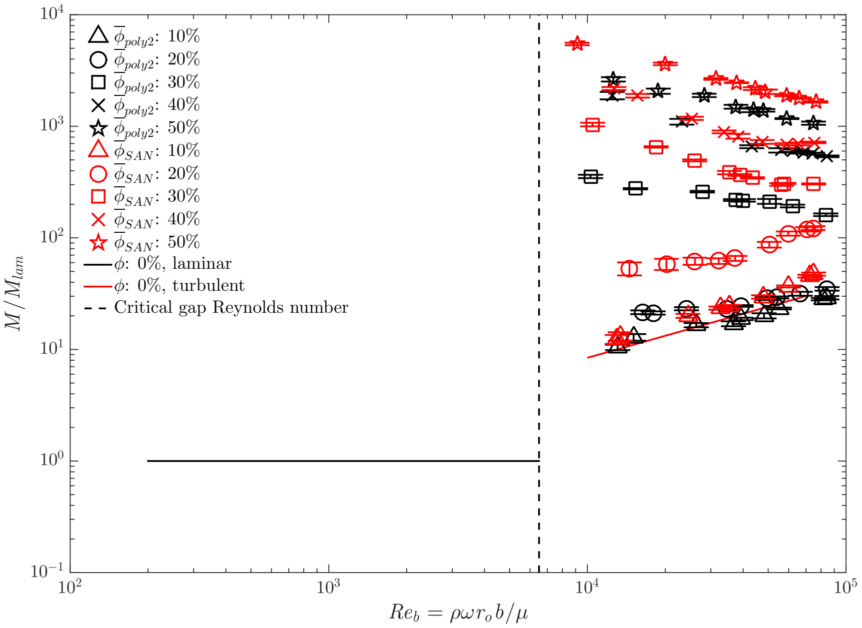

Figure 5.13: Direct torque measurements normalized by the laminar torque in terms of Re_b considering 1.27 *mm* polystyrene particles and 3.22 *mm* SAN particles in water for $\phi = 0.1, 0.2, 0.3, 0.4$, and 0.5. $\rho_p/\rho_f = 1.05$.

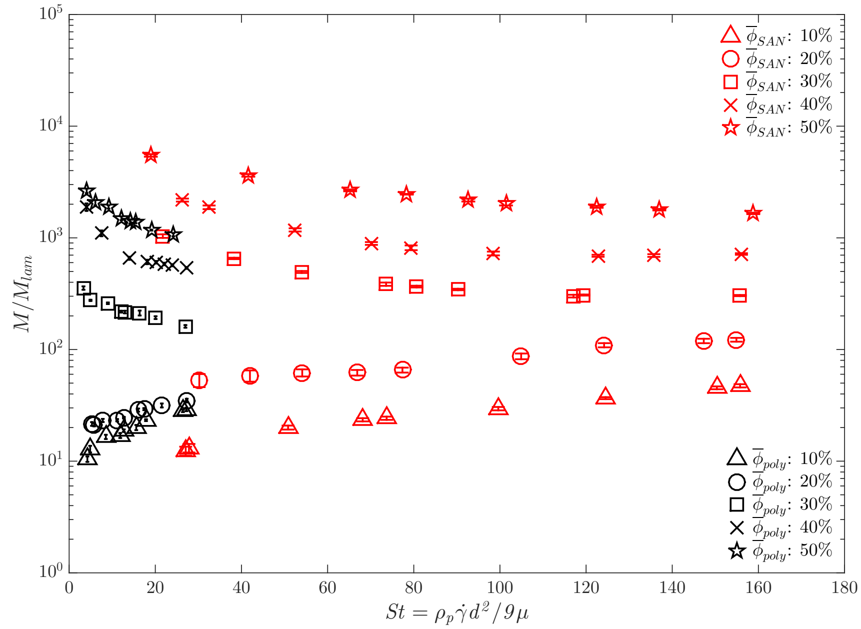

Figure 5.14: Direct torque measurement normalized by the laminar torque in terms of St for 1.27 *mm* polystyrene particles and 3.22 *mm* SAN particles in water. $\rho_p/\rho_f = 1.05$.

larger than the polystyrene results, but the normalized torques are nearly independent of Re_b and particle size for $Re_b > 5.9 \times 10^4$. The 50% SAN measurements are 55% higher than the values of the polystyrene results over the examined Re_b regions. The relatively larger inertial effects and the greater collisional impact have led to larger normalized torques of SAN particles as compared to the polystyrene particles. However, considering the relatively smaller density ratio of 1.05 and St from 3.3 to 159, the contribution to the normalized torque from particle collisions is assumed to be limited in comparison to the study of Zhou and Prosperetti (2020), in which the ρ_p/ρ_f varies from 2.5 to 10. In addition, as explained in Section 5.1, the differences in the packing structures of the polystyrene and SAN particles cause differences in the bed heights (h_o) of polystyrene and SAN particles at $\dot{\gamma} = 0$. For loading fractions greater than 20% and less than 50%, both the polystyrene and SAN particle beds have reached the middle testing cylinder ($h_{middle} < h_o < h_{top}$), but the polystyrene bed has slightly larger bed height at the same loading fraction, leading to more contact surface between the polystyrene bed and the middle testing cylinder than the SAN particle bed at static state. During the bed expansion, the difference in the static bed heights affects the axial distribution of the effective solid fraction.

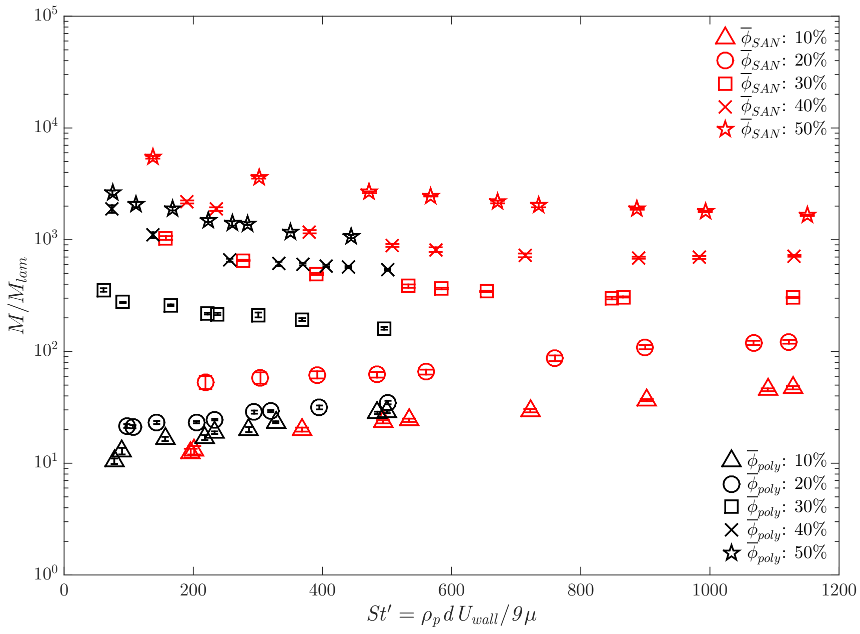

Figure 5.15: Direct torque measurement normalized by the laminar torque in terms of St' for 1.27 mm polystyrene particles and 3.22 mm SAN particles in water. $\rho_p/\rho_f = 1.05$.

The same normalized torque results are presented with respect to Stokes number in Figure 5.14. For St of approximately 29, the 10% polystyrene result is 2.3 times larger than the SAN measurements, while both the 20% measurements show good agreement. In the examination of the 30%, 40%, and 50% loading fraction results for St of approximately 20, the SAN values are 6.4 times, 4.0 times, and 4.7 times larger than the corresponding polystyrene measurements.

Following that, the normalized results are plotted in terms of St' in Figure 5.15. In the domain of St', the measurements for SAN and polystyrene particles have more overlapping regions. The 10% loading fraction results compare well, and the 20% polystyrene results appear to be slightly smaller than the corresponding SAN results. The 30%, 40%, and 50% polystyrene results still have smaller values than the SAN measurements, but the differences become narrower over the same St' region from 200 to 500 as compared with the magnitude differences in Figure 5.14.

5.5 Comparison with previous experimental results

This section discusses the comparison between the current measurement and the previous experimental results considering non-neutrally buoyant particles immersed in water.

Figure 5.16 presents the current experimental measurements considering 3.22 mm SAN particles immersed in water and the 3.34 mm polystyrene particles immersed in water from Linares Caltech thesis (Linares, 2015). Both measurements were implemented with a density ratio of 1.05. Due to the shape difference of the particles, there are some differences in the particle microstructures. As a result, the maximum loading fraction of the spherical SAN particles that can fill the rheometer annulus is 50%, while the maximum loading fraction for the elliptical polystyrene particles is 60%. The 10% results from both experimental measurements have shear-thickening behaviors, and show good agreement in terms of magnitudes. The 20% loading fraction results from Linares (2015) decreases slightly for St of approximately 10 to 20, and increases at higher Stokes numbers, but the magnitudes appear to be close to the 10% loading fraction result of the present study. The 30%, 40%, 50%, and the 60% loading fraction results from Linares (2015) all show shear-thinning behaviors, and reach relatively steady normalized torque values for $St > 80$. For St of 140, the M/M_{lam} values of 30%, 40%, 50%, and 60% loading fractions from Linares (2015) match well with the current experimental measurements concerning 20%, 30%, 40%, and 50% loading fractions. The differences between the particle bed heights of 3.22 *mm* SAN particles and 3.34 *mm* polystyrene particles, as well as the difference in the effective solid fraction distribution along the axial and radial directions between the two experiments may contribute to the differences in normalized torques.

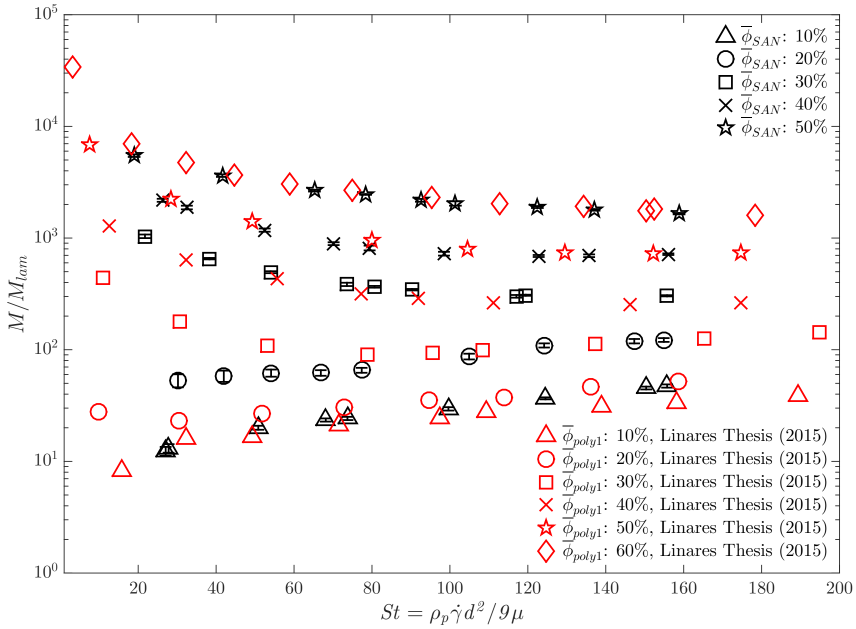

Figure 5.16: Direct torque measurement normalized by the laminar torque in terms of *St* considering the current results and the experimental results from Linares (2015). The present study considers 3.22 *mm* SAN particles in water. The Linares study considers 3.34 *mm* particles in water. $\rho_p/\rho_f = 1.05$.

5.6 Summary

For the settling particles with a density ratio of 1.05, the direct torque measurements do not show a linear dependence on the $\dot{\gamma}$. For loading fractions of 0.1 and 0.2, the normalized torques of the particles increase with St. However, for higher loading fractions from 0.3 to 0.5, due to the decreasing effective solid fraction in the middle testing region, the normalized torques gradually decrease with increasing Stokes numbers.

This chapter also introduces St' to examine the normalized torques of both particles. The normalized torques of different particles compare better as a function of St' instead of St.

Chapter 6

CONCLUSION

This thesis presents the rheological measurements for pure fluids, neutrally-buoyant suspensions, and non-neutrally buoyant suspensions in an outer-rotating rheometer with roughened walls. The current study aims to extend the torque measurements into previously untested particle Reynolds number regimes. For neutrally-buoyant suspensions, the normalized torques have shown an increased dependence on the particle Reynolds number over the examined Reynolds number (Re) regime from 0.5 to 800 and for solid fractions less than 50%. Based on the experimental results, a particle Reynolds number ($Re' = \rho_f d U_{wall}/\mu$) has been introduced to examine the normalized torques before the laminar-turbulent transition. Rheological models of normalized torques as a function of ϕ and Re' are proposed for neutrally-buoyant suspensions for solid fractions from 10% to 30% to investigate the shear-thickening behaviors.

In Section 6.1, the results of the pure fluids are discussed to investigate the laminar-turbulent transition in the Caltech Couette flow device. Section 6.2 summarizes the neutrally-buoyant torque measurements and discusses the rheological models for neutrally-buoyant suspensions. Finally, Section 6.3 summarizes the findings in non-neutrally buoyant experiments.

6.1 Summary of the pure fluids experiments

For pure fluids measurements, the results cover the gap Reynolds number regimes corresponding to the laminar, transitional, and turbulent flows. With the results using the glycerol-water mixture with 50% glycerol volume fraction, it extends measurements of the pure fluids to the previously untested transitional flow regime for the Caltech Couette flow device. The critical gap Reynolds number where the flow transition starts, and the fully turbulent gap Reynolds number where the flow reaches a fully-turbulent state are determined to be 6.5×10^3 and 1.1×10^4, respectively, based on the results of direct torques and normalized torques for pure fluids. The results show a sudden change in terms of the normalized torque magnitudes between the critical and fully-turbulent gap Reynolds numbers, corresponding to the rapid propagations of turbulence from rheometer corners to the middle testing sections. The critical gap Reynolds number and the fully-turbulent fitting curves determined in the pure fluids study also help the investigations of neutrally-buoyant and non-neutrally buoyant experiments.

6.2 Summary of the neutrally-buoyant experiments

Motivated by the previous experimental and numerical studies to investigate the moderate-Reynolds-number liquid-solid flows, the thesis aims to extend the rheological measurements to previously untested Reynolds number (Re) regimes for neutrally-buoyant suspensions.

The experiments of SAN and polystyrene particles immersed in low-viscosity and high-viscosity fluids cover a particle Reynolds number regime from 0.51 to 773 and solid fractions from 10% to 50%. Specifically, the measurements considering polystyrene particles in high-viscosity and low-viscosity fluids cover Reynolds number regimes from 0.51 to 8.5 and from 13.2 to 135, corresponding to intermediate-Reynolds-number regions which lack experimental data.

For solid fractions less than 40% and Re from 0.5 to 10, the effective viscosity of the particulate flow only depends on the solid fractions. For the intermediate Reynolds number regime of Re from 10 to 100, the effective viscosity for ϕ from 10% to 40% not only depends on the solid fraction, but also shows an increased dependence on the particle Reynolds number. For Re greater than 100, the liquid-solid flows start to transition to turbulent regimes, similar to the laminar-turbulent transition of the pure fluids. The current study finds that small polystyrene particles suppress the turbulent transition while the large SAN particles augment the turbulence. At the state of the 50% solid fraction, the effective viscosity (M/M_{lam}) has increased by a factor of 20 in comparison with the results of the 10% solid fraction, but the effective viscosity ($(M - M_o)/M_{lam}$) is nearly independent of Re. When we examine the normalized torques of two different particle sizes, the results correlate better as a function of Re' based on d rather than Re based on d^2. Therefore, considering a Re' regime from 10 to 500, this thesis proposes rheological models of M/M_{lam} in terms of Re' and for ϕ from 10% to 30%, as well as models of $(M - M_o)/M_{lam}$ in terms of Re' for solid fractions from 40% to 50%. The current experimental measurements before transition also compare well with previous experimental and numerical results as functions of both Re and Re'.

The current neutrally-buoyant study differs from the previous studies in several aspects. Most simulation studies for similar liquid-solid flow Re regimes only considered one particle diameter/radius and used the particle diameter/radius for nondimensionalization of the computational domain. However, the current experimental study used two different particle sizes and two types of fluids to cover a wide region of Reynolds numbers. Especially, the overlapping Reynolds number regimes considering different particle sizes allow for the study of the impact of particle size on the normalized torque. In addition, because it is computationally expensive to simulate the liquid-solid flow, the numerical studies discussed in this thesis only present limited data points in terms of effective viscosity as a function of the Reynolds number for a specified solid fraction. On the other hand, the design of the Caltech Couette flow device allows the experiments using relatively large particles (mm scales) sheared by the relatively higher rotational velocities with incremental magnitudes, and will not make such experiments prohibitively expensive. Therefore, the current rheological measurements uniformly distribute over the examined Reynolds number regimes, and provide sufficient data points for rheological model developments.

6.3 Summary of the non-neutrally buoyant experiments

The non-neutrally-buoyant experiments use the same polystyrene and SAN particles immersed in water ($\rho_p/\rho_f = 1.05$) with loading fractions from 10% to 50%, to study the effects of additional particle inertia on the particulate flows. The torque measurements of the suspensions cover a Stokes number region from 3.3 to 159, extending the range of Stokes number to the previously untested regime.

For loading fractions from 0.1 to 0.2, the normalized torques of both particles show shear-thickening behaviors with the increasing Stokes number, as the effective solid fraction increases in the middle testing region. However, for loading fractions from 30% to 50%, the dependence is reversed, and the normalized torques decrease with increasing Stokes numbers due to the decreasing effective solid fraction in the middle testing region. Similar to Re', a Stokes number (St') based on the maximum shear flow velocity is introduced to examine the normalized torques of polystyrene and SAN particles. The comparison for normalized torques of polystyrene and SAN particles shows better correlations as functions of St' based on d rather than St based on d^2.

6.4 Future work

In this experimental study, experiments focus on the torque measurements of pure fluids, neutrally-buoyant suspensions, and non-neutrally-buoyant suspensions. These measurements can help the advancement of rheological model developments.

However, without the velocity fluctuation, the effective solid fraction and the height of the settled particles (non-neutrally buoyant), as well as the collisional pressure measurements, the relative contributions to the effective viscosity of liquid-solid flows cannot be determined.

Measurements of velocity fluctuations for particles near the wall should be conducted to determine the Reynolds stress from the solid phase. In the appendix, a visualization method similar to particle image velocimetry (PIV) has been presented to determine the velocity fluctuations of the particles. The proposed methods take images of the liquids-solid flows from a transparent inner cylinder, and then use algorithms to identify the centers of the particles. Finally, the processed images with labeled particle centers are analyzed using PIVlab to determine the average velocity and the fluctuating velocity of particles near the wall. The measured velocity fluctuations would allow the analysis of the contribution of the Reynolds stresses from the solid phase to the effective viscosity.

It would be of interest to measure the solid fraction distribution along the vertical annulus direction and the height of the settled particles for non-neutrally buoyant suspensions. Unlike the neutrally-buoyant experiments, the distribution of particles in non-neutrally buoyant mixture is heterogeneous, exhibiting a solid fraction gradient along the vertical annulus direction. Once the rotation of the outer cylinder is stopped, the height of the settled particles will gradually decrease over time. A visualization method using the projected particle area to calculate the effective solid fraction has been developed by Linares and presented in her Caltech thesis (Linares, 2015). In the same time, the height of the settled particles can also be determined by determining the upper contour of the particle bed in the image. The same methods should be applied to the non-neutrally buoyant visualization images of polystyrene and SAN particles captured by a camera placed inside a transparent cylinder, and the calculated effective solid fraction and settled particle height can then be used to study the resuspension and settling of particles.

Experiments considering non-neutrally buoyant particles with higher Stokes numbers should be conducted to further examine the impact of the collisional pressure on the torque measurements. Preliminary collisional pressure measurements had been implemented at the Hunt research lab using the Caltech Couette flow device and particles with a density around 1050 kg/m^3. However, the piezoelectric pressure sensors (PCB) could not measure the collisional pressure generated by the 1050 kg/m^3 particles due to the small magnitudes of the pressure signals. It would be also challenging to measure the collisional pressure of the 1050 kg/m^3 particles used in the current neutrally-buoyant study due to the small density ratio. The preliminary experimental results are similar to the conclusion from the simulation study of Haddadi and Morris (2014), indicating that the contribution of the collisional pressure to the torque measurement in the neutrally buoyant suspensions (ρ_p/ρ_f = 1) considering intermediate particle Reynolds numbers is limited. To address the challenge of collisional pressure measurement, non-neutrally buoyant experiments with higher rotational speeds and larger density ratios (ρ_p/ρ_f) should be conducted. The numerical study from Zhou and Prosperetti (2020) can shed light on the experimental investigation of liquid-solid flows in the collisional regimes. With particle to fluid density ratios varying between 2.5 and 10, Zhou and Prosperetti (2020) found that the particle-wall and particle-particle collisions play important roles in the effective viscosities of liquid-solid mixtures. Therefore, if future non-neutrally buoyant experiments can use particles with densities 2.5 or 10 times higher than the density of the suspending fluid, the collisional pressure generated by the liquid-solid flows may be determined. In addition, the current Caltech Couette flow device has a limitation in its rotational speed. If the current motor and the ball bearings can be improved to allow for higher $\dot{\gamma}$ to suspend the particles, the Stokes number can be further increased and the signals of the collisional pressure may be detected.

In summary, for the neutrally-buoyant and the non-neutrally buoyant experiments, future in-depth investigation is needed to determine the relative contribution to the measured torque from the velocity fluctuations, the effective solid fraction, the settled particle height and the particle collisions.

BIBLIOGRAPHY

Acrivos, A. et al. (1994). “On the measurements of the relative viscosity of suspensions”. In: *Journal of Rheology* 38.5, pp. 1285–1296.

Atta, C. V. (1966). “Exploratory measurements in spiral turbulence”. In: *Journal of Fluid Mechanics* 25, pp. 495–512.

Bagnold, R. A. (1954). “Experiments on a gravity-free dispersion of large solid spheres in a Newtonian fluid under shear”. In: *Proceedings of the Royal Society of London, Series A* 225.1160, pp. 49–53.

Barnes, H. A. (1995). “A review of the slip (wall depletion) of polymer solutions, emulsions and particle suspensions in viscometers: Its cause, character, and cure”. In: *Journal of Non-Newtonian Fluid Mechanics* 56.3, pp. 221–251.

Batchelor, G. K. (1970). “The stress system in a suspension of force-free particles”. In: *Journal of Fluid Mechanics* 41, pp. 545–570.

Boyer, F. et al. (2011). “Unifying suspension and granular rheology”. In: *Physical Review Letters* 107, pp. 188301–5.

Brady, J. F. and G. Bossis (1988). “Stokesian dynamics”. In: *Annual Review of Fluid Mechanics* 20, pp. 111–157.

Brennen, C. E. (2005). *Fundamentals of Multiphase Flows*. Cambridge University Press.

Buscall, R. et al. (1993). “The rheology of concentrated dispersions of weakly attracting colloidal particles with and without wall slip”. In: *Journal of Rheology* 37.4, pp. 621–641.

Cartellier, A. and N. Riviere (2001). “Effect of particle size on modulating turbulent intensity”. In: *Physics of Fluids* 13, pp. 2165–2181.

Cheng, N. (2008). “Formula for the viscosity of a glycerol-water mixture”. In: *Industrial and Engineering Chemistry Research* 47, pp. 3285–3288.

Coles, D. (1965). “Transition in circular Couette flow”. In: *Journal of Fluid Mechanics* 21, pp. 385–424.

Conway, S. L. et al. (2004). “A Taylor vortex analogy in granular flows”. In: *Nature* 431, pp. 433–437.

Eilers, H. (1941). “The viscosity of emulsions made of highly viscous materials as a function of concentration”. In: *Koloid-Z* 97, p. 313.

Ernst, R. C. et al. (1936). “The physical properties of the ternary system ethyl alcohol-glycerin-water”. In: *The Journal of Physical Chemistry A* 40, p. 5.

Fall, A. et al. (2009). “Yield stress and shear banding in granular suspensions”. In: *Physical Review Letters* 103, pp. 178301–4.

Fornari, W. et al. (2016). “Rheology of confined non-brownian suspensions”. In: *Physical Review Letters* 116, p. 018301.

Gallier, S. et al. (2016). “Effect of confinement in wall-bounded non-colloidal suspensions”. In: *Journal of Fluid Mechanics* 799, pp. 100–127.

Gore, R. A. and C. T. Crowe (1989). “Effect of particle size on modulating turbulent intensity”. In: *International Journal of Multiphase Flow* 15, pp. 279–285.

– (1991). “Modulation of turbulence by a dispersed phase”. In: *Journal of Fluids Engineering* 113.2, pp. 304–307.

Haddadi, H. and J. F. Morris (2014). “Microstructure and rheology of finite inertia neutrally buoyant suspensions”. In: *Journal of Fluid Mechanics* 749, pp. 431–459.

Hanes, D. M. and D. L. Inman (1985). “Observations of rapidly flowing granular-fluid materials”. In: *Journal of Fluid Mechanics* 150, pp. 357–380.

Hunt, M. L. et al. (2002). “Revisiting the 1954 suspension experiments of R.A. Bagnold”. In: *Journal of Fluid Mechanics* 452, pp. 1–24.

Jeffrey, D. J. and A. Acrivos (1976). “The rheological properties of suspensions of rigid particles”. In: *American Institute of Chemical Engineers Journal* 22.3, pp. 417–433.

Joseph, G. G. et al. (2001). “Particle-wall collisions in a viscous fluid”. In: *Journal of Fluid Mechanics* 433, pp. 329–346.

Koos, E. (2009). “Rheological Measurements in Liquid-Solid Flows”. PhD thesis. California Institute of Technology.

Koos, E. et al. (2012). “Rheological measurements of large particles in high shear rate flows”. In: *Physics of Fluids* 24.013302, pp. 1–19.

Krieger, I. M. (1963). “A dimensional approach to colloid rheology”. English. In: *Transactions of the Society of Rheology* 7, pp. 101–109.

– (1972). “Rheology of monodisperse latices”. In: *Advances in Colloid and Interface Science* 3, p. 111.

Kulkarni, P. M. and J. F. Morris (2008). “Suspension properties at finite Reynolds number from simulated shear flow”. In: *Physics of Fluids* 20, pp. 40602–12.

Linares, E. (2015). “Experimental Study on Inertial Effects in Liquid-Solid Flows”. PhD thesis. California Institute of Technology.

Linares, E. et al. (2017). “Effects of inertia and turbulence on rheological measurements of neutrally buoyant suspensions”. In: *Journal of Fluid Mechanics* 811, pp. 525–543.

Martinez, M. et al. (2007). “Measurement of pseudoturbulence intensity in monodispersed bubbly liquids for 10<Re<500”. In: *Physics of Fluids* 19, p. 103302.

Matas, J. P. et al. (2003). “Transition to turbulence in particulate pipe flow”. In: *Physical Review Letters* 90.1, pp. 4501–4504.

Mendez, D. et al. (2013). “Power spectral distributions of pseudo-turbulent bubbly flows”. In: *Physics of Fluids* 25, p. 043303.

Mueller, S. et al. (2010). “The rheology of suspensions in solid particles”. In: *Proceedings of the Royal Society of London, Series A* 466, pp. 1201–1228.

Mullin, T. and T. B. Benjamin (1980). “Transition to oscillatory motion in the Taylor experiment”. In: *Nature* 288, pp. 567–569.

Pabst, W. (2004). “Fundamental considerations on suspension rheology”. In: *Ceramics-Silikaty* 48, pp. 6–13.

Phillips, R. J. et al. (1992). “A constitutive equation for concentrated suspensions that accounts for shear- induced particle migration”. In: *Physics of Fluids* 4, p. 30.

Picano, F. et al. (2013). “Shear thickening in non-Newtonian suspensions: An excluded volume effect”. In: *Physical Review Letters* 111, pp. 98302–4.

Prasad, D. and H. K. Kytömaa (1995). “Particle stress and viscous compaction during shear of dense suspensions”. In: *International Journal of Multiphase Flow* 21.5, pp. 775–785.

Rahmani, M. et al. (2018). “Momentum balance and stresses in a suspension of spherical particles in a plane Couette flow”. In: *Physics of Fluids* 30, p. 043301.

Ravelet, F., R. Delfos, and J. Westerweel (2010). “Influence of global rotation and reynolds number on the large-scale features of a turbulent Taylor–Couette flow”. In: *Physics of Fluids* 22, p. 055103.

Ruiz-Angulo, A. and M. L. Hunt (2010). “Measurements of the coefficient of restitution for particle collisions with ductile surfaces in a liquid”. In: *Granular Matter* 12, pp. 185–191.

Savage, S. B. and S. McKeown (1983). “Shear stresses developed during rapid shear of concentrated suspensions of large spherical particles between concentric cylinders”. In: *Journal of Fluid Mechanics* 127, pp. 453–472.

Schlichting, H. (1951). *Boundary Layer Theory*. 7^{th}. New York: McGraw Hill.

Stickel, J. J. and R. L. Powell (2005). “Fluid mechanics and rheology of dense suspensions”. In: *Annual Review of Fluid Mechanics* 37.1, pp. 129–149.

Taylor, G. I. (1936a). “Fluid friction between rotating cylinders, I. Torque measurements”. In: *Proceedings of the Royal Society of London, Series A* 157.892, pp. 546–564.

– (1936b). “Fluid friction between rotating cylinders, II. Distribution of velocity between concentric cylinders when outer one is rotating and inner one is at rest”. In: *Proceedings of the Royal Society of London, Series A* 157.892, pp. 565–578.

Yang, F. L. and M. L. Hunt (2006). “Dynamics of particle-particle collisions in a viscous liquid”. In: *Physics of Fluids* 18.

Yeo, K. and M. R. Maxey (2013). “Dynamics and rheology of concentrated, finite-Reynolds- number suspensions in a homogeneous shear flow”. In: *Physics of Fluids* 25, pp. 533303–24.

Zenit, R. et al. (1997). “Collisional particle pressure measurement in solid-liquid flows”. In: *Journal of Fluid Mechanics* 353.

Zenit, R. and M. L. Hunt (1999). “Mechanics of immersed particle collisions”. In: *Journal of Fluids Engineering* 121.1, pp. 179–184.

Zhou, G. and A. Prosperetti (2020). “Inertial effects in shear flow of a fluid-particle mixture: resolved simulations”. In: *Physical Review Fluids* 5, p. 084301.

Appendix A

PARTICLE IMAGE CORRELATION FOR THE MEASUREMENTS OF VELOCITY FLUCTUATIONS

One limitation of the current study of particulate flow with inertial and viscous effects is that it only considers the torque measurements of the liquid-solid flows. Without the direct measurements of the velocity fluctuations, the relative contribution of Reynolds stress to the effective viscosity of liquid-solid flow cannot be quantified. To determine the velocity fluctuations of particles near the inner wall, a particle visualization and analysis method has been developed for SAN and polystyrene particles.

In this appendix, the methods used to identify the centers of particles are discussed in detail. Then a method using PIVlab to implement particle image correlation is described. Finally, Section A.2 discusses future experiments to determine the particle velocity fluctuations in the Caltech Couette flow device.

A.1 Particle center identification

One of the biggest challenges to process the images of liquid-solid flows for the present study is to accurately identify the centers of the polystyrene and SAN particles. This section presents a method to identify and mark the centers of the particles before the particle image correlations.

There are two major steps for particle center identification, including improving the color contrast between the particle and the background, as well as finding an effective algorithm to detect the circular shape of the particle.

One way to improve the color contrast is to paint a thin layer of red paint on the surface of the particles. The thin layer of the paint has a limited impact on the particle density. Several commercially-available red spray paints have been tested for the SAN and the polystyrene particles. The Rust-Oleum red paint is found to be best since the paint provides an ethanol-resistant coating for the particles. Especially, the particles with the Rust-Oleum red coatings have been immersed in the glycerol-water and glycerol-ethanol mixtures for 7 days, and the red paint does not dissolve in the suspending fluids.

Once the frame is preprocessed using the color segmenter tool, an algorithm based

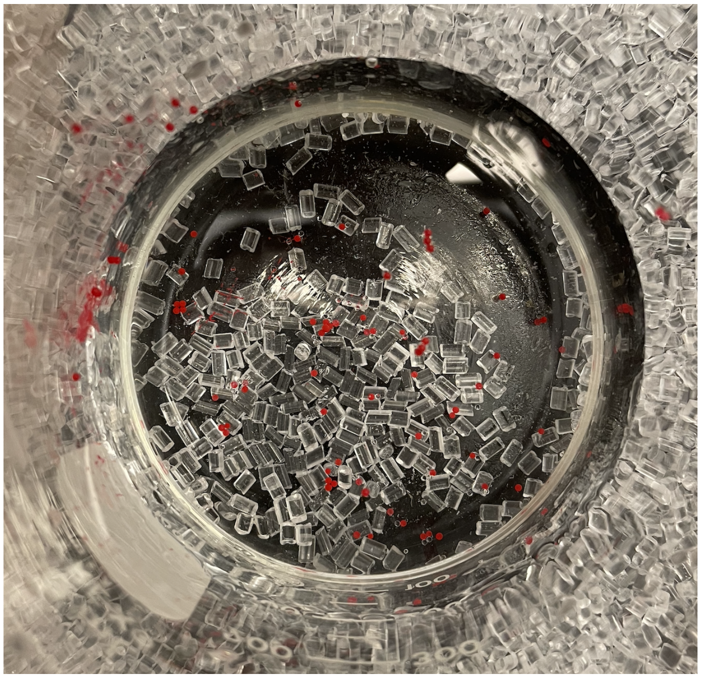

Figure A.1: Image processing example considering polystyrene particles with red paint rotating clockwise in water. The black background is the same waterproof vinyl sticker sheet covering the rheometer inner surface. The elliptical particles on the bottom are the same 3.34 *mm* particles glued on the waterproof sheet as the rough surface. The image corresponds to the first frame of the video.

on the "Find Circles" function of the MATLAB 2021 version is used to locate the centers of the particles. With this tool, we can set the minimum and the maximum particle diameters of interest, and the sensitivity of the detection function.

An experimental setup to mimic the rheometer environment had been built to test the particle image correlation. The centers of the 3.22 *mm* SAN particles can be determined by the "Find Circles" algorithm without painting the particles. However, it is more challenging to accurately identify the centers of the 1.27 *mm* polystyrene particles due to the small particle size.

The following section uses polystyrene particles with red paint rotating clockwise in water as an example to demonstrate the process of particle center identification. After a video of particle motion is recorded, the video is broken into frames. Figure A.1 presents the first frame of the video recording the clockwise rotation of 1.27 *mm* red particles in water. The black sheet on the background is the same waterproof vinyl sticker sheet covering the rheometer surface. The elliptical particles on the bottom are the 3.34 *mm* polystyrene particles used to roughen the rheometer surface.

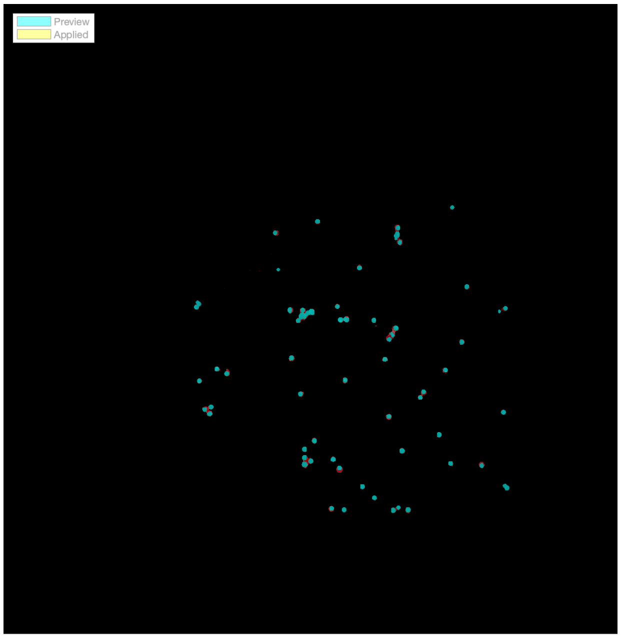

Figure A.2: Image processing example of polystyrene particle identification considering polystyrene particles with red paint rotating clockwise in water. The red dots on the bottom are the original red particles segmented from Figure A.1. The blue dots overlapping the red particles are the circular contours generated by the algorithm to identify the polystyrene particles. The image corresponds to the first frame of the video.

The Image Segmenter Tool in MATLAB is first used to specify the region of interest for particle image correlation in Figure A.1, creating a mask filtering out the regions outside the glass container filled with particles and water. Following that, the color threshold in the Image Segmenter Tool is adjusted to isolate the red polystyrene particles with circular shapes. The preprocessed image includes the isolated red polystyrene particles located on the black image with the same dimensions as the original frame of Figure A.1.

Then the function of "Find Circles" is used to find the centers of the isolated red particles. Figure A.2 shows the red particle identification results for Figure A.1. The red dots on the bottom represent the isolated polystyrene particles from Figure A.1. The blue dots overlapping the red particles are the algorithm-generated circular particle identification marks. In this way, we can directly observe which red polystyrene particles are detected and how accurate the detection is given the input parameters of particle size and detection sensitivity. With appropriate particle diameter range and sensitivity, the red polystyrene particles can be detected even though the particles stick together. Once the circular contours of the polystyrene particles are identified, the particle center locations in terms of pixels can be extracted.

Once the parameters for the Image Segmenter Tool and the "Find Circles" Tool are determined for the first frame of the video, MATLAB can auto-generate scripts that can process the rest frames and calculate the locations of the particle centers. The auto-generated scripts are then incorporated into the main algorithm that can convert the original video of particle motions into a series of images with white particle centers labeled on the black images.

A.2 Particle image correlation

The visualization method described in this appendix is similar to particle image velocimetry (PIV), but is implemented in a simplified way. Due to the *mm* scale-sized particles and the relatively large Stokes number, the calculated particle velocities can only represent the motions of the particles near the inner wall, but cannot represent the instantaneous flow field of the suspending fluid. Both OpenPIV and PIVlab have been tested to process the images. PIVlab has more functions of velocity analysis than OpenPIV. Therefore, this section describes a way to use PIVlab to analyze the velocity fluctuation of the particles in the liquid-solid flow.

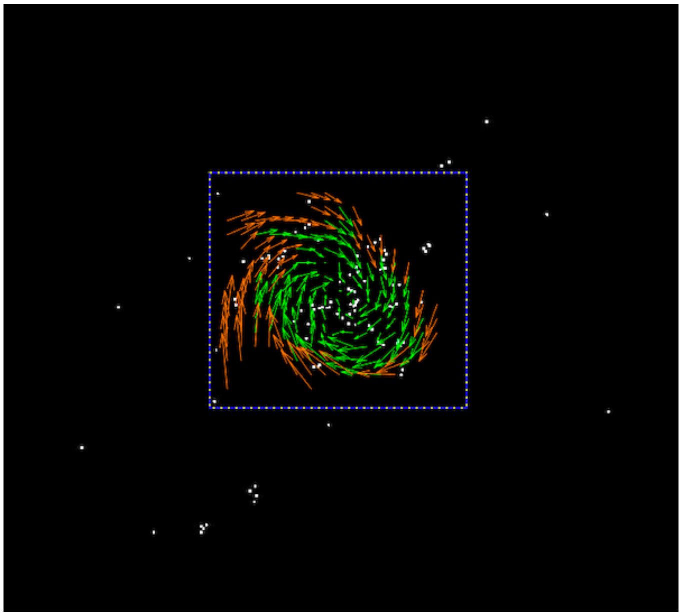

Figure A.3: Image processing example of particle image correlation considering polystyrene particles with red paint rotating clockwise in water. The area inside the box with blue-dashed boundaries is the region of interest, filled with calculated velocity vectors considering rotating particles. The image corresponds to the last frame of the video.

PIVlab is used to import the series of images with marked centers and calculate the average velocity as well as the velocity fluctuations. Figure A.3 presents the results of the particle image correlation for the video of the red particles rotating clockwise in water. The distribution of the velocity vectors is consistent with the particle rotation directions. The velocity fluctuation can then be calculated based on the velocity values for each particle.

A.3 Future work

The method of particle image correlation described in this appendix will be used to determine the velocity fluctuations of liquid-solid mixtures in the Caltech Couette flow device.

A transparent cylinder with the same radius as the inner rheometer cylinder has been built. The transparent cylinder will be used to replace the middle and upper inner cylinders. The transparent cylinder will then be roughened with the same 3.34 mm polystyrene particles, leaving a small window for visualization. Around 20% of the particles will be painted to be red and mixed with other loading particles before the experiment. The particle image correlation methods will be used to calculate the velocity fluctuations of the red tracer particles near the wall.